

RICE UNIVERSITY

Nanobody-mediated dynamic and spatial control of cellular proteins for mammalian gene circuit engineering

by

Brianna Jayanthi

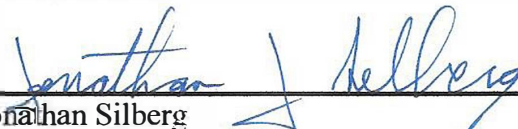
A THESIS SUBMITTED IN PARTIAL FULFILLMENT OF THE
REQUIREMENTS FOR THE DEGREE

Doctor of Philosophy

APPROVED, THESIS COMMITTEE



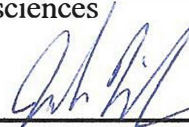
Laura Segatori, Chair
Associate Professor, Department of
Bioengineering



Jonathan Silberg
Professor, Department of Biosciences
Director, Systems, Synthetic and Physical
Biology Graduate Program



Matthew Bennett
Associate Professor, Department of
Biosciences



Jordan Miller
Assistant Professor, Department of
Bioengineering

HOUSTON, TEXAS
December 2019

ABSTRACT

Nanobody-mediated dynamic and spatial control of cellular proteins for mammalian gene circuit engineering

by

Brianna Jayanthi

Cellular information processing in mammalian cells relies on sophisticated and highly dynamic mechanisms. Unravelling these mechanisms remains a challenging endeavor and has limited *de novo* design of biological functions. Controlling cellular phenotypes requires precise control of protein concentration and localization, which is typically realized through the design of genetic networks orthogonal to the cellular circuitry. This work describes my efforts to develop tools for achieving temporal and spatial control over cellular proteins through post-translational regulation that can be generally used to characterize and manipulate the complex genetic networks that regulate mammalian cells. I first illustrated the use of a nanobody-based platform designed to control degradation of target proteins (the NanoDeg) to improve the dynamic range and temporal resolution of input-dependent reporter systems. I then explored integration of a reporter-specific NanoDeg into a genetic circuit through a feedforward loop to generate an improved heat-shock reporter system. To enhance temporal control of genetic networks, I investigated strategies to use the NanoDeg for controlling the oscillatory behavior of a range of different circuit topologies. Finally, I developed a nanobody-based platform for controlling the subcellular localization of target proteins. Using this

strategy, I experimentally demonstrated selective target localization to multiple cellular compartments and investigated different circuit architectures for dynamic control of target localization to different compartments. Combining nanobody-mediated localization and degradation with orthogonal transcriptional regulation I developed a nanobody-based toolkit to achieve spatial and temporal control of target protein levels.

Acknowledgments

I would first like to thank my advisor, Dr. Laura Segatori. Working under her direction has been a truly rewarding and humbling experience. I am forever indebted to her for teaching me and inspiring the creativity for me to do this work.

I am sincerely grateful to my committee members, Dr. Joff Silberg, Dr. Matt Bennett and Dr. Jordan Miller for their valuable contributions and support of this work.

I also thank all of the faculty and staff of the SSPB program for their drive to develop a community and support exciting research.

I would also like to thank current and former Segatori Lab members, Bhagyashree, Santi, Carlos, Yimeng, Lauren and Wenting, for teaching me many things and making the longest days bearable with the promise of baked goods. Yongin Choi and Zengyi Wan for the opportunity to learn from mentoring two incredible minds.

I would like to thank the inaugural cohort of SSPB for their comradery in navigating the uncharted and setting the bar high. A special thanks is owed to Josh Atkinson and Felix Ekness for their unmatched friendship, and Dongya Jia for radiating the joy that we all hope to attain in research.

I would like to thank all of my family for the never-ending, selfless support. I am especially grateful to my mom, Julie, for making learning a priority and pushing

me to make my dreams a reality, my twin sister, Amanda, for reminding me what matters most, and my grandparents, Kerry and Sue Jones, for the constant support of their faith.

Finally, I would like to thank my husband, Shridhar, for his love and for being my greatest teacher in all matters of the mind and spirit.

Contents

Acknowledgments	iv
Contents	vi
List of Figures	viii
List of Tables	x
List of Equations	xi
Nomenclature	xii
Introduction	1
Objectives	6
Input-dependent post-translational control of the reporter output enhances dynamic resolution of mammalian signaling systems	10
3.1. Introduction	10
3.2. The NanoDeg as a module for genetic circuits.....	13
3.2.1. Mathematical model of input-dependent NanoDeg reporter circuits	16
3.3. Design rules of the NanoDeg Inverter circuit topology.....	25
3.3.1. Implementation of a heat shock-inducible NanoDeg Inverter circuit	29
3.3.2. Tuning the NanoDeg Inverter circuit	32
3.4. Concluding Remarks.....	35
Post-translational modification of degradation rates can generate oscillations in proto-oscillating biomolecular networks	36
4.1. Introduction	36
4.2. Results.....	40
4.2.1. Activator-repressor.....	40
4.2.2. Goodwin oscillator.....	47
4.2.3. Repressilator regulation	53
4.2.4. NanoDeg repressilator.....	59
4.3. Discussion.....	64
4.4. Methods.....	66
4.4.1. Activator Repressor simulations.....	67

4.4.2. Goodwin Oscillator simulations.....	71
4.4.3. Repressilator Regulation simulations	73
4.4.4. NanoDeg repressilator simulations	80
A platform for post-translational spatiotemporal control of cytosolic proteins.....	83
5.1. Introduction	83
5.2. Results.....	86
5.2.1. Design of a nanobody-based platform for spatial control of GFP.	86
5.2.2. Tuning GFP localization by modulating nanobody-mediated control of GFP localization and degradation.	97
5.2.3. Design of a Genetic Toggle Switch for Spatial Control of GFP Output.....	102
5.3. Discussion.....	107
5.4. Materials and Methods.....	111
5.4.1. Plasmids and Cloning.....	111
5.4.2. Cell culture and transfections.....	117
5.4.3. Lentivirus production and transduction	118
5.4.4. Generation of stable cell lines	118
5.4.5. Flow cytometry analyses	119
5.4.6. Immunofluorescence for confocal microscopy	120
5.4.7. Image analysis	121
5.4.8. Statistical analysis.....	121
Summary and Future Work.....	122
6.1. Summary	122
6.2. Future Work	124
References	128

List of Figures

Figure 1.1 The NanoDeg Platform.	3
Figure 3.1 Schematic representation of genetic network motifs.....	15
Figure 3.2 Mathematical model of the genetic network motifs.....	18
Figure 3.3 Comparison of network motifs.....	24
Figure 3.4 Design rules of the NanoDeg Inverter topology.....	28
Figure 3.5 Implementation of a heat shock-inducible NanoDeg Inverter circuit.	31
Figure 4.1 A NanoDeg modified Activator-Repressor oscillator.....	42
Figure 4.2 Tuning the activator-repressor with NanoDeg concentration and half-life.....	45
Figure 4.3 Effect of NanoDeg affinity and rate of interaction on oscillations... 	46
Figure 4.4 The Goodwin oscillator.	49
Figure 4.5 A NanoDeg modified Goodwin oscillator.	51
Figure 4.6 Repressilator tuning with a common NanoDeg.	56
Figure 4.7 Repressilator tuning with individual NanoDegs.	58
Figure 4.8 The NanoDeg Repressilator from a repressor-of-a-repressor network.	61
Figure 4.9 Tuning the NanoDeg Repressilator by NanoDeg concentration and half-life.....	62
Figure 4.10 Effect of repressor sensitivity on oscillations of the NanoDeg repressilator.....	63
Figure 5.1 NanoLoc-mediated control of GFP subcellular localization.....	88
Figure 5.2 GFP subcellular localization in the absence of NanoLoc.....	89

Figure 5.3 Residence time of NanoLoc-mediated GFP subcellular localization.	90
Figure 5.4 Dual-compartment subcellular localization of GFP with the NanoLoc.	92
Figure 5.5 GFP mitochondrial localization as a function of VHH_{MOM} and GFP expression level.	93
Figure 5.6 Modulation of mitochondria-localized GFP fluorescence using the NanoDeg.	95
Figure 5.7 Induction of iRFP expression in the dual-input system.	98
Figure 5.8 A dual-input NanoLoc and NanoDeg system for temporal control of GFP localization.	100
Figure 5.9 Modulation of GFP localization to the mitochondria and the nucleus using a dual-input NanoLoc expression system.	101
Figure 5.10 A synthetic toggle switch with NanoLoc to control GFP subcellular localization.	105

List of Tables

Table 3.2.1 Parameters used in input-dependent NanoDeg circuit simulations	22
Table 4.4.1 Parameters used in activator-repressor simulations.....	70
Table 4.4.2 Parameters used in Goodwin oscillator simulations.....	73
Table 4.4.3 Parameters used in repressilator with a common NanoDeg simulations.....	76
Table 4.4.4 Parameters used in Repressilator with individual NanoDegs simulations.....	80
Table 4.4.5 Parameters used in NanoDeg repressilator simulations.....	82
Table 5.4.1 Localization tag sequences	112
Table 5.4.2 Plasmids used in the NanoLoc study.....	115
Table 5.4.3 List of primers used in the NanoLoc study.	117

List of Equations

Equation 3.2.1 Input-dependent promoter activity.....	20
Equation 3.2.2 Direct Reporter topologies.....	20
Equation 3.2.3 The NanoDeg Activator topology.	20
Equation 3.2.4 The NanoDeg Inverter topology.	21
Equation 4.4.1 Activator-repressor with an activator-targetting NanoDeg.....	68
Equation 4.4.2 Goodwin oscillator with a mature repressor-targetting NanoDeg.	71
Equation 4.4.3 Repressilator with a common NanoDeg.	73
Equation 4.4.4 Repressilator with individual NanoDegs.....	76
Equation 4.4.5 NanoDeg repressilator.....	80

Nomenclature

VHH	nanobody; variable domain of heavy-chain only antibodies
ODC	degradation tag of ornithine decarboxylase
EKRAB	erythromycin-dependent transrepressor
ETR	EKRAB operator sequence
Em	erythromycin
TetR	tetracycline repressor
TO	TetR operator sequence
Tc	tetracycline
PIPKRAB	pristinamycin-dependent transrepressor
PIR	PIPKRAB operator sequence
PI	Pristinamycin I

Introduction

Cells have evolved sophisticated mechanisms to maintain homeostasis in highly dynamic environments and respond to a variety of signals with diverse behaviors which are realized through complex networks that process biological information. Proper information processing in these networks is managed by precise spatial and temporal control of proteins [1]–[3]. Synthetic biology provides a powerful framework to engineer cellular pathways, thereby improving our understanding of the sophisticated coordination between individual reactions displayed in biological systems and informing the design of novel biological functions [4], [5].

Cells often control protein activities by regulating protein concentration. In nature, protein concentration is controlled at every step, from DNA transcription to post-translational regulation, including protein localization and degradation. Control in synthetic gene networks can also be introduced at any level of this

2

hierarchy. Impressive success has already been made in the design of mammalian genetic circuits based on transcriptional level control [6], [7]. In theory, additional mechanisms of protein regulation could also be targeted for engineering circuits with increased functionality. There remains a need for tools to more precisely control protein function in a manner similar to these endogenous mechanisms, especially at the post-translational level [8], [9]. The application of such advanced tools would provide unprecedented insights and design rules for engineering biological function.

Approaches for controlling protein function in living cells can be broadly classified into two groups. One approach relies on direct genetic fusion of the target protein with effector domains dictating post-translational processing, such as protein-protein interactions [10], phosphorylation [11], localization [12], or degradation [13]. The other approach relies on secondary proteins with high affinity for the target protein [14], [15]. These secondary proteins can be functionalized with various effector domains (i.e., degradation or localization signal sequences) to regulate the function of the target protein avoiding any need for genetic modification of the target. Conventional antibodies and antibody fragments (scFv) have traditionally filled the role of a secondary protein for high affinity target recognition [16], [17], but they are unstable and difficult to express in cells. Synthetic protein binders that are easily expressed in cells have been developed, but engineering these proteins for recognition of new targets remains a significant challenge [18]. Nanobodies, on the other hand, present an ideal target recognition element for the study of cellular proteins. Nanobodies comprise the monomeric

3

antigen-recognition domain of Camelid heavy-chain only antibodies. In addition to being easily customized to recognize new targets from immunized Camelids [19]–[24] and selection from display libraries [25]–[30], nanobodies are small, stable, and easily expressed in cells [31], [32]. Due to their unique structure and increased hypervariable regions, nanobodies also present an increased repertoire [33]–[36] of potential targets compared to conventional antibodies.

The ideal target recognition properties of nanobodies were recently exploited for development of the NanoDeg, a platform technology for targeted, post-translational depletion of cellular proteins [37]. The NanoDeg consists of a molecular recognition unit provided by the nanobody (VHH) and a degradation signaling unit provided by a degen. The nanobody mediates recognition of the target with high specificity and selectivity and can be engineered to target virtually any cellular protein [38]. The degen determines the rate of degradation of the nanobody-target complex and can be customized to convey susceptibility to different pathways of proteasomal degradation and with tunable rate of degradation (Figure 1.1A).

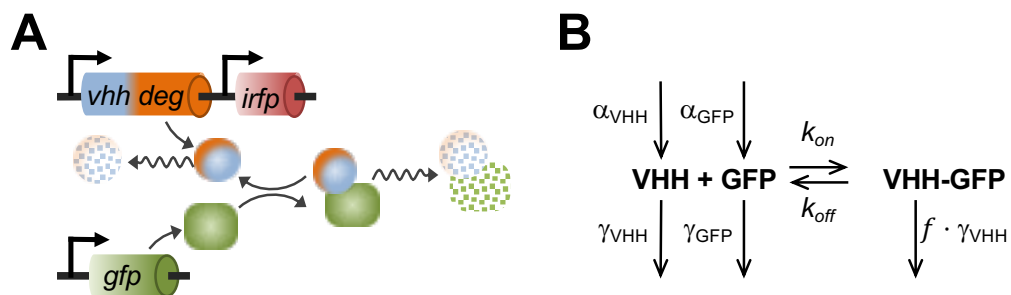


Figure 1.1 The NanoDeg Platform. (A) Schematic representation of the NanoDeg platform. (B) Mechanism of NanoDeg-mediated degradation of GFP. The reaction is

based on synthesis of VHH and GFP (rates α_{VHH} and α_{GFP}), formation of VHH–GFP complex (association rate constant k_{on} and dissociation rate constant k_{off}), degradation of VHH and GFP (rates γ_{VHH} and γ_{GFP}), and degradation of VHH–GFP complex (rate $f \cdot \gamma_{\text{VHH}}$, where f is a degradation coefficient).

A predictive, mathematical model of NanoDeg-mediated depletion of GFP was developed and experimentally validated. This model describes the concentration of VHH, GFP and the VHH-GFP complex as dependent on the species-specific rates of synthesis (α) and degradation (γ), and on the rate of dilution due to cell division (μ). The model is based on the assumptions that (1) the rate of degradation of VHH is determined by the specific degron used to build the NanoDeg, (2) VHH binds reversibly to GFP, and (3) the rate of degradation of the VHH-GFP complex is proportional to that of VHH (Figure 1.1B). The model was validated by modulating the most sensitive parameters: the rate of synthesis of VHH (α_{VHH}), the rate of synthesis of GFP (α_{GFP}), and the rate of degradation of VHH (γ_{VHH}). Equipped with a predictive model for controlling cellular protein levels, The NanoDeg is a powerful, plug-and-play platform that provides exquisite control of target protein depletion.

In this thesis, I have employed post-translational protein regulation via engineered nanobodies to achieve dynamic and spatial control over cellular proteins. I first illustrate the use of the NanoDeg platform to improve the dynamic range and temporal resolution of input-dependent reporter systems. This was achieved by integrating a reporter specific NanoDeg into a genetic circuit through a feedforward loop to generate an improved heat-shock reporter system. To enhance temporal control of genetic networks, I investigated strategies to use the NanoDeg

5

to control the oscillatory behavior of a range of different circuit topologies. Finally, I developed a nanobody-based platform to control the subcellular localization of target proteins (NanoLoc). I experimentally demonstrated the use of this platform to selectively localize a target to multiple cellular compartments and investigated different circuit architectures for dynamic control of target localization to different compartments. Combining nanobody-mediated localization and degradation with orthogonal transcriptional regulation I developed a nanobody-based toolkit to achieve spatial and temporal control of target protein levels.

Objectives

The overarching goal of this study was to generate synthetic post-translational tools that provide temporal and spatial control over cellular proteins and can be generally used to characterize and manipulate mammalian genetic networks.

Objective 1: Enhancing the dynamic resolution of input-responsive reporter systems through input-dependent post-translational control of the reporter output. The use of synthetic orthogonal circuits for detection of dynamic cellular behaviors has been limited by the remarkable stability of conventional reporters. While providing an appealing feature for signal detection, the long half-life of reporters such as GFP is typically not ideal to measure transient signals and dynamic behaviors. The goal of this study was to use post-translational regulation for the design of input-dependent circuits that produce output signals with enhanced dynamic range and superior dynamic resolution of the input. This goal

was achieved using the NanoDeg to attain input-dependent depletion of a GFP reporter. To identify the ideal circuit architecture that allows placing both the GFP output and the GFP-specific NanoDeg under control of a common input, feedforward loop topologies were explored and compared to conventional reporters directly controlled by the input. The topologies explored provide regulation of GFP levels not only through input-dependent transcriptional activation but also input-dependent degradation. The coherent-feedforward loop topology was found to provide ideal features and was implemented experimentally by building a heat-sensitive reporter. The design features of this circuit that result in detection of the cell response with maximal output dynamic range and dynamic resolution of the heat shock were also explored. The method reported provides the design rules of a novel synthetic biology module that will be generally useful to build complex genetic networks for enhanced detection of highly dynamic behaviors.

Objective 2: Controlling the dynamic behavior of oscillatory genetic networks through post-translational modulation of network components.

Many essential functions in biological systems, including cell cycle progression and circadian rhythm regulation, are governed by periodic behaviors of specific biomolecules. These periodic behaviors arise from the precise arrangement of components in biomolecular networks that generate oscillatory output signals. The dynamic properties of individual components of these networks, such as maturation delay and degradation rates, often play a key role in determining the network oscillatory behavior. The goal of this study was to explore the post-translational modulation of network components to generate and perturb oscillatory behaviors.

8

To achieve this goal, I used the NanoDeg platform to control the degradation rates of network components and predicted the effect of post-translational depletion of network components on the behavior of a series of proto-oscillating network topologies. I modeled the behavior of two main classes of oscillator topologies, relaxation oscillators (the activator-repressor and the Goodwin oscillator) and ring oscillator (repressilators). I identified two main mechanisms by which non-oscillating networks could be induced to oscillate by post-translational modulation of network components: increasing the separation of timescales and mitigating the leaky expression of network components. This work demonstrates control of protein degradation rates as a strategy to modulate existing oscillatory signals and construct oscillatory networks, and the NanoDeg provides the means to experimentally achieve facile, post-translational regulation of protein degradation rates. This work also establishes a framework to explore the use of existing tools for post-translational perturbations of biomolecular networks to generate specific oscillatory network behaviors.

Objective 3: Developing a platform for spatial and temporal control of cellular proteins through post-translational control of target localization and degradation. Mammalian cells process information through coordinated spatiotemporal regulation of proteins. Engineering cellular networks thus relies on efficient tools for regulating protein levels in specific subcellular compartments. To address the need to manipulate the extent and dynamics of protein localization, I developed a platform technology for target-specific control of cellular destination. This platform is based on bifunctional molecules comprising a target-specific

9

nanobody and universal sequences determining target subcellular localization or degradation rate. I demonstrated that nanobody-mediated localization depends on the expression level of the target and the nanobody, and the extent of target subcellular localization can be regulated by combining multiple target-specific nanobodies with distinct localization or degradation sequences. I also show that this platform for nanobody-mediated target localization and degradation can be regulated transcriptionally and integrated within genetic circuits to achieve the orthogonal control over spatial regulation of target proteins.

Input-dependent post-translational control of the reporter output enhances dynamic resolution of mammalian signaling systems

This work is published in Methods in Enzymology (Jayanthi, B., Zhao, W., and Segatori, L. Input-dependent post-translational control of the reporter output enhances dynamic resolution of mammalian signaling systems. Methods in enzymology 2019, 622, 1-27.)

3.1. Introduction

Green fluorescent protein (GFP) is widely used to quantify gene expression in live cells [39], [40]. The gene encoding GFP is typically placed under control of a

regulated promoter that is sensitive to a specific environmental cue or intracellular signal [41], [42] and cellular fluorescence monitored to obtain a quantitative measurement of the promoter activity. As most commonly used reporters, whether fluorescent, luminescent, or enzymatic, GFP is a highly stable protein with a reported half-life of ~26 hours [43], which is generally useful for detection of stimuli of limited intensity. In many cell types, however, GFP half-life is greater than the cell doubling time, resulting in decay of the fluorescence signal that is often governed by dilution due to cell division, rather than by changes in promoter activity, and that fails to provide an accurate measurement of the input dynamics. As a result, GFP is not an ideal reporter for monitoring the response time of transient signals, particularly when focusing on the dynamic behavior associated with removal of the input [44], [45]. Furthermore, ideal reporter systems generate output signals with large dynamic range, which facilitates detection of small, but often biologically relevant changes in gene expression [46]–[48]. The high basal expression characteristic of many mammalian signaling networks limits the dynamic range of reporter systems designed to interface with the signaling input [49]. Moreover, in situations where the basal expression is high, GFP stability can lead to protein crowding that has the potential to effect the correlation between GFP concentration and GFP fluorescence [50].

To improve the sensitivity of GFP as a reporter of dynamic cellular behaviors, reduced half-life variants such as destabilized GFP variants (dGFP) have been generated by fusing GFP to destabilizing tags or protein signaling domains that

confer susceptibility to degradation to the resulting fusion protein [13], [43]. As a result, reporter systems based on the reduced half-life dGFP present faster response times [13], [43], [51]–[54]. The use of unstable GFP variants results in shorter times to reach steady state compared to stable GFP and does not usually affect the signal dynamic range, as the reduction in GFP steady-state levels is independent of the system dynamics [55], [56]. Destabilized GFP variants may lead to enhancement of the output dynamic range in cases where the input is applied for a time interval shorter than that needed for GFP levels to reach steady state, but they typically produce low absolute signal outputs [57], which are not ideal for sensing applications. These observations point to the need for novel circuit design strategies to enhance dynamic resolution of the input without sacrificing the output dynamic range.

In the present chapter, I investigated the use of input-regulated, NanoDeg-mediated control of GFP levels to improve the design of input-dependent circuits. Because post-translational control of GFP mediated by the NanoDeg occurs over timescales faster than the transcriptional events mediating GFP expression [8], I explored strategies for integration of the NanoDeg into input-dependent circuits with the ultimate goal to attain input-dependent post-translational control of GFP levels. To this end, I explored feedforward loops, which are a class of network motifs frequently observed across biological systems [58] and comprise two parallel input-controlled regulation paths. Each feedforward loop affects the output through a direct and an indirect regulation path [59]. Feedforward loops can be further

classified as coherent or incoherent. In coherent feedforward loops (CFFLs), the direct and indirect regulation paths have the same effect on the output. In incoherent feedforward loops (IFFLs), the two paths are based on opposite regulatory mechanisms, resulting in antagonistic effects on the output [59]. Such feedforward motifs constitute the simplest circuit topologies that allow integrating transcriptional and post-translational control of GFP. This dual control results in direct input-dependent control of GFP and indirect input-dependent control of the NanoDeg, such that post-translational regulation of the GFP output mediated by the NanoDeg is under control of the input.

Herein, mathematical modeling analyses revealed optimal integration of the NanoDeg can be achieved through a CFFL leading to a NanoDeg Inverter configuration that improves both the output response time and dynamic range. This topology was experimentally implemented by building a cell based sensor of moderate hyperthermia based on a minimal heat-shock promoter derived from the human *hsp70B* gene [60]–[62].

3.2. The NanoDeg as a module for genetic circuits

While the NanoDeg platform is potentially useful to investigate the function of any cellular protein through the design of NanoDeg derivatives based on target-specific VHHs and degron with desired degradation rate, the GFP-specific NanoDeg can be specifically used to modulate GFP levels in the context of synthetic networks

designed to link GFP output to complex dynamic behaviors. The output signal of gene circuits typically provides an accurate measurement of the input-dependent activation kinetics. The output decay, however, is likely to depend on the reporter's half-life, with stable reporters providing poor indicators of the input decay [40]. Reducing the reporter's half-life via genetic engineering partly alleviates this issue, but also significantly reduces the concentration of the reporter, which may affect detection [57]. To enhance dynamic control of a GFP reporter and generate a reporter that recapitulates the input dynamics with high fidelity, I integrated the NanoDeg within an input-dependent circuit generating a GFP output signal.

I compared the GFP output of conventional reporters based on expression of GFP (Figure 3.1 Schematic representation of genetic network motifs. (A) Direct GFP reporter. (B) Direct destabilized GFP (dGFP) reporter. (C) NanoDeg Activator topology based on the IFFL motif. (D) NanoDeg Inverter topology based on the CFFL motif. Arrows indicate a positive regulation; blunt lines indicate negative regulation. A) or dGFP (Figure 3.1B) under the control of the input, to the simplest topologies designed to place the NanoDeg, in addition to GFP, under the control of the input through the use of feedforward loops (Figure 3.1C and D).

Integrating the NanoDeg under the control of a positive transcriptional regulator that is, in turn, transcriptionally activated by the input results in an IFFL-based circuit (NanoDeg Activator) that mediates input-dependent activation of GFP expression and input-dependent activation of an activator of the NanoDeg (Figure

3.1C). IFFLs are commonly found in biological signaling networks that provide adaptive response [63], [64]. The NanoDeg Activator topology could thus be used to engineer circuits with IFFL-like behavior based on post-translational regulation to accurately investigate the adaptive response to biologically relevant stimuli.

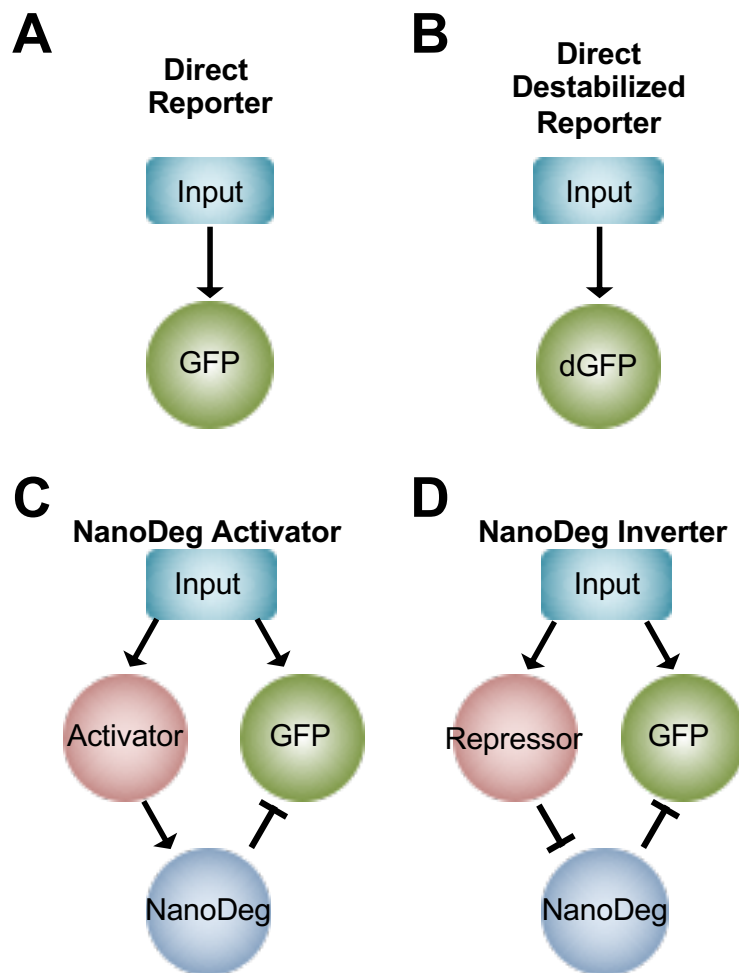


Figure 3.1 Schematic representation of genetic network motifs. (A) Direct GFP reporter. (B) Direct destabilized GFP (dGFP) reporter. (C) NanoDeg Activator

topology based on the IFFL motif. (D) NanoDeg Inverter topology based on the CFFL motif. Arrows indicate a positive regulation; blunt lines indicate negative regulation.

The NanoDeg can also be integrated through an inverter topology such that the NanoDeg is under the control of a negative transcriptional regulator that is, in turn, transcriptionally activated by the input. The NanoDeg Inverter results in input-dependent activation of GFP expression and input-dependent activation of a repressor of the NanoDeg, thus generating a CFFL-based circuit that leads to inversion of NanoDeg expression with respect to the input (Figure 3.1D). The CFFL of the NanoDeg Inverter topology results in a two-branched input-dependent mechanism of GFP control: direct GFP activation and direct repressor activation followed by indirect NanoDeg repression. As discussed above, the stability of GFP limits its use as a reporter of biological behaviors characterized by fast turnover of relevant components [65]. The two-branched NanoDeg Inverter topology, on the other hand, is expected to ensure fast turnover of the GFP reporter through NanoDeg-mediated degradation, while maintaining a large dynamic range of the GFP output signal.

3.2.1. Mathematical model of input-dependent NanoDeg reporter circuits

The NanoDeg-based circuit topologies were first compared by simulating the GFP output of each topology given an input of fixed duration and intensity using a mathematical model based on ordinary differential equations describing the concentration of the species involved [66]. All species concentration profiles were

derived as dependent on rate of synthesis (α), rate of degradation (γ), and rate of cell dilution due to cell growth (μ). The input was introduced using a generalized inducible promoter model with exponential transitions between basal expression (P_{off}) and maximum expression (P_{max}) that follow a rate of activation (β_A) from basal to maximum activity induced by an input of duration (τ) and a rate of deactivation (β_D) from the maximum to basal activity after removal of the input (Equation 3.2.1). The input was simulated through the activation of an inducible promoter that controls the expression of GFP by affecting the rate of synthesis (α_{GFP}). The direct reporter configurations (Figure 3.2A and B) were evaluated by modeling the expression of GFP as the product of the rate of synthesis and a coefficient that accounts for the effect of the inducible promoter ($P_{on} \cdot \alpha_{GFP}$) (Equation 3.2.2). The direct reporter based on the dGFP was modeled by adjusting GFP degradation rate.

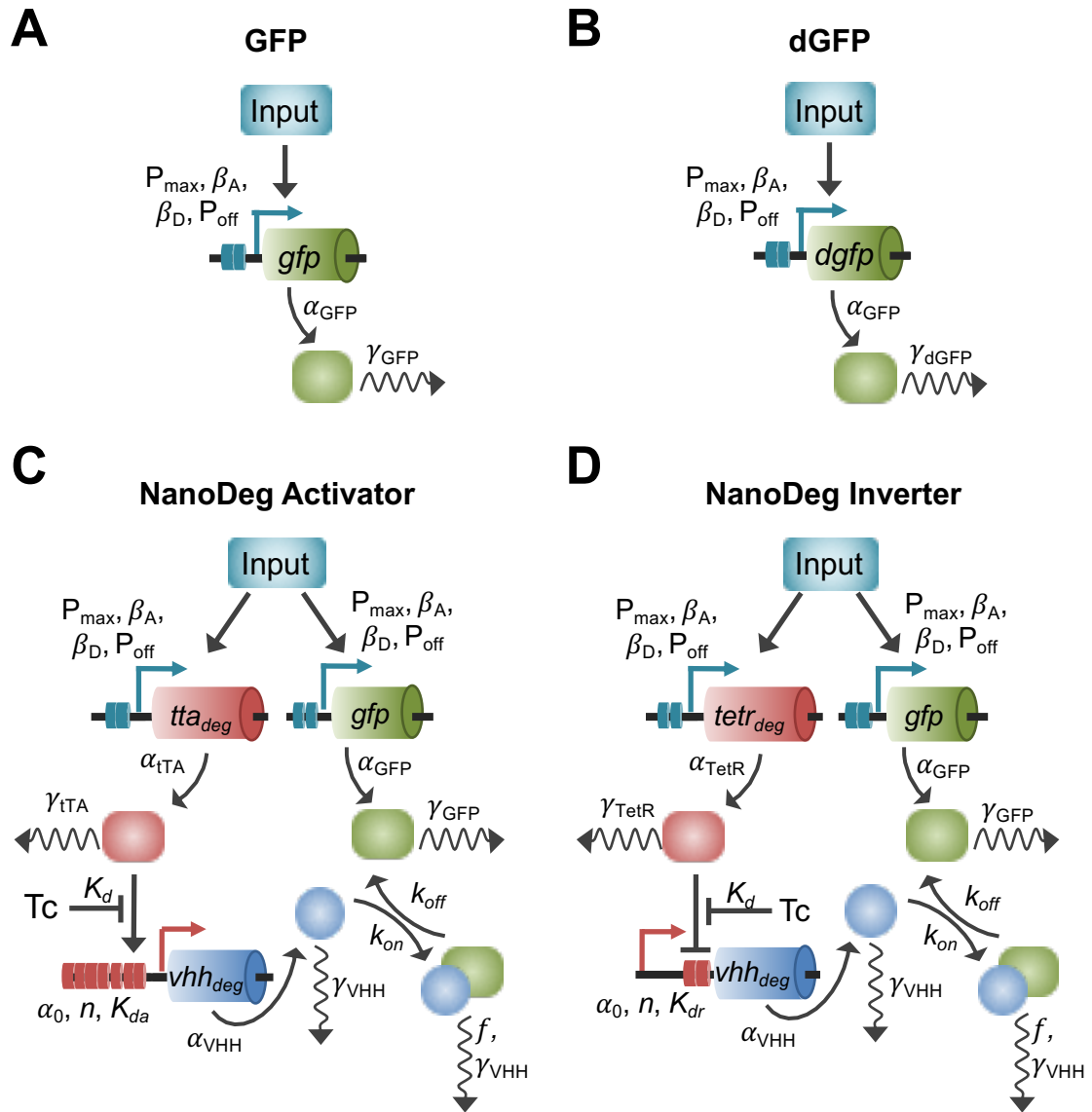


Figure 3.2 Mathematical model of the genetic network motifs. Diagrams of the models used in this work. The input is modeled assuming an inducible promoter with basal activity (P_{off}), maximal activity (P_{\max}), activation rate (β_A), and deactivation rate (β_D). (A) In the direct GFP reporter, GFP depends on the synthesis rate α_{GFP} and degradation rate γ_{GFP} . (B) In the dGFP reporter, dGFP depends on the synthesis rate α_{GFP} and degradation rate γ_{dGFP} . (C) In the NanoDeg Activator reporter, both GFP and tTA_{deg} are under control of an inducible promoter and depend on the synthesis rates α_{GFP} and α_{tTA} , and degradation rates γ_{tTA} and γ_{GFP} . The expression of the VHH depends on α_0 , tTA_{deg} -TO binding with cooperativity n and equilibrium dissociation constant K_{da} , tTA_{deg} -Tc binding with equilibrium dissociation constant K_d , and degradation with rate γ_{VHH} . The expression of GFP and VHH is also affected by formation of the VHH-GFP complex with association rate constant k_{on} and

dissociation rate constant k_{off} , and degradation of the VHH-GFP complex with rate $f \cdot \gamma_{VHH}$. (D) In the NanoDeg Inverter reporter, both GFP and TetR_{deg} are under control of an inducible promoter and depend on the synthesis rates α_{GFP} and α_{TetR} , and degradation rates γ_{GFP} and γ_{TetR} . The expression of the VHH depends on α_0 , TetR_{deg}-TO binding with cooperativity n and equilibrium dissociation constant K_{dr} , TetR_{deg}-Tc binding with equilibrium dissociation constant K_d , and degradation with rate γ_{VHH} . The expression of GFP and VHH is also affected by formation and degradation of the VHH-GFP complex as in C.

The NanoDeg Activator topology (Figure 3.2C, Equation 3.2.3) was evaluated by modeling the expression of both GFP and the tetracycline transactivator (tTA) [67] as dependent on their rate of synthesis ($P_{on} \cdot \alpha_{GFP}$ and $P_{on} \cdot \alpha_{tTA}$), with GFP also being affected by association and dissociation of VHH and GFP governed by the rate constants k_{on} and k_{off} . The expression of the NanoDeg was modeled as dependent on the rate of synthesis regulated by tTA following a Hill Function for an activator with Hill Coefficient (n), rate of synthesis due to leakiness (α_0), and equilibrium dissociation constant of tTA binding to the TO sequence (K_{da}) [68]. The NanoDeg concentration profile is also dependent on the rate of association and dissociation of the VHH-GFP complex.

The NanoDeg Inverter topology (Figure 3.2D, Equation 3.2.4) was evaluated using a similar approach with the expression of GFP and the tetracycline repressor (TetR) dependent on their rate of synthesis ($P_{on} \cdot \alpha_{GFP}$ and $P_{on} \cdot \alpha_{TetR}$), and with GFP also affected by association and dissociation of VHH and GFP governed by the rate constants k_{on} and k_{off} . The expression of the NanoDeg was modeled as dependent on the rate of synthesis regulated by TetR following a Hill Function for a repressor with Hill Coefficient (n), rate of synthesis due to leakiness (α_0), and equilibrium

dissociation constant of TetR binding to the TO sequence (K_{dr}). The NanoDeg concentration profile is also dependent on the rate of association and dissociation of the VHH-GFP complex.

The NanoDeg-based circuits should be based on short half-life transcriptional regulators (TetR and tTA) to ensure that GFP output dynamics reflects the nature of the input and is not controlled by the half-life of the regulators. The degradation rate of TetR and tTA was thus modeled as the expected degradation rate of ODC(D12A)-tagged TetR and tTA variants [37]. Other short half-life components (*i.e.*, the VHH and dGFP) were also modeled as having the degradation rate of an ODC(D12A)-tagged derivative.

Equation 3.2.1 Input-dependent promoter activity.

$$P_{on}(t) = \begin{cases} P_{off} & t < t_0 \\ P_{off} + (P_{max} - P_{off})(1 - e^{-\beta_A(t-t_0)}) & t_0 < t < \tau + t_0 \\ P_{off} + (P_{on}(\tau) - P_{off})e^{-\beta_D(t-(\tau+t_0))} & t > \tau + t_0 \end{cases}$$

Equation 3.2.2 Direct Reporter topologies.

$$\frac{d[GFP]}{dt} = \alpha_{GFP} \cdot P_{on}(t) - (\gamma_{GFP/dGFP} + \mu)[GFP]$$

Equation 3.2.3 The NanoDeg Activator topology.

$$\frac{d[GFP]}{dt} = \alpha_{GFP} \cdot P_{on}(t) - (\gamma_{GFP} + \mu)[GFP] - k_{on}[VHH][GFP] + k_{off}[VHH:GFP]$$

$$\frac{d[tTA]}{dt} = \alpha_{tTA} \cdot P_{on}(t) - (\gamma_{tTA} + \mu)[tTA]$$

$$\frac{d[VHH]}{dt} = \alpha_{VHH} \cdot pTRE \left(\frac{[tTA]^n + \frac{\alpha_0}{\alpha_{VHH}} \cdot K_{da}^n}{K_{da}^n + [tTA]^n} \right) - (\gamma_{VHH} + \mu)[VHH] - k_{on}[VHH][GFP] + k_{off}[VHH:GFP]$$

$$\frac{d[VHH:GFP]}{dt} = k_{on}[VHH][GFP] - k_{off}[VHH:GFP] - (f \cdot \gamma_{VHH} + \mu)[VHH:GFP]$$

Equation 3.2.4 The NanoDeg Inverter topology.

$$\frac{d[GFP]}{dt} = \alpha_{GFP} \cdot P_{on}(t) - (\gamma_{GFP} + \mu)[GFP] - k_{on}[VHH][GFP] + k_{off}[VHH:GFP]$$

$$\frac{d[TetR]}{dt} = \alpha_{TetR} \cdot P_{on}(t) - (\gamma_{TetR} + \mu)[TetR]$$

$$\frac{d[VHH]}{dt} = \alpha_{VHH} \cdot pTO \left(\frac{1 + \frac{\alpha_0}{\alpha_{VHH}} \left(\frac{[TetR]}{K_{dr}} \right)^n}{1 + \left(\frac{[TetR]}{K_{dr}} \right)^n} \right) - (\gamma_{VHH} + \mu)[VHH] - k_{on}[VHH][GFP] + k_{off}[VHH:GFP]$$

$$\frac{d[VHH:GFP]}{dt} = k_{on}[VHH][GFP] - k_{off}[VHH:GFP] - (f \cdot \gamma_{VHH} + \mu)[VHH:GFP]$$

Parameter	Description	Value	Source
P_{max}	Inducible promoter maximum activity	36	[69], [70]
P_{off}	Inducible promoter basal activity	3.6	This work
β_A	Inducible promoter activation rate	5 nM h ⁻¹	Arbitrary value
β_D	Inducible promoter deactivation rate	1 nM h ⁻¹	Arbitrary value
P_{on}	Inducible promoter activity at time t	Variable	This work
α_{GFP}	GFP synthesis rate	1 nM h ⁻¹	Assuming synthesis rate is equal to P_{on} (Equation 3.2.1)
γ_{GFP}	GFP degradation rate	0.0267 h ⁻¹	[70]
μ	Cell dilution rate	0.0385 h ⁻¹	[70]
γ_{dGFP}	dGFP degradation rate	0.7534 h ⁻¹	[37]
α_{VHH}	VHH synthesis rate	281 nM h ⁻¹	[37]
γ_{VHH}	VHH degradation rate	0.7534 h ⁻¹	[37]

k_{on}	VHH-GFP association rate constant	2.7648 nM ⁻¹ h ⁻¹	[37]
k_{off}	VHH-GFP dissociation rate constant	0.6264 h ⁻¹	[37]
f	Degradation coefficient of VHH _{ODC} -GFP complex	0.414	[37]
α_{tTA}	tTA synthesis rate	1 nM h ⁻¹	Assuming synthesis rate is equal to P_{on} (Equation 3.2.1)
α_{0-tTA}	Leakiness of inducible VHH	5 nM h ⁻¹	[70]
n_{tTA}	Cooperativity of tTA-TO binding	2	[70]
K_{da}	tTA-TO equilibrium dissociation constant	3.0 nM	[70]
α_{TetR}	TetR synthesis rate	1 nM h ⁻¹	Assuming synthesis rate is equal to P_{on} (Equation 3.2.1)
α_{0-TetR}	Leakiness of repressible VHH	5 nM h ⁻¹	[70]
n_{TetR}	Cooperativity of TetR-TO binding	2	[70]
K_{dr}	TetR-TO equilibrium dissociation constant	3.0 nM	[70]

Table 3.2.1 Parameters used in input-dependent NanoDeg circuit simulations

The basal steady-state levels of GFP (in the absence of input) were used as initial conditions for simulations of total GFP levels upon introduction of the input, which were quantified as free GFP for the direct reporters and as the sum of free GFP and VHH-GFP complex concentrations for NanoDeg Inverter and NanoDeg Activator topologies. All topologies were simulated by evaluating GFP output as a function of time with the input introduced at $t = 5$ hours for $\tau = 75$ hours, and using the parameters listed in Table 3.2.1 (Figure 3.3A). GFP dynamic range was calculated

by normalizing the GFP levels at each time point to the GFP levels immediately before introduction of the input for each circuit (Figure 3.3B).

As expected, the GFP signal of the reporter based on dGFP presents improved dynamic resolution of the input decay and reduced absolute output signal compared to the reporter based on stable GFP. Specifically, the dGFP based reporter displays a 6-fold reduction in the response time (defined as the time of decay to half of the maximum GFP levels) at the expense of a marked reduction in absolute GFP levels (Figure 3.3A). The dynamic range did not differ significantly between the two reporters as it arises from a proportional reduction in both induced and non-induced (basal) levels of dGFP compared to stable GFP (Figure 3.3B).

The NanoDeg Activator and NanoDeg Inverter topologies are designed to achieve input-mediated control of GFP at the post-translational level: input-induced activation of GFP degradation through the NanoDeg Activator topology and input-induced repression of GFP degradation through the NanoDeg Inverter topology. In the NanoDeg Activator configuration, activation of NanoDeg-mediated degradation results in dramatic reduction in GFP steady-state levels compared to the direct GFP reporter (**Error! Reference source not found.A**).

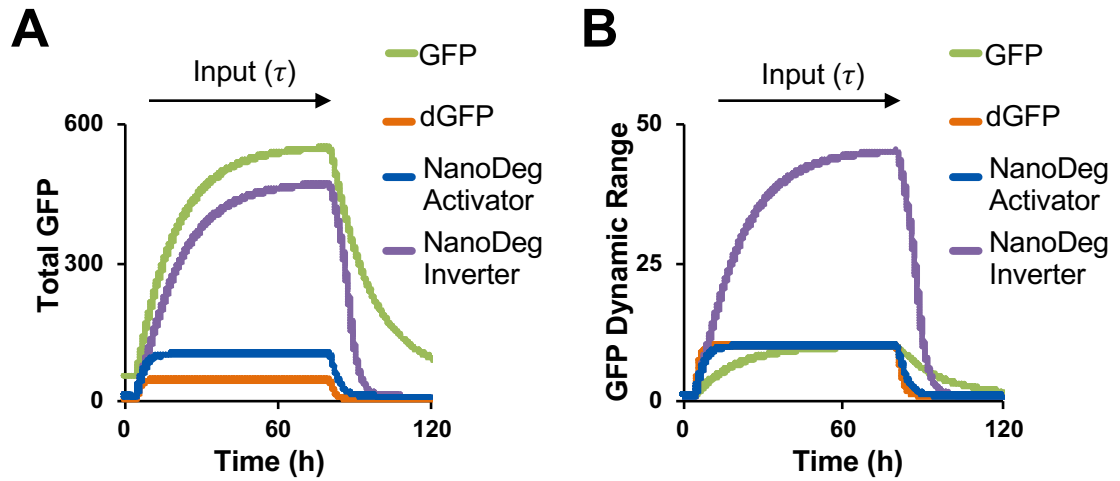


Figure 3.3 Comparison of network motifs. (A) Total GFP output of the topologies modeled as described in Figure 3.2 simulated using Matlab. GFP expression was simulated for 120 hours with a 75 hour input duration (τ , indicated with an arrow) starting at time $t = 5$ hours. Steady-state levels of GFP in the absence of the input were used as initial conditions. Total GFP is calculated as either free GFP (for GFP and dGFP), or as the sum of free GFP and VHH-GFP complex (for the NanoDeg Activator and NanoDeg Inverter). **(B)** GFP dynamic range of the topologies modeled as shown in Figure 3.2 simulated as described in A and calculated by normalizing the total GFP values to the total GFP in the absence of the input.

Because the basal GFP levels are also reduced, the dynamic range of GFP output upon introduction of the input is comparable to that of the direct reporter. The response time of the NanoDeg Activator circuit, however, is significantly improved compared to the direct GFP reporter due to post-translational depletion of GFP resulting in GFP decay similar to that of the dGFP reporter (Figure 3.3B).

Repression of NanoDeg-mediated degradation in the NanoDeg Inverter configuration results in GFP steady-state levels comparable to those of the direct GFP reporter upon induction of the system, and reduced GFP levels under basal conditions and upon removal of the input (Figure 3.3A), which improves the output

dynamic range dramatically (Figure 3.3B). Moreover, NanoDeg-mediated degradation also improves the output response time due to post-translation depletion of GFP (Figure 3.3A and B).

In summary, the NanoDeg Inverter configuration provides a topology that enhances the dynamic range of an input-dependent output and dynamic resolution of the input.

3.3. Design rules of the NanoDeg Inverter circuit topology

To define design rules of the NanoDeg Inverter topology, I performed a global sensitivity analysis and quantified the parameter sensitivities (Figure 3.4A). The global sensitivity analysis allows characterizing the response of the GFP output to perturbations in the circuit parameters, ultimately informing design optimization. To this end, the model was simulated in the COPASI software [71]. Parameters identified based on the sensitivity analysis that could be actually altered experimentally, such as tetracycline (Tc) dosage, or through alterations in the circuit design, such as the NanoDeg and TetR synthesis and degradation rates, were further explored. Simulations of the NanoDeg Inverter circuit were conducted to characterize the dynamic range (total GFP normalized to total GFP in the absence of the input) and the response time (time to decay to half of the maximum GFP levels) in response to alterations in Tc dosage, the NanoDeg degradation rate, TetR

synthesis and degradation rates, and the concentration of TO sequences (Figure 3.4B-F).

Analysis of GFP dynamic range as a function of the rates of degradation of VHH and TetR (γ_{VHH} and γ_{TetR}) revealed the design constraints of the NanoDeg Inverter circuit (Figure 3.4B). There appear to be lower and upper thresholds of γ_{VHH} , beyond which γ_{TetR} does not affect the output dynamic range and an optimum γ_{TetR} within these limits. Low γ_{TetR} values are expected to result in repression of the NanoDeg, effectively generating a circuit regulated by TetR half-life, and resulting in a behavior that approaches that of the direct GFP reporter. Large γ_{TetR} values, on the other hand, are expected to eliminate input-mediated control of NanoDeg expression, effectively placing GFP output under control of a constitutively expressed NanoDeg and resulting in a behavior that approaches that of the direct dGFP reporter (Figure 3.4B).

Analysis of GFP response time as a function of the rates of degradation of VHH and TetR (γ_{VHH} and γ_{TetR}) confirmed that the response time is largely affected by γ_{TetR} (Figure 3.4C), which is in agreement with the notion that rapid degradation of TetR upon removal of the input results in rapid expression of the NanoDeg and depletion of residual GFP. These results point to a potential tradeoff between response time and dynamic range of the system (Figure 3.4B and C) and the need to carefully tune γ_{TetR} and γ_{VHH} to avoid deregulated depletion of GFP, which enhances the output response time at the expense of the output dynamic range.

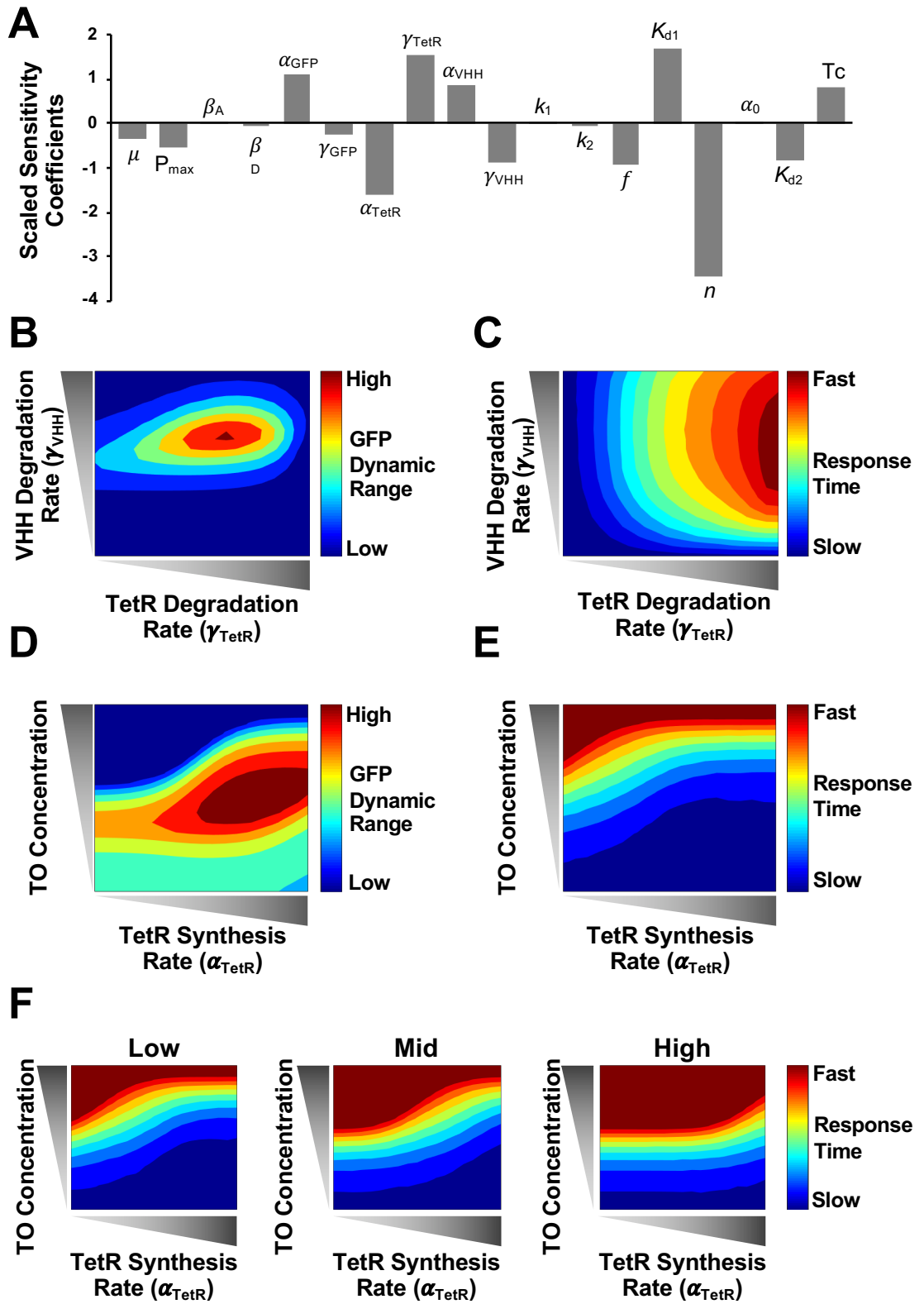


Figure 3.4 Design rules of the NanoDeg Inverter topology. (A) Sensitivity of GFP output to perturbations in the NanoDeg Inverter parameters. The sensitivity analysis was performed using COPASI software with default parameter step size. (B-F) GFP levels of the NanoDeg Inverter simulated for 120 hours. The input is introduced at time $t = 5$ hours for 75 hours. (B) GFP Dynamic Range as a function of NanoDeg degradation rate (γ_{VHH}) and TetR degradation rate (γ_{TetR}). GFP Dynamic Range was calculated by normalizing the total GFP levels upon exposure to the input to the total GFP levels prior to exposure to the input. (C) GFP response time as a function of NanoDeg degradation rate (γ_{VHH}) and TetR degradation rate (γ_{TetR}). The response time was calculated as the time to decay to half of the maximum total GFP value. (D) GFP Dynamic Range as a function of the TO concentration (which is proportional to the maximum α_{VHH}) and TetR synthesis rate (α_{TetR}). (E) GFP response time as a function of TO concentration and TetR synthesis rate (α_{TetR}). (F) GFP response time as a function of TO concentration and TetR synthesis rate (α_{TetR}) in the presence of high (10^{-7} nM), mid (10^{-8} nM), and low (10^{-9} nM) Tc.

I next studied the response of the NanoDeg Inverter circuit to alterations in the rate of TetR synthesis (α_{TetR}) and the concentration of DNA operator (TO concentration), which is proportional to the maximum NanoDeg synthesis rate (Figure 3.4D). For a given value of α_{TetR} , the dynamic range increases as a function of TO concentration until a TO concentration that exceeds the TetR capacity to repress the NanoDeg, effectively approaching the behavior of the direct dGFP reporter. The threshold of TO concentration increases as α_{TetR} increases with a characteristic sigmoidal behavior. These modeling results also predict the conditions to maximize GFP dynamic range based on the optimal TO concentration for expression of the NanoDeg in the absence of the input and optimal α_{TetR} for repression of the NanoDeg in the presence of the input.

The response time is also affected by the TO concentration and TetR synthesis rate (Figure 3.4E). Generally speaking, the response time increases as a function of TO concentration due to incomplete repression of NanoDeg expression,

with the lower limit of TO concentration increasing as a function of α_{TetR} , reflecting the increase in TetR levels available for TO repression. These results point to a design tradeoff with respect to TO concentration and TetR synthesis rate and to the need to carefully tune TO concentration and α_{TetR} to ensure depletion of GFP levels in the absence of the input and efficient repression of the NanoDeg in the presence of the input.

Tc dosage affects the binding equilibrium of TetR and the TO sequence [68]. Tc dosage is thus expected to cause an apparent reduction in TetR synthesis rate, resulting in modulation of the GFP response time for a given TO concentration. Modeling prediction of the GFP response time as a function of TO concentration and TetR synthesis rate and in the presence of increasing Tc concentration confirmed that Tc dosage increases the output response time (Figure 3.4F).

3.3.1. Implementation of a heat shock-inducible NanoDeg Inverter circuit

The NanoDeg Inverter circuit was tested experimentally in cells expressing a GFP reporter of heat shock. HEK293T cells were transduced for the expression of GFP under control of the minimal *hsp70B* promoter [60]–[62] and a stable monoclonal population selected (HS-GFP cells). To verify that the NanoDeg degradation rate affects GFP response time, the decay of GFP signal was tested in the context of a series of NanoDeg Inverter circuits based on NanoDeg variants presenting mutations in the ODC tag expected to affect the NanoDeg half-life, namely ODC (1.3 hours), ODC(C20A) (10.8 hours) and ODC(D12A) (0.9 hours) [37]. HS-GFP

cells were co-transfected for the expression of (i) TetR_{ODC(D12A)} (a TetR variant expected to display fast degradation rate [37] selected to ensure TetR half-life does not affect the output dynamics) under the control of the minimal *hsp70B* promoter and linked to the expression of a near-infrared fluorescent protein (eqFP650) [72] through an internal ribosome entry site (IRES) [73], and (ii) a NanoDeg variant or the parental VHH under the control of the TetR regulated CMV promoter containing two repeats of the TO sequence downstream of the TATA box (CMV/TO) [74]. Cells were transfected with plasmids for the expression of TetR and the NanoDeg in a 10:1 ratio and exposed to the input (43°C for 90 minutes 24 hours after transfection). GFP fluorescence of eqFP650 fluorescent cells was recorded as a function of time. GFP decay rate, quantified between 12 hours and 18 hours post-induction, was found to correlate with the degradation rate of the NanoDeg (Figure 3.5A). These results confirm that the NanoDeg degradation rate affects the GFP output of the NanoDeg Inverter circuit and led to the generation of a stable cell line expressing the NanoDeg based on ODC(D12A) to implement the complete heat-shock sensitive NanoDeg Inverter circuit.

A stable HEK293T cell line expressing GFP and a degraon-tagged TetR variant under the control of a heat-shock sensitive promoter and the NanoDeg under the control of TetR was generated by first transducing HS-GFP cells to integrate a cassette containing the gene encoding VHH_{ODC(D12A)}, an IRES, and the gene encoding the infrared fluorescent protein (iRFP) [75] under control of the CMV/TO promoter.

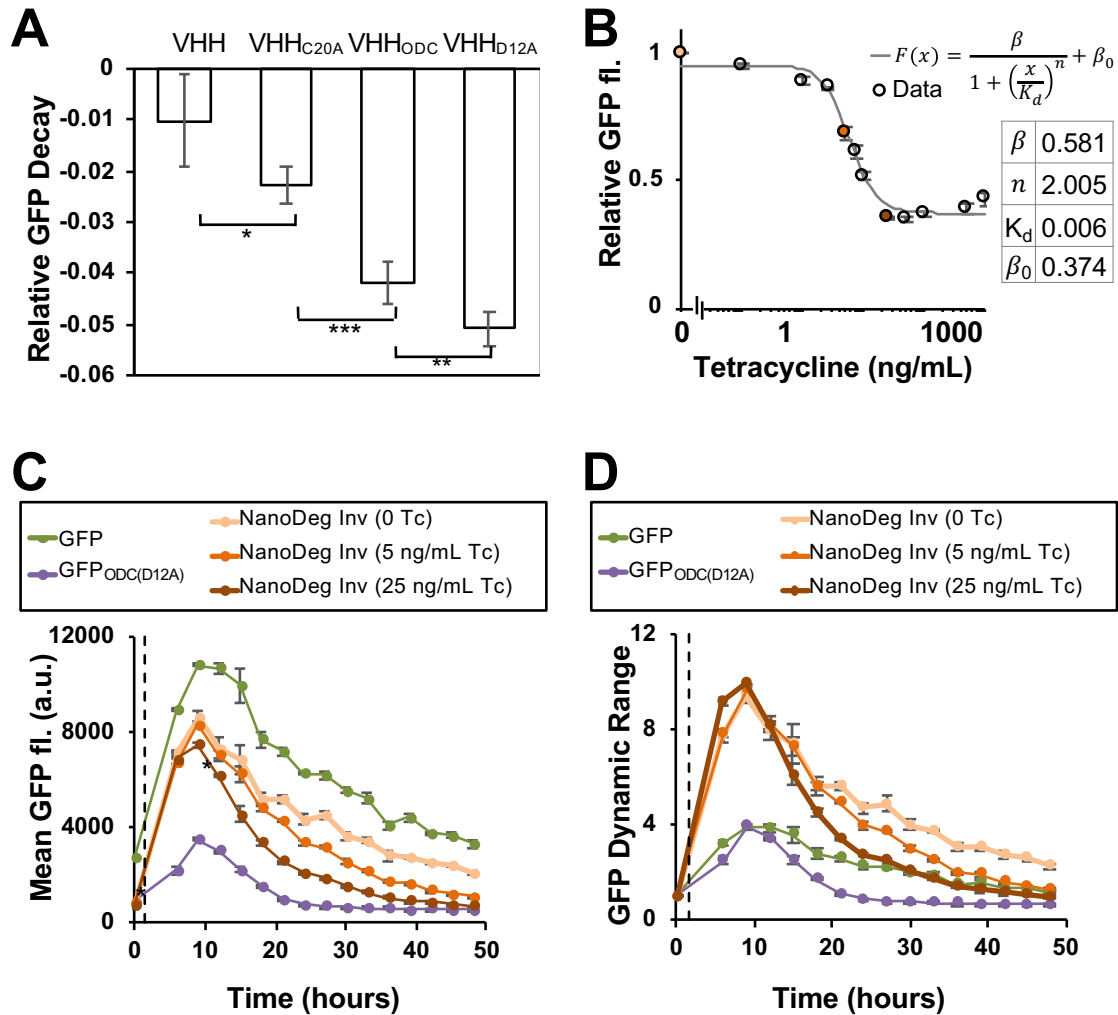


Figure 3.5 Implementation of a heat shock-inducible NanoDeg Inverter circuit. (A) GFP output of stable HEK293T cells expressing GFP under control of the minimal *hsp70B* promoter transiently transfected with TetR_{ODC(D12A)}-IRES-eqFP650 under control of the minimal *hsp70B* promoter and VHH variants under control of the CMV/TO promoter. Cells were exposed to heat-shock (90 minutes at 43°C) 24 hours post-transfection. Transfected cells were analyzed by flow cytometry at 12 hours, 15 hours, and 18 hours post-heat shock. Relative GFP values were calculated by normalizing the mean GFP values of eqFP650+ and GFP+ cells exposed to heat shock to the mean GFP values of untreated cells. The relative GFP decay was obtained by calculating the slope of the relative GFP values between 12 and 18 hours. Data are reported as mean \pm s.d. ($n = 5$, * $p < 0.05$, ** $p < 0.01$, *** $p < 0.0001$, Student's *t*-test). (B) GFP fluorescence of stable HEK293T cells expressing the heat sensitive NanoDeg Inverter circuit as a function of Tc dosage. Cells were treated with Tc for 24 hours prior to heat-shock treatment (90 minutes at 43°C). GFP fluorescence was measured by flow cytometry 24 hours post-heat shock. Relative GFP values, calculated by normalizing the GFP fluorescence of Tc-treated cells to

that of untreated cells, were fit to a Hill function using Matlab nonlinear least-squares solver. Data are reported as mean \pm s.d. (n=3). (C) GFP output of stable HEK293T cells expressing GFP or GFP_{ODC(D12A)} under control of the minimal *hsp70B* promoter, or stable HEK293T cells expressing the heat sensitive NanoDeg Inverter circuit. Cells were treated with Tc for 24 hours prior to exposure to heat-shock (90 minutes at 43°C, dashed line). Flow cytometry measurements were conducted immediately prior to heat-shock (t=0 hours) and every 3 hours between 6 and 48 hours post-heat shock. Data are reported as mean \pm s.d. (n = 3, *p < 0.001, Student's *t*-test). (D) GFP dynamic range calculated by normalizing the mean GFP values of cells treated as in (C) to the mean GFP values prior to heat shock.

Transduced cells were subsequently transduced for the expression of TetR_{ODC(D12A)}-IRES-eqFP650 under control of the minimal *hsp70B* promoter. The resulting polyclonal population was analyzed by FACS to isolate single cells exhibiting high eqFP650 signal (corresponding to high TetR_{ODC(D12A)} expression) and high iRFP signal (corresponding to high VHH_{ODC(D12A)} expression). Monoclonal populations were further screened by flow cytometry to select a monoclonal stable cell line displaying maximal GFP dynamic range (compared to the parental HS-GFP cell line not containing TetR and the NanoDeg) and sensitivity to Tc, which is expected to affect the expression of the NanoDeg and thus degradation of GFP. The resulting monoclonal cell line containing the complete NanoDeg Inverter circuit was selected for further experiments. A monoclonal cell line stably expressing dGFP (GFP_{ODC(D12A)}) under the control of the minimal *hsp70B* promoter was also generated for comparison.

3.3.2. Tuning the NanoDeg Inverter circuit

To identify the Tc dosage that maximizes the circuit sensitivity to heat shock, I measured the GFP output of HEK293T cells expressing the NanoDeg Inverter

circuit as a function of Tc concentration in the culturing medium. Cells were exposed to Tc for 24 hours, heat shocked at 43°C for 90 minutes [61], and analyzed by flow cytometry 24 hours from the initial time of exposure to heat shock to quantify GFP fluorescence (Figure 3.5B). The experimental data were fit to a Hill function for a repressor with basal expression ($F(x)$) using the least-squares method. Noticeably, the resulting Hill coefficient (n) is approximately 2, as expected for a dimeric repressor [76].

Cells expressing heat shock sensitive GFP, heat shock sensitive destabilized GFP_{ODC(D12A)}, or the heat shock sensitive NanoDeg Inverter circuit (5×10^4 cells, 24-well plates) were treated with representative concentrations of Tc (0, 5, and 25 ng/mL) for 24 hours prior to heat shock (43°C for 90 minutes). Flow cytometry measurements of GFP output as a function of time were recorded for 48 hours from the initial time of exposure to the input (Figure 3.5C and D). The maximum GFP output was reached 9 hours post-induction in all circuits and independently of the Tc dosage. The response time of the NanoDeg Inverter in the absence of Tc was similar to that of the GFP-based direct reporter (~ 15 hours). This result is expected when the concentration of TetR is in large excess compared to that of the TO sequence (see Figure 3.4D and E) and depletion of TetR to an extent that results in activation of NanoDeg synthesis is slower than the rate of degradation of GFP.

Addition of Tc is expected to decrease the pool of TetR that can bind to the TO sequence, resulting in rapid activation of NanoDeg expression upon removal of

the input. Culturing cells expressing the NanoDeg Inverter circuit in the presence of 5 ng/mL Tc decreases the response time to approximately 12 hours and does not significantly reduce the basal (0 hours) or maximum (9 hours) GFP fluorescence. Addition of higher Tc concentration (25 ng/mL), however, does significantly reduce both the basal and maximum GFP fluorescence (Figure 3.5C, $*p < 0.001$, Student's *t*-test). Treatment with 25 ng/mL Tc also further enhances the response time to approximately 9 hours, which is the same response time measured for cells expressing GFP_{ODC(D12A)}. GFP dynamic range values were obtained by normalizing the mean GFP fluorescence of each sample to the GFP signal of uninduced cells for each topology and Tc condition (Figure 3.5D). The GFP output dynamic range of cells expressing the heat sensitive NanoDeg Inverter was found to be 3-fold higher than that of cells expressing the direct (GFP) and destabilized (GFP_{ODC(D12A)}) reporters, regardless of Tc dosage. In addition, the response time of cells expressing the NanoDeg Inverter circuit exposed to Tc (25 ng/mL) (~9 hours) was found to be considerably shorter than that of cells expressing the direct GFP reporter (~15 hours) due to the rapid depletion of GFP mediated by the NanoDeg (Figure 3.5D). These results demonstrate that the NanoDeg Inverter circuit provides a robust topology for monitoring signal dynamics and can be experimentally tuned to enhance the dynamic resolution of the input.

3.4. Concluding Remarks

In this chapter, I report the development of a platform technology (NanoDeg) to achieve quantitative and predictable control of the cellular levels of a target protein [37] and the implementation of this technology to build reporter systems for detection of dynamic behaviors through input-dependent degradation of the reporter output. I investigated the design rules for integrating the NanoDeg within an input-dependent genetic circuit to achieve enhanced output dynamic range and dynamic resolution of the input, which are particularly appealing features for detection of transient behaviors that are often biologically relevant. The NanoDeg Inverter circuit described in the present study provides the first report of transcriptional and post-translational regulation combined in a synthetic coherent feedforward loop topology. Moreover, the NanoDeg Inverter circuit responds to endogenous inputs with a tunable output. This feature is particularly important for connecting individual modules to generate genetic circuits of greater complexity [77], [78] and represents a currently unmet goal in the field of synthetic biology.

Post-translational modification of degradation rates can generate oscillations in proto-oscillating biomolecular networks

4.1. Introduction

Many cellular pathways that regulate biological outcomes are controlled by molecules that exhibit periodicity in their expression or activity [79], [80].

Oscillatory processes appear in a wide variety of contexts from alternating periodic expression of CLOCK:BMAL1 and PER:CRY in circadian cycles [81] and cyclin-CDK and APC-Cdc20 in cell cycle progression [82] to the periodic transcription activation activity of p53 necessary for DNA repair upon cell irradiation [83]. Other examples of oscillatory behaviors that determine cell fate are NF- κ B regulation of the

inflammatory response [84], segmentation activity in early embryogenesis [85], neuronal stem cell differentiation [86], and deregulation of circadian cycles associated with Alzheimer's disease [87]. In all of these biological oscillators, the specific arrangement of biomolecular components gives rise to periodic behavior which is a frequent determinant of cell fate. The underlying network properties and dynamic interactions that result in such cell-fate determining oscillations, however, remain to be fully characterized. Tools and strategies that precisely initiate or perturb oscillatory behaviors would allow for the underpinnings of these endogenous networks to be defined and provide well-characterized genetic network modules for the creation of novel biological functions.

Oscillatory signals are intrinsically tied to the dynamics of individual nodes of a biomolecular network and arise from the presence of a limit cycle around an unstable equilibrium or an excitable response [88] that presents a very long transient (damped) oscillation. Both the excitable system response and the limit cycles around an unstable equilibrium are associated with systems that present a supercritical Hopf bifurcation [88]–[90] for a critical parameter of the system. Specifically, limit cycles appear when the value of the critical parameter is such that an equilibrium becomes unstable (i.e., the critical parameter “crosses” the Hopf bifurcation value) whereas the excitable response appears when the value of the critical parameter is such that the equilibrium is still stable but approaches the critical factor (i.e., the critical parameter approaches the Hopf bifurcation value). Dynamic parameters such as delays [91], [92] and degradation rates [93]–[96] are

frequently a critical parameter in Hopf bifurcations associated with the onset of oscillations in biomolecular networks. Changes to these dynamic parameters of proteins, however, require either protein engineering to modify inherent protein properties, such as maturation or degradation rates, or the use of target-specific molecules, such as small-molecule inhibitors [83]. For systems in which there are no available protein-specific molecules, there is, therefore, a substantial challenge to produce perturbations to the biomolecular network that allows the controlled study of the oscillatory behavior and its phenotypic response.

As presented in the introduction, the NanoDeg platform is a heterobifunctional molecule comprising fusion of a target-specific nanobody and a degradation signaling peptide that can direct degradation of the target with exquisite control [37]. When integrated with transcriptional regulation, the NanoDeg also allows dynamic adjustment of target protein levels without a requirement for direct manipulation of the target [97]. The NanoDeg provides a flexible platform that can be customized to target potentially any protein by modifying the nanobody and to mediate target degradation with a range of rates by altering the degradation tag. Furthermore, NanoDeg-mediated perturbations of genetic networks can be produced through transfection or viral transduction, making the NanoDeg an ideal tool to generate dynamic perturbations through facile cell engineering approaches.

In the present chapter, I aimed to explore the post-translational regulation of circuit components using the NanoDeg to create and control oscillatory networks. To this end, I explore ways to perturb systems representative of two important classes of biomolecular oscillator topologies [96], [98], relaxed feedback oscillators (the activator-repressor and the Goodwin oscillator) and ring oscillators (repressilators). The computational investigation described herein is an exploration of approaches to integrate the NanoDeg in relaxed-feedback oscillator and ring oscillator topologies and obtain insights for experimental construction of oscillator topologies and post-translational oscillation-triggering perturbations. The results obtained from the chosen examples illustrate different aspects by which post-translational modulation of topology component degradation rates can be used to trigger oscillations in the circuits. The first two subsections investigate a two-node activator-repressor topology and a single-node self-repressing Goodwin oscillator topology. Results from these relaxation oscillator examples illustrate the effect of the degradation rate of specific network components on oscillations. I then proceed to discuss the use of the NanoDeg with ring oscillators. The third subsection shows the results for a three-node repressilator topology that is perturbed by the addition of a common NanoDeg targeting all the repressilator nodes or by the addition of multiple NanoDeps where each NanoDeg targets a corresponding repressilator node. Finally, the fourth subsection shows the results for a system in which the NanoDeg behaves as one of the repressilator nodes. The results obtained for these ring-oscillator examples describe the effect of adjusting mismatched protein

concentration on non-oscillating topologies and of introducing feedback loops regulated by existing nodes.

4.2. Results

4.2.1. Activator-repressor

Activator-repressor systems are two-node genetic circuits that present a Hopf bifurcation, wherein a stable equilibrium point bifurcates into an unstable equilibrium and a stable periodic orbit upon increase in the separation of timescales between activator and repressor dynamics [88], [90]. The fundamental mechanism responsible for this transition is well captured by a two-dimensional model that describes the rate of change of the activator and repressor concentrations [93]. The activator-repressor topology considered here consists of a transcriptional activator that induces its own expression as well as that of a transcriptional repressor. The repressor, in turn, represses the expression of the activator (Figure 4.1A). To explore the effect of post-translational regulation on the behavior of the activator-repressor topology, I first built a model based on ordinary differential equations describing the concentration of the activator, the repressor, and an activator-specific NanoDeg as described in the Methods section 4.4.1. The concentrations of all species were derived as dependent on rate of synthesis and rate of degradation, with the rates of synthesis modeled as constitutive or following Hill functions [99] for an activator or a repressor and the rate of degradation either reflecting the

innate protein's half-life or the half-life of the Nano-Deg. The interaction between the NanoDeg and its target was modeled by mass-action expressions.

Onset of output oscillation requires a separation of timescales between the activator and repressor dynamics, which can be achieved when the synthesis and degradation rates of the activator are greater than that of the repressor [93], [94], [100]. I first investigated the use of the NanoDeg for triggering oscillatory behaviors in an activator-repressor topology that does not exhibit oscillation due to lack of the necessary separation of timescales between activator and repressor dynamics. Specifically, I modeled an activator-repressor topology with activator and repressor proteins exhibiting equal half-lives (i.e., degradation rates). I then introduced a NanoDeg that binds to the activator and modulates the activator's degradation rate through NanoDeg-mediated post-translational depletion (Figure 4.1A). Such an activator specific NanoDeg could be generated using an activator-specific nanobody [101], [102] or a fluorescent protein [103] or peptide tag-specific [104] nanobody upon co-expression of the activator appropriately engineered by fusion to the fluorescent protein or peptide tag. The activator-repressor output was modeled based on a short half-life NanoDeg ($\eta_N = 0.9$ h), as it was experimentally demonstrated to result in the greatest reduction in the steady-state levels of a stable target protein [37].

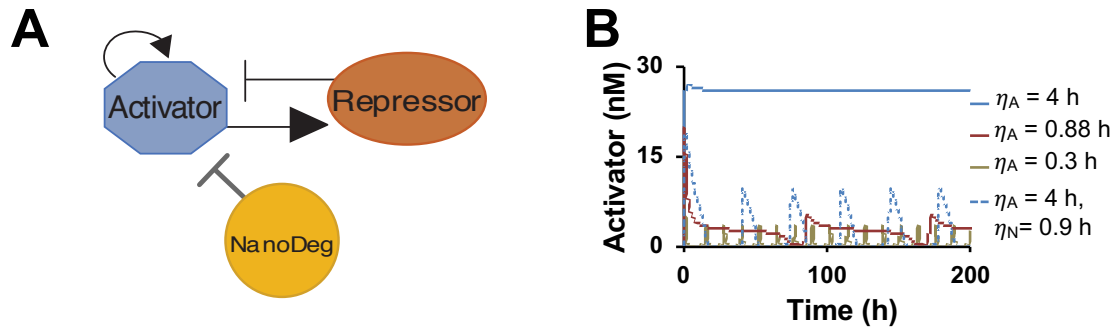


Figure 4.1 A NanoDeg modified Activator-Repressor oscillator. (A) Schematic representation of an activator-repressor oscillator incorporating an activator-targeting NanoDeg. (B) Activator protein levels of the activator-repressor topology simulated for 200 h. Half-life of the repressor (η_R) is 4 h in all simulations. Activator-repressor simulated without the NanoDeg (solid curves) and activator half-life (η_A) equal to 4 h, 0.88 h, or 0.3 h. Activator-repressor incorporating the NanoDeg (dashed curve) simulated with the activator-targeting NanoDeg half-life (η_N) equal to 0.9 h and η_A equal to 4 h.

Simulation of the activator-repressor circuit based on both the activator and the repressor exhibiting a half-life of 4 h revealed a non-oscillating output (Figure 4.1B). As expected, the system rapidly reaches a stable equilibrium due to the activator and repressor operating at similar timescales [93], [100]. Onset of oscillations in the activator-repressor lacking the NanoDeg can be achieved by decreasing the half-life of the activator to generate a timescale separation. For the chosen parameters, oscillation is triggered by lowering the half-life of the activator to at least 0.88 h, with shorter activator half-lives resulting in an increased frequency of oscillation (Figure 4.1B). Such a drastic alteration of protein half-life would be challenging to achieve experimentally, as it requires substantial modification of inherent protein properties, including fusion to protease sensitive tags or protein engineering to alter protein stability. The separation of timescales

required for oscillation, however, could be easily achieved through co-expression of an activator-specific Nano-Deg. Because introduction of the NanoDeg into the system is expected to enhance the degradation rate of the target proportionally to the NanoDeg half-life [37], oscillation of the activator-repressor circuit can be triggered by an activator-specific NanoDeg exhibiting a sufficiently short half-life (Figure 4.1B). Notably, while introducing a NanoDeg with a half-life of 0.9 h results in an output with oscillatory behavior, the same activator-repressor circuit based on an activator with half-life of 0.9 h and in the absence of the NanoDeg does not present oscillatory behavior. This result can be attributed to sequestration effects [105]–[107] as the model is based on the assumption that complex between the activator and the NanoDeg cannot bind to the activator’s cognate promoter.

To investigate the extent to which the properties of the NanoDeg influence the design of an activator-repressor circuit with oscillatory behavior based on NanoDeg-mediated control of the activator half-life, I first evaluated the circuit’s output upon modulation of the NanoDeg synthesis rate and the NanoDeg half-life. Modulation of the NanoDeg synthesis rate revealed the window of NanoDeg concentration that results in oscillatory output (3.8-9.6 nM, Figure 4.2A and B), but altering the NanoDeg concentration within this window did not have a pronounced effect on the oscillation amplitude (Figure 4.2A) or the oscillation period, with the exception of a sharp decline in oscillation period for small NanoDeg concentrations (Figure 4.2B). The lower bound of the NanoDeg concentration window corresponds to the minimum concentration of NanoDeg needed to sufficiently enhance

degradation of the activator relative to the repressor. Increasing the NanoDeg concentration above the upper bound results in excessive degradation of the activator such that the activator concentration never reaches a concentration sufficient to activate expression of the repressor. The amplitude of oscillation decreases moderately in response to increasing concentration of NanoDeg (Figure 4.2A). The moderate decrease in amplitude and the robust period (Figure 4.2A and B) in a large region of NanoDeg concentrations suggests that addition of the NanoDeg to the system triggers oscillations but modulating the NanoDeg concentration within the window of oscillation-inducing concentrations does not affect the oscillatory behavior of the circuit. Modulating the NanoDeg half life revealed the sensitivity of the oscillation period. Increasing the NanoDeg half-life results in a moderate increase in the amplitude (Figure 4.2C) and substantial increase in the period of oscillations (Figure 4.2D). Compared to the effect of the NanoDeg synthesis rate on the circuit output, the NanoDeg half-life has a more pronounced effect on the period of oscillation within the range of NanoDeg half-lives where oscillation occurs (0.3 - 1 h) (Figure 4.2C and D). This result suggests modulation of the NanoDeg half-life as a potential strategy to control the period of oscillations independently of the amplitude.

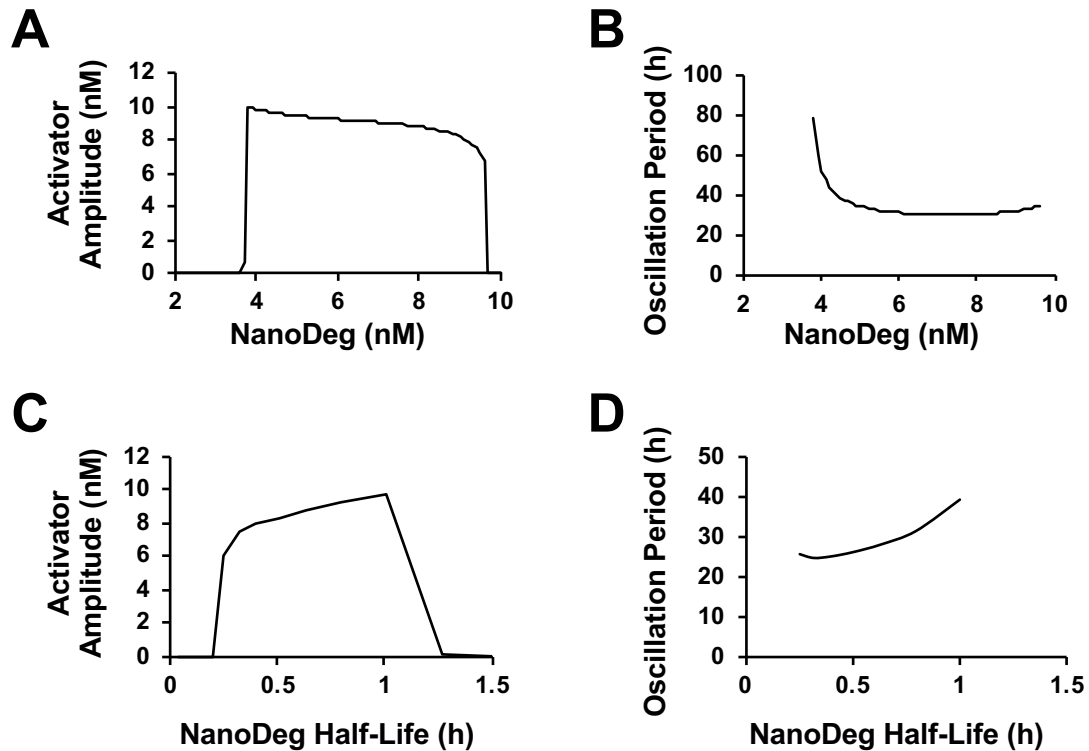


Figure 4.2 Tuning the activator-repressor with NanoDeg concentration and half-life. (A) Oscillation amplitude of the activator protein and (B) oscillation period as a function of NanoDeg concentration with $\eta_N = 0.9$ h. (C) Oscillation amplitude of the activator protein and (D) oscillation period as a function of NanoDeg half-life. NanoDeg concentration is 5 nM. Reported amplitude was calculated as the difference between the largest and the lowest concentration of the reported protein in the region of oscillation. The reported oscillation period was calculated as the zero crossings of the zero-mean trajectory in the region of oscillation.

To investigate the effect of the kinetics of the interaction between the activator and the NanoDeg on the circuit oscillatory behavior, I modulated the dissociation constant (K_d) and the rates of interaction (k_{on} and k_{off}) between the NanoDeg and the activator and evaluated oscillation amplitude and the range of NanoDeg concentrations that induce oscillation (Figure 4.3A and B). Decreasing the K_d of the interaction between the NanoDeg and activator, simulated by increasing k_{on} , results in an increase in the amplitude of oscillations. The range of NanoDeg

concentrations that induce oscillations is reduced proportionally to the decrease in K_d (e.g. $K_d * 0.1$ reduces the region of oscillation by approximately one-tenth of the initial concentration range). The minimum concentration of NanoDeg required to start oscillation is also moderately reduced with decreased K_d (Figure 4.3A).

Increasing the rate of the interaction between NanoDeg and the activator by introducing a common scaling factor (ν) to increase k_{on} ($\nu * k_{on}$) and k_{off} ($\nu * k_{off}$) and maintain K_d constant results in an increase in oscillation amplitude, a slight reduction in the minimum NanoDeg concentration needed to induce oscillation and a reduced range of NanoDeg concentrations that results in oscillations, similar to the effect of K_d on oscillations. The effect of the rate of NanoDeg and activator binding on oscillation amplitude, however, is non-linear (Figure 4.3B). These results indicate that both the affinity and the rate of the interaction between the NanoDeg and the activator should be considered in design of NanoDeg-based systems for modulation of oscillatory behavior of the activator-repressor.

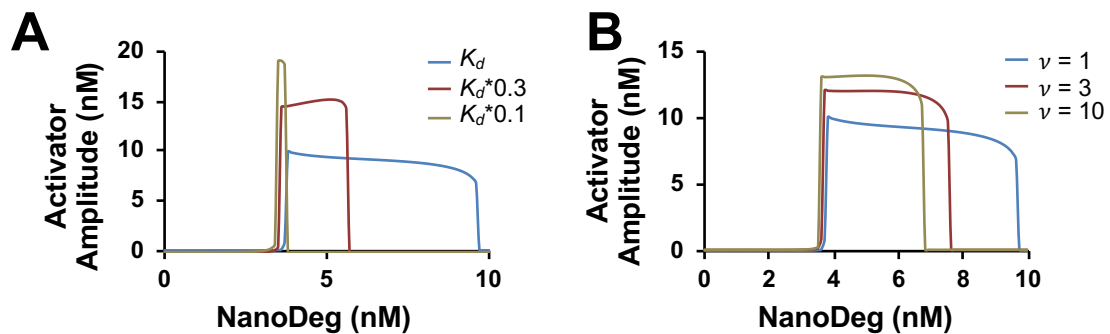


Figure 4.3 Effect of NanoDeg affinity and rate of interaction on oscillations. (A) Oscillation amplitude of the activator protein as a function of NanoDeg concentration for different K_d between the NanoDeg and the activator. (B) Oscillation amplitude of the activator protein as a function of NanoDeg

concentration for different rates of interaction (ν) between the NanoDeg and the activator. Reported amplitude was calculated as the difference between the largest and the lowest concentration of the reported protein in the region of oscillation.

Taken together, these results provide design rules for modulating oscillatory behavior of the activator-repressor using the NanoDeg. Specifically, the NanoDeg can be used to generate activator-repressor oscillators from activator-repressor pairs that do not oscillate due to a lack of timescale separation. The NanoDeg degradation rate needed to generate the required timescale separation is less stringent than the activator degradation rate required for oscillation when the NanoDeg and activator complex formation inhibits the activator binding to its cognate promoter. Furthermore, the oscillation amplitude is insensitive to variations in NanoDeg concentration and NanoDeg half-life within the oscillation-inducing limits. The period of oscillation, however, is sensitive to variations in the NanoDeg half-life which suggests a mechanism to modulate oscillation period independent of amplitude. Additionally, the rate of interaction between the NanoDeg and the activator and the activators affinity to the NanoDeg are important parameters to be considered for experimental design.

4.2.2. Goodwin oscillator

Goodwin oscillators are single-protein networks formed by a self-repressing protein with a delay in the maturation, or repressive effect, of the protein [108]. The length of the delay in the maturation process introduces a lag between the expression of the nascent protein and the repressing capacity of the mature protein

[98], [109], which triggers oscillations in the repressor concentration. Oscillation in the Goodwin topology can arise from a limit cycle around an unstable equilibrium or due to a very long transient (excitable) oscillation [88], [110] towards the stable equilibrium. Both behaviors are connected to the presence of a supercritical Hopf bifurcation associated with the repressor maturation delay [90], [91], with the limit cycle appearing if the maturation delay exceeds the critical value and with the excitability appearing if the maturation delay approaches the critical value.

Accordingly, when the lag associated with the maturation delay is sufficiently long, the gene may undergo bursts of expression of nascent protein followed by periods of strong repression from the matured proteins generated in the burst. This topology is exemplified in Figure 4.4A and modeled by a delay-differential equation describing the concentrations of a repressor in both nascent and mature forms and the NanoDeg derived as dependent on the rate of synthesis and the rate of degradation. The concentration of the mature protein is modeled by the use of the delay term τ . Interaction between the NanoDeg and the repressor is modeled by mass-action expression between the NanoDeg and the mature protein species. The repressor regulated rate of synthesis is modeled as a Hill function. This model is further detailed in the Methods section 4.4.2.

For the self-repressing gene simulated herein with a half-life (η_R) of 11 h, a delay (τ) of 0.5 h in the maturation is associated with a stable equilibrium. A delay $\tau = 10$ h also results in a stable equilibrium with a pronounced, transient oscillatory

response. For a delay $\tau = 15$ h, the simulated system exhibits an excitable response from a stable equilibrium that approximates a limit cycle orbit around an unstable equilibrium (Figure 4.4B). This result shows that the excitability of the Goodwin oscillator is achieved due to a large enough maturation delay relative to the half-life of the repressor, in accordance with previous results [111].

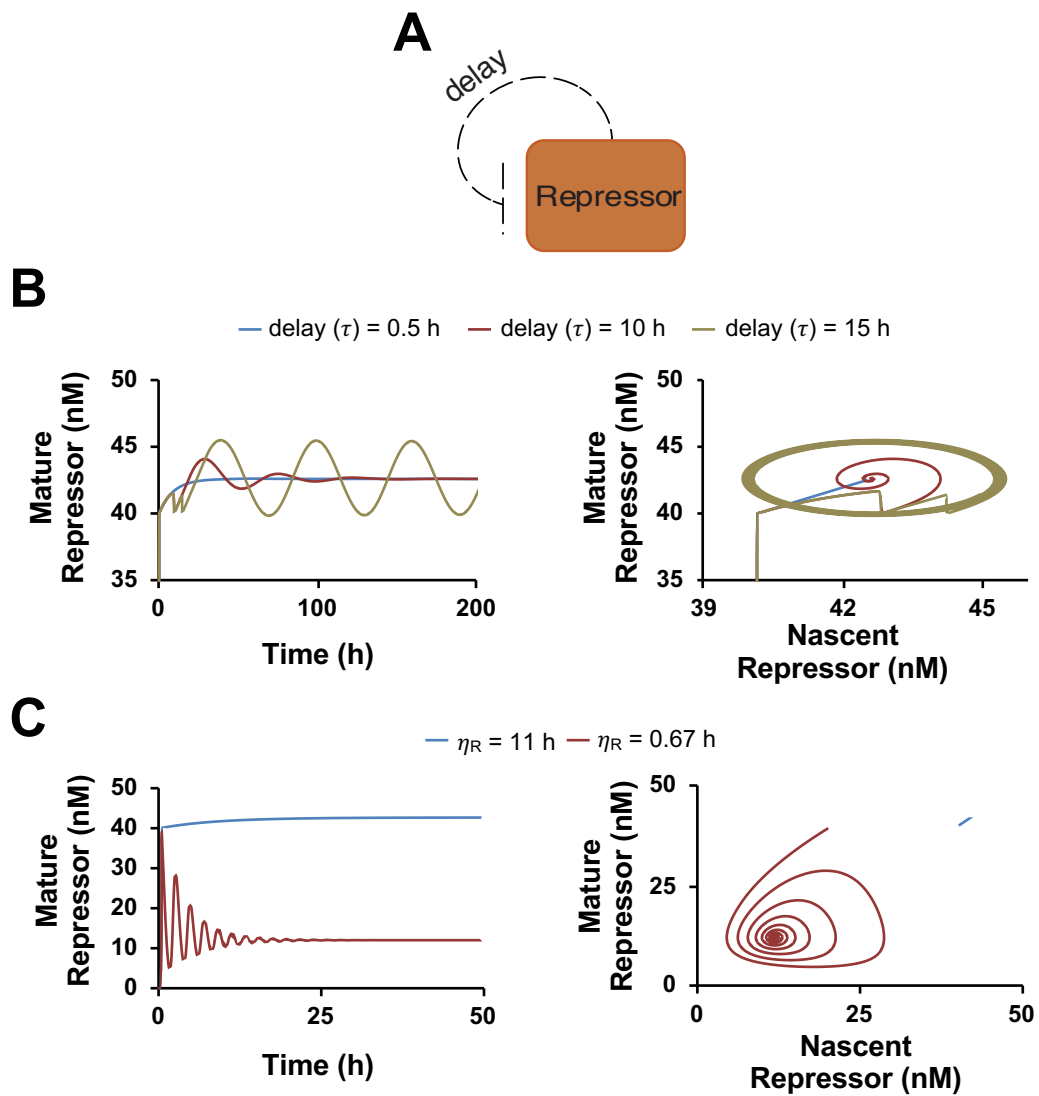


Figure 4.4 The Goodwin oscillator. (A) Schematic representation of a Goodwin oscillator topology. (B) Mature repressor protein levels of the Goodwin oscillator

topology as a function of time simulated for 200 h (left) and phase diagram of mature repressor levels as a function of nascent repressor levels (right) for a mature protein half-life (η_R) of 11 h and with 0.5 h, 10 h, or 15 h maturation delays (τ). (C) Mature repressor protein levels of the Goodwin oscillator topology as a function of time simulated for 50 h (left) and phase diagram of mature repressor levels as a function of nascent repressor levels (right) for $\tau = 0.5$ h for the nascent protein to mature and with a mature repressor protein half-life (η_R) of 11 h or 0.67 h. Reported amplitude was calculated as the difference between the largest and the lowest concentration of the reported protein in the region of oscillation.

To investigate the use of the NanoDeg to trigger oscillations in the Goodwin oscillator topology, I first simulated the effect of decreasing the half-life of the repressor and show that transient oscillations of the Goodwin topology can be triggered by decreasing the half-life of the repressor (Figure 4.4C). In fact, for a repressor with a maturation delay $\tau = 0.5$ h and half-life $\eta_R = 11$ h, the Goodwin topology does not present any oscillatory behavior. For the model utilized, I numerically found that the critical parameter for the Hopf bifurcation occurs at η_R approximately 0.65 h. For half-lives smaller than the critical value, the equilibrium is unstable and the simulated trajectories are unbounded. Setting the half-life $\eta_R = 0.67$ h, a value close to the critical parameter, results in an excitable dynamic (damped oscillation) of the repressor concentration (Figure 4.4C). Following this result, it was hypothesized that introducing a repressor-targeting NanoDeg to reduce the effective half-life of the repressor may trigger oscillations in a non-oscillating Goodwin topology (Figure 4.5A). A simulation with a maturation delay $\tau = 0.5$ h, repressor half-life $\eta_R = 11$ h, and a repressor-targeting NanoDeg half-life (η_N) of 0.9 h also produces an excitable response with transient oscillation and a lower repressor equilibrium concentration compared to the system lacking

NanoDeg expression (Figure 4.5B, 0 nM and 20 nM). Upon addition of a sufficiently large concentration of NanoDeg the Goodwin topology exhibits sustained oscillations (Figure 4.5B, 30 nM).

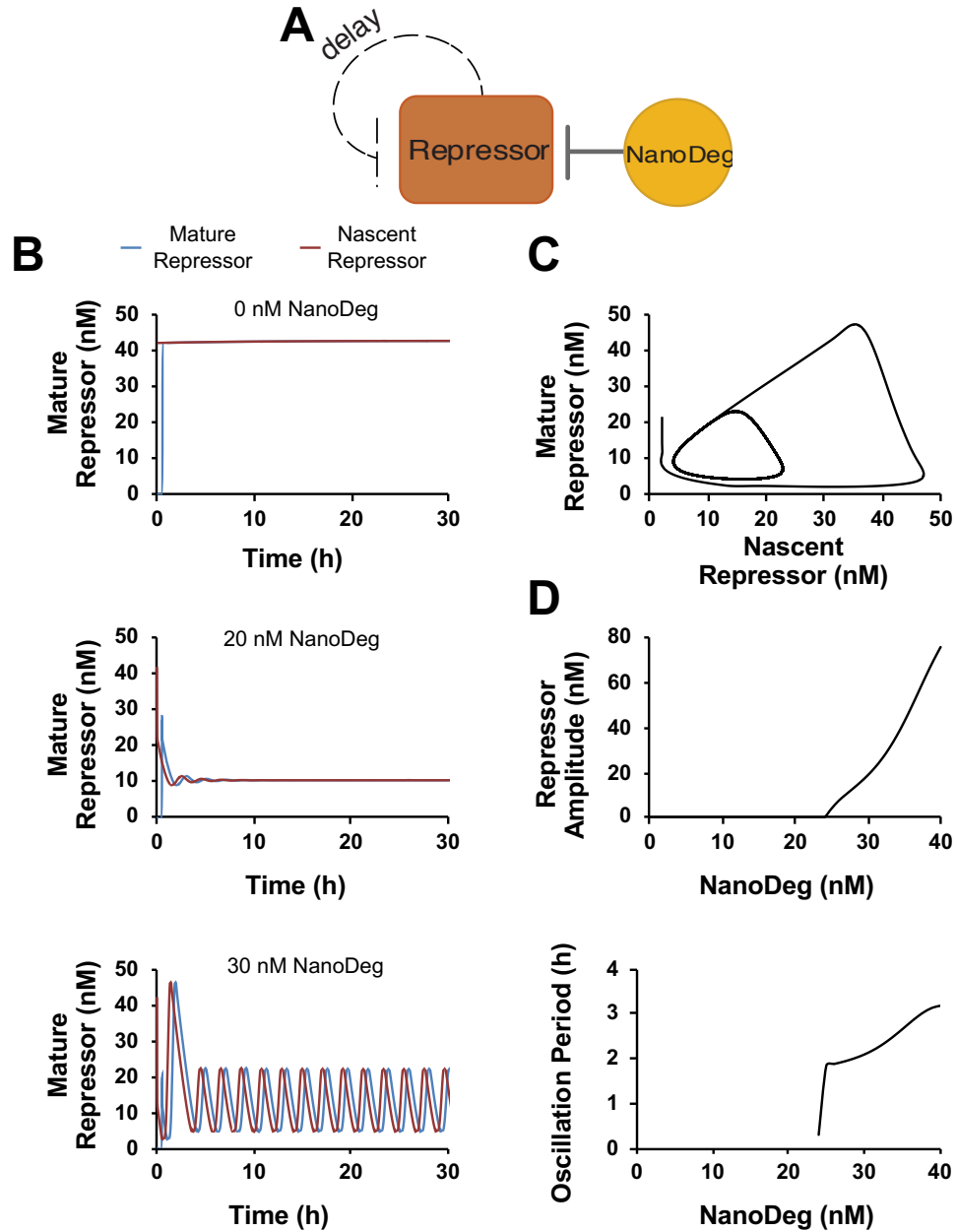


Figure 4.5 A NanoDeg modified Goodwin oscillator. (A) Schematic representation of a NanoDeg-tuned Goodwin oscillator topology. (B) Nascent and mature repressor

protein levels as a function of time for the Goodwin Oscillator topology simulated for 50 h and with 0 nM (left), 20 nM (center) or 30 nM (right) concentration of NanoDeg. (C) Phase diagram of mature repressor levels as a function of nascent repressor levels for the Goodwin oscillator with 30 nM NanoDeg. (D) Oscillation amplitude of the mature repressor (left) and oscillation period (right) of the Goodwin oscillator incorporating a NanoDeg as a function of NanoDeg concentration. Reported amplitude was calculated as the difference between the largest and the lowest concentration of the reported protein in the region of oscillation. The reported oscillation period was calculated as the zero crossings of the zero-mean trajectory in the region of oscillation.

The oscillations observed by the introduction of the NanoDeg are from a sustained limit cycle, indicating the effect of the NanoDeg on the repressor is analogous to increasing the maturation delay to exceed the critical Hopf bifurcation parameter (Figure 4.5C). For the system simulated, NanoDeg concentrations below 25 nM produce only transient oscillation. Above 25 nM NanoDeg, the amplitude and period of Goodwin oscillations triggered by NanoDeg expression increase linearly as the concentration of the NanoDeg increases until an upper bound is reached. Beyond this upper-bound NanoDeg-mediated degradation of the repressor dominates the capabilities of expression of the Repressor (Figure 4.5D).

These results demonstrate constitutive expression of the NanoDeg targeting a self-repressing protein can produce an oscillatory response based on the Goodwin topology. A NanoDeg effector in the Goodwin topology has potential to introduce additional delay between expression of the nascent repressor and its maturation to produce a robust oscillation. Furthermore, the amplitude and period of oscillation are sensitive to the concentration of the NanoDeg, suggesting a method to experimentally tune the amplitude and period of a Goodwin oscillator.

4.2.3. Repressilator regulation

Repressilators are genetic circuits that employ repressors connected in series to implement a ring oscillator. Genetic repressilators were initially constructed in *E. coli* [53]. Repressilator topologies were later identified in certain circadian clocks [112], [113] and the required conditions for oscillation in repressilators have been investigated in previous theoretical works [114]–[116].

In general, an odd number of repressor nodes connected in a ring will present oscillation provided that the expression of each repressor node is sufficiently regulated by the corresponding regulating repressor. Leaky expression from any repressor node can impair the oscillations of the system [116]. In the present section, I investigate the extent to which a NanoDeg can be employed to mitigate leakiness in a non-oscillating repressilator topology using a mathematical model based on ordinary differential equations describing the concentration of the species involved. All species concentration profiles were derived as dependent on the rate of synthesis regulated by a repressor following a Hill function and the rate of degradation. Interactions between the NanoDeg and its targets are modeled by mass-action expressions. The model is further detailed in the Methods section 4.4.3. Specifically, I investigate two alternative designs implementing the NanoDeg in a three-node repressilator topology to induce oscillations that are lacking as a result of the leaky expression of the three repressors.

One potential method to tune the repressilator via NanoDeg expression is through a single NanoDeg capable of degrading all three repressors (Figure 4.6A). This design could be implemented using a NanoDeg that recognizes a domain common to all three repressors, such as the KRAB domain or by fusing an epitope [104] recognized by the NanoDeg to the three repressors of a synthetic repressilator. I first modeled a repressilator topology that lacks expression of the NanoDeg and does not oscillate due to leaky expression of the repressors (Figure 4.6B, left). Oscillations in the repressilator are triggered by addition of a constitutively expressed NanoDeg that enhances degradation of all three repressors (Figure 4.6, right). Notably, because the three repressor nodes are simulated with identical parameters, the free concentration of the NanoDeg targeting the three nodes also presents an oscillatory behavior with three times the frequency of each of the repressors and displays a minimum when each node is at its maximum amplitude. In a repressilator system with non-identical repressor parameters, the NanoDeg still presents an oscillatory period with a frequency component that is three times the frequency of each of the repressors and an amplitude inversely proportional to the amplitude of the individual repressor being expressed (Figure 4.6C).

To investigate the effect of NanoDeg concentration on the period and amplitude of oscillation, I simulated the non-oscillating repressilator with increasing NanoDeg concentrations. Incorporating the NanoDeg at concentrations that do not produce sustained oscillations (Figure 4.6D, 5 nM and 10 nM) produces damped

oscillation. The addition of higher NanoDeg concentrations (Figure 4.6D, 20 nM) is sufficient to produce sustained oscillations of the repressilator (Figure 4.6D). This result suggests that it may be possible to tune the oscillation characteristics by varying the NanoDeg concentration in a repressilator with a common NanoDeg mediating degradation of all three repressors. I analyzed the oscillation amplitude and period for this repressilator topology simulated with a range of NanoDeg concentrations (Figure 4.6E). In the examples simulated, the total concentration of the NanoDeg that results in sustained oscillations is between 15 nM and 70 nM. The lower concentration bound exists as there is a minimum concentration of NanoDeg required to compensate for the leakiness of the repressilator nodes. The higher concentration bound exists as a very large concentration of NanoDeg will result in degradation surpassing the capacity of expression of at least one of the repressors (Figure 4.6E). In the region of NanoDeg concentration where oscillations occur, the amplitude increases substantially with increasing NanoDeg concentrations. In the simulation, the amplitude of repressor A ranges from 20 nM for a 15 nM concentration of NanoDeg to 92 nM for a 70 nM concentration of NanoDeg, which follows a curve with a slope greater than one. This result demonstrates the oscillation amplitude is sensitive to NanoDeg concentration in this repressilator with a common NanoDeg. This paradoxical result of amplitude increasing with increased NanoDeg-mediated degradation is due to the fact that as the amount of NanoDeg increases the leakiness of each of the nodes is effectively reduced.

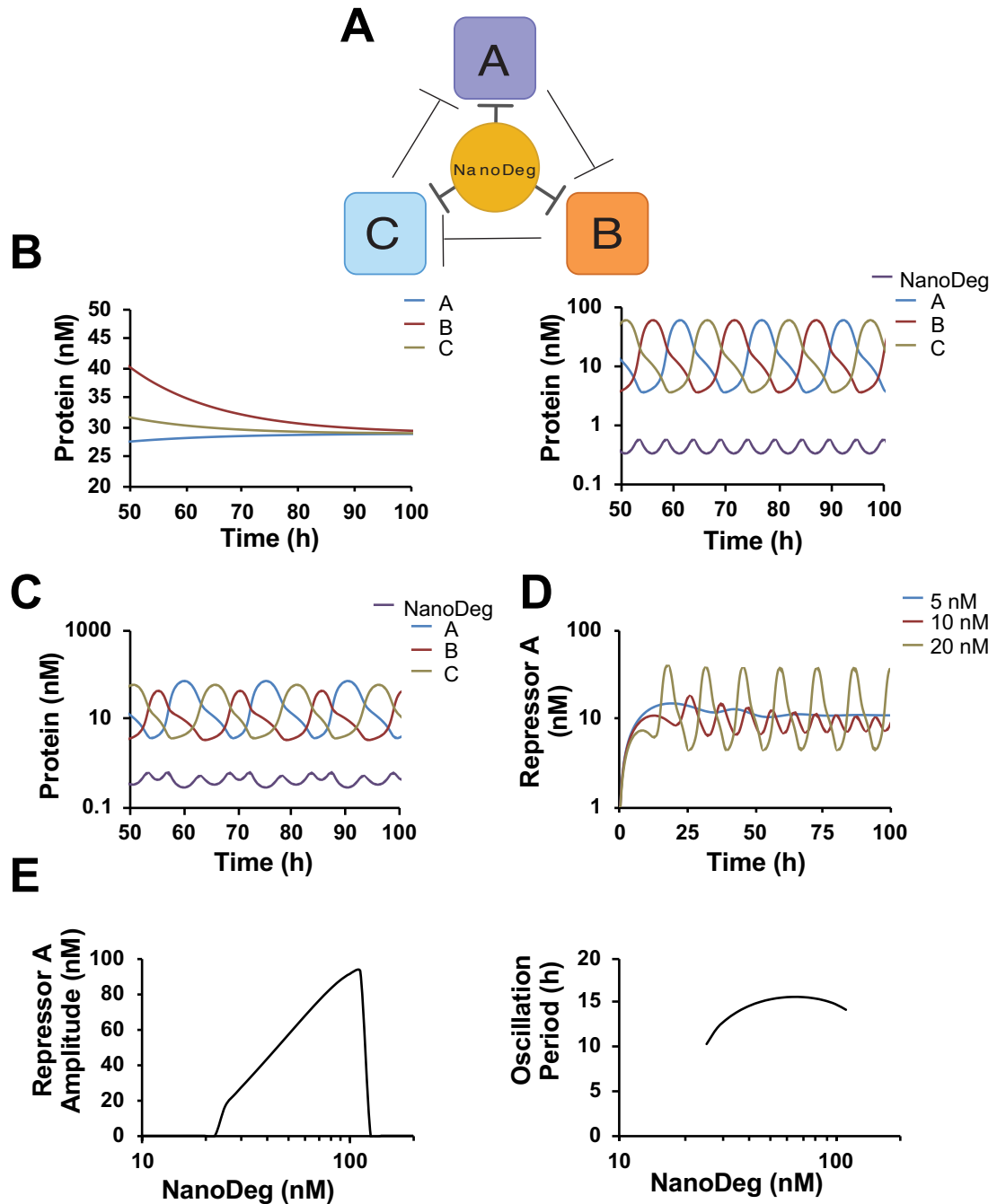


Figure 4.6 Repressilator tuning with a common NanoDeg. (A) Schematic representation of a repressilator incorporating a NanoDeg that targets all three repressors. (B) Protein levels for all topology components as a function of time for a repressilator lacking the NanoDeg (left) or incorporating the NanoDeg targeting all three repressors (right) simulated for 100 h. The three repressors of the repressilator have the same synthesis parameters (see methods). (C) Protein levels

for all topology components as a function of time for a repressilator incorporating the NanoDeg, and where each repressor has a different synthesis parameter but share a common degradation rate (see methods). Simulation covers 100 h. (D) Repressor A protein levels as a function of time for the repressilator incorporating the NanoDeg targeting all three repressors and where the repressors have the same synthesis parameters. Simulation covers 100 h and illustrates both insufficient (5 nM and 10 nM) or sufficient (20 nM) concentration of the NanoDeg to achieve sustained oscillations. (E) Oscillation amplitude of repressor A (left) and oscillation period (right) as a function of NanoDeg concentration for a repressilator incorporating the NanoDeg targeting all three repressors with the same synthesis parameters for all three repressors. Reported amplitude was calculated as the difference between the largest and the lowest concentration of the reported protein in the region of oscillation. The reported oscillation period was calculated as the zero crossings of the zero-mean trajectory in the region of oscillation.

The decreased leakiness results in an increased dynamic range of each node and, consequently, in a more pronounced oscillation. By contrast, the oscillation period does not vary substantially, ranging between 12 h and 16 h in a non-monotonic manner (Figure 4.6E).

I also investigated an alternative design to tune the non-oscillating repressilator with three NanoDeps mediating degradation of the three repressor nodes independently (Figure 4.7A). Similar to the use of a common NanoDeg, the use of independent NanoDeps will also result in triggering oscillations by mitigating the leakiness of the nodes in the repressilator; however, both amplitude and period are highly sensitive to the concentration of total NanoDeg (Figure 4.7B). When the concentration of each NanoDeg is less than 3nM, the amplitude increases substantially as a result of the NanoDeps decreasing the leaky concentration of the repressors and, consequently, increasing the dynamic range of each node. The amplitude of the oscillation decreases as a result of the enhanced degradation of the

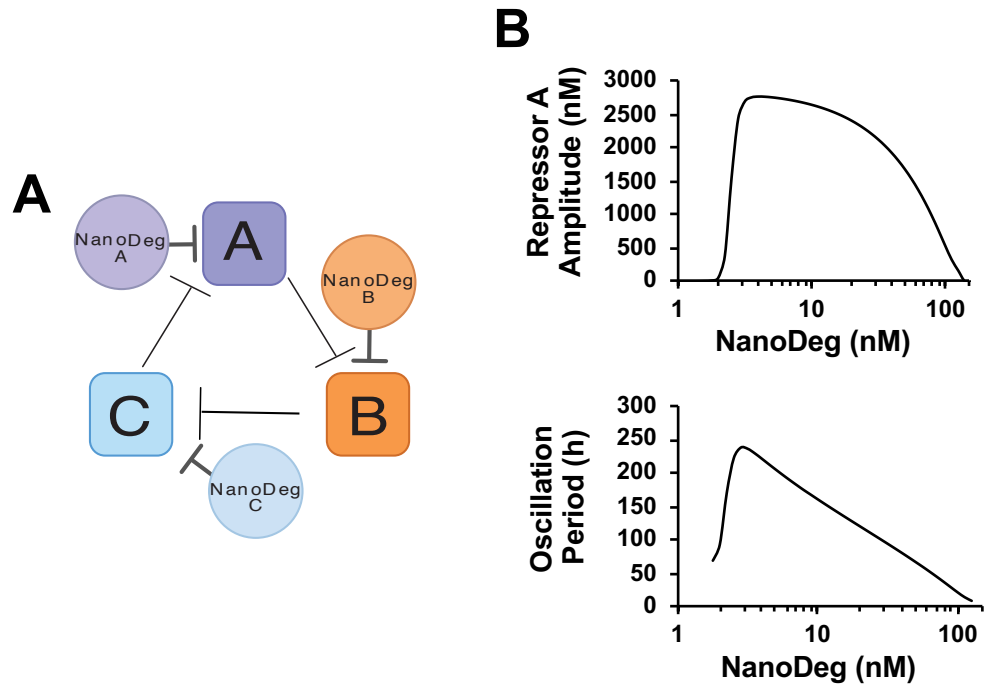


Figure 4.7 Repressilator tuning with individual NanoDeps. (A) Schematic representation of a repressilator incorporating separate NanoDeps that target each repressor independently. (B) Oscillation amplitude of repressor A (left) and oscillation period (right) as a function of NanoDeg concentration for a repressilator incorporating separate NanoDeps targeting each repressor independently with the same parameters for all three repressors and NanoDeps (see methods). Reported amplitude was calculated as the difference between the largest and the lowest concentration of the reported protein in the region of oscillation. The reported oscillation period was calculated as the zero crossings of the zero-mean trajectory in the region of oscillation.

repressors as the concentration of each NanoDeg increases above 3nM. The decreasing period of oscillations is due to the fact that the presence of the NanoDeps leads to an effective increase in the degradation rate of the repressors [95]. Contrasting the behavior of the period illustrated in Figure 4.7B with that illustrated in Figure 4.6E suggests the presence of a secondary coupling [117] between the

repressor nodes is provided by the integration of a common NanoDeg in the repressilator system.

These results show that the NanoDeg can be used in two different designs to tune repressilators with distinct results. In the first strategy, a common NanoDeg that targets the three proteins can be used to trigger oscillations. The use of a common NanoDeg provides a means to tune amplitude without a significant impact on the period of oscillation. In the second strategy, the use of multiple NanoDegs, each targeting a respective node of the repressor, can also be used to trigger oscillations. For repressilators adjusted using this second strategy, both the amplitude and period of oscillation are highly sensitive to the amount of NanoDeg in the system.

4.2.4. NanoDeg repressilator

In this section, I investigate employing the post-translational action of the NanoDeg [97] to generate a mixed-mode repressilator circuit from an existing transcription-based repressor-of-repressor network [118]–[121]. Specifically, I investigated the potential to design oscillating systems from topologies consisting of two repressors coupled with the expression and action of a NanoDeg. To this end, I modeled the effect of introducing a NanoDeg that targets a repressor-of-repressor (repressor A) and that is transcriptionally regulated by the repressed repressor (repressor B) (Figure 4.8A). Similar to the other repressilator topologies, this system was modeled based on ordinary differential equations describing the

concentration of the species involved. The concentration of the repressor A was modeled by constant synthesis and degradation rates. The concentration of the repressor B and the NanoDeg were derived as dependent on the rate of synthesis regulated by a repressor following a Hill function and rate of degradation.

Interaction between the NanoDeg and repressor A was modeled by mass-action expression. Further details of this model are provided in the Methods section 4.4.4.

The resulting topology is similar to that of a three-node repressilator, with the significant distinction that the interaction between the “third repressor,” the NanoDeg, and repressor A is post-translational rather than transcriptional. The addition of the NanoDeg with a half-life of 0.9 h such that its expression is regulated by a stable repressor B (half-life 11 h) and it sufficiently enhances the degradation of a stable repressor A (half-life 11 h) results in oscillatory behavior of the network (Figure 4.8B).

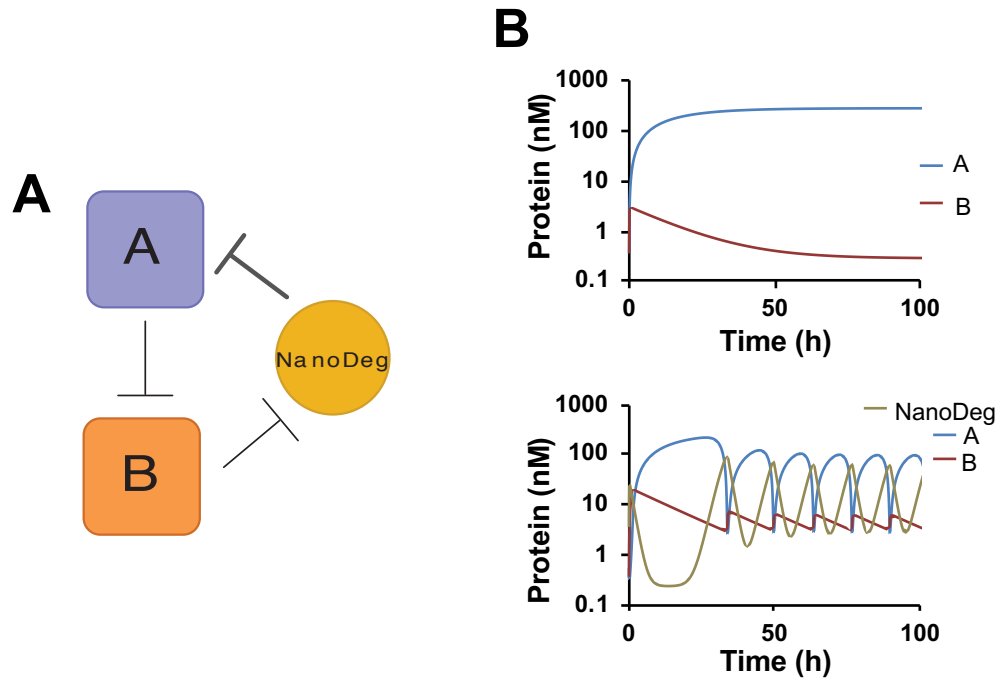


Figure 4.8 The NanoDeg Repressilator from a repressor-of-a-repressor network. **(A)** Schematic representation of a transcriptional repressor-of-repressor network incorporating the NanoDeg as separate node to make a repressilator. **(B)** Protein levels of a repressor-of-repressor network lacking the NanoDeg (top) or incorporating the NanoDeg as a network node (bottom) as a function of time simulated for 100 h.

To investigate design rules for employing the NanoDeg to generate a repressilator from a repressor-of-repressor network, I modeled the oscillatory characteristics as a function of the concentration of DNA encoding the NanoDeg, the NanoDeg half-life, and the sensitivity (Hill coefficients) of repressor A and repressor B. For the simulated system, that minimum concentration was approximately 2 nM of DNA. There is also a maximum concentration of NanoDeg encoding DNA that this modified repressilator can tolerate before the NanoDeg-mediated degradation overwhelms the potential for expression of repressor A and thus eliminates the

oscillatory behavior. In the simulated example, the maximum concentration was approximately 630 nM.

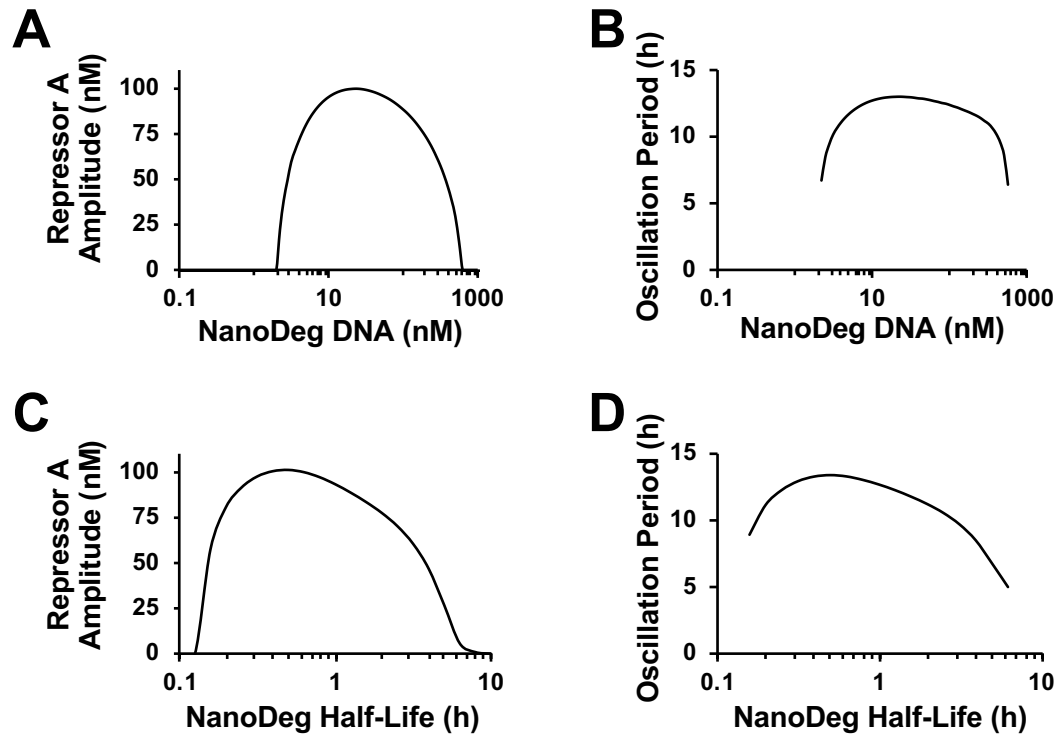


Figure 4.9 Tuning the NanoDeg Repressilator by NanoDeg concentration and half-life. (A) Oscillation amplitude of repressor A and (B) oscillation period as a function of NanoDeg encoding DNA concentration. (C) Oscillation amplitude of repressor A and (D) oscillation period as a function of NanoDeg half-life. Reported amplitude was calculated as the difference between the largest and the lowest concentration of the reported protein in the region of oscillation. The reported oscillation period was calculated as the zero crossings of the zero-mean trajectory in the region of oscillation.

The half-life of the NanoDeg also impacts the amplitude and the period of the repressilator. For repressors A and B exhibiting a half-life of 11h, a NanoDeg half-life between 0.5 h - 1 h provides the largest amplitude and oscillation period. Notably, as the half-life of the NanoDeg approaches that of the repressors, the oscillation

amplitude is reduced and the network transitions to a stable equilibrium dominated by expression of repressor A (Figure 4.9C and D).

In the simulations employed for this NanoDeg repressilator topology, the sensitivity of repressors [122] A and B was relatively large ($n=10$, $m=10$). It has been shown that repressilators formed by sensitive repressors, as modeled by the Hill coefficient, are more likely to present oscillation [115]. To investigate how the sensitivity of repressor A (Hill coefficient m) or repressor B (Hill coefficient n) impacts the presence of an oscillation, I modeled the NanoDeg repressilator with pairs of Hill coefficients (m, n) ranging between four and 10 (Figure 4.10A and B).

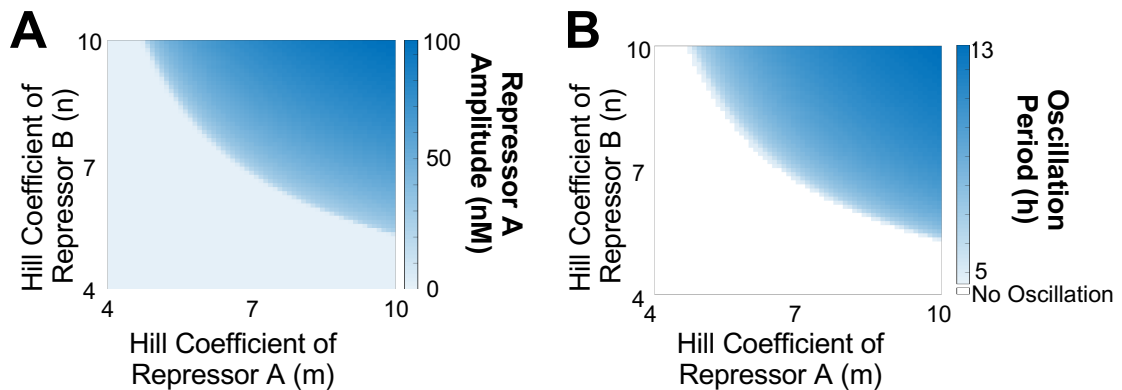


Figure 4.10 Effect of repressor sensitivity on oscillations of the NanoDeg repressilator. (A) Oscillation amplitude of repressor A and (B) oscillation period as a function of Hill Coefficients of Repressor A and Repressor B. Reported amplitude was calculated as the difference between the largest and the lowest concentration of the reported protein in the region of oscillation. The reported oscillation period was calculated as the zero crossings of the zero-mean trajectory in the region of oscillation.

Hill coefficient values $m < 4$ or $n < 4$ do not result in oscillatory behavior of this system as modeled here. Of note, it appears that the system presents oscillations for

the lower sensitivity of repressor A ($m > 4.8$ can present oscillation for $n = 10$) than of repressor B ($n > 5.4$ presents oscillations for $n = 10$).

These analyses demonstrate that the NanoDeg can be effectively used to implement repression feedback of an oscillator that is conventionally implemented using a transcriptional repressor. These analyses also show that such a strategy might be limited to investigate repressor-of-repressor pairs that present particularly high sensitivities, such as those that display switch-like dynamics due to post-translational modifications [122]–[124].

4.3. Discussion

The study of oscillatory behavior in biological systems is commonly performed by fabricating synthetic circuits [53], [54], [109], [125], [126], or by modifications to existing biological systems [83], [113], [127]–[129]. Studies employing synthetic circuits are of great value to investigate the nature of oscillatory behavior in biomolecular systems. However, reconstruction of the entire network to study the interaction between the oscillatory behavior of the biochemical system and its phenotypic response is remarkably challenging. Therefore, there is a need for biological tools that can probe and perturb existing biochemical systems.

Studies that rely on modifications of an existing network depend on either the use of existing protein-specific inhibitors or the genetic engineering of network

component proteins. As an example, the study by Purvis et al [83] relied on the use of a small molecule that specifically inhibits the Mdm2 protein, a repressor in the p53 network. Similarly, Dale et al [129] employed molecules that specifically inhibit the cleavage of notch protein, a step in the notch oscillations described therein. These strategies are valuable, but their application is contingent on the knowledge and existence of such molecules. Other studies employ gene modification by employing knockouts [113] or mutants [128] to investigate biochemical oscillators. Such studies rely on the viability of the target organism after undergoing deletion or mutation of the target protein. Moreover, these types of studies do not allow for quantitative control of the alterations to the target protein.

There are few studies that focus on the use of protein regulation methods beyond genetic modifications in biomolecular oscillators. Tigges et al. used siRNA was used to tune a synthetic circuit that implements a relaxed feedback oscillator [130]. A potential approach for post-translational regulation of existing biochemical oscillators using DNA binding sequences targeted by transcriptional regulators in the oscillator have been theoretically considered as well [94], [131]. The effect of such modifications, however, is limited to sequestration [107] of the target protein or to timescale impacts due to retroactivity [105], [132].

In the present study, I investigated the potential for post-translational interactions as a manner to trigger oscillations in biomolecular networks that have a topology capable of oscillating [94] but do not present oscillation. The post-

translational interaction may perform multiple distinct roles in the systems described. In the activator-repressor subsection and the Goodwin oscillator subsection, I show that the NanoDeg can be used to increase the degradation rate of a node in the cell to trigger timescale separations required for oscillations. In the Goodwin oscillator subsection and the repressilator regulation subsection, I show that the NanoDeg can trigger oscillations by mitigating leaky expression that prevents oscillatory behavior. In the NanoDeg repressilator subsection, I show that the NanoDeg can be used as a negative feedback loop that plays a role similar to that of a transcriptional repressor in the network. Taken together these results show that the NanoDeg platform is a universal tool for protein perturbation that can be employed to generate or modify biomolecular oscillators without the need for engineering a target protein.

4.4. Methods

All the models presented in this work were computationally simulated using MATLAB R2019a, The Mathworks. Models presented in the activator-repressor section and the two repressilator sections were simulated employing the continuous ordinary differential equation (ODE) solver “ode23s,” an order (2, 3) solver modified to work with stiff systems. Models presented in the Goodwin oscillator section were simulated using a DDE solver “dde23,” an order (2, 3) solver. To calculate the amplitude of the reported oscillations, I used MATLAB’s “range” function to calculate the difference between the largest and the lowest

concentration of the reported protein in the region of oscillation. To calculate the period of the reported oscillations, I subtract the simulated trajectory for the concentration of a reported protein by the mean value of concentration in the region of oscillation, to obtain a zero-mean trajectory. Subsequently, I identify the zero crossings of the zero-mean trajectory to calculate the periods in the region of oscillation and report the mean period. For all simulations, I impose a simulation sampling period of 0.01 hour, to prevent potential errors in the calculation of periods and amplitudes from low sampling.

General Assumptions

In this work, I made certain assumptions about the dynamics and behavior of transcriptional regulators (i.e., repressors or activators) and the NanoDeg. I assumed that the transcriptional regulators bound to the NanoDeg are blocked from interaction with the respective promoters and that at most one NanoDeg molecule couples to a target protein. I also make the simplifying assumption that the NanoDeg-target complex is degraded at the same rate as the free NanoDeg.

4.4.1. Activator Repressor simulations

For the activator-repressor system, the differential equations used in the simulation are given in the equations below.

Equation 4.4.1 Activator-repressor with an activator-targetting NanoDeg.

$$\frac{dA}{dt} = p_{AT} \frac{(\alpha_1 A^m + \alpha_2 K_A^m)(\beta_1 B^n + \beta_2 K_B^n)}{(A^m + K_A^m)(B^n + K_B^n)} - \delta_A A - k_{on} AN + k_{off} C,$$

$$\frac{dB}{dt} = p_{BT} \frac{k_5 A^m + k_6 k_A^m}{A^m + k_A^m} - \delta_B B,$$

$$\frac{dN}{dt} = p_{NT} k_n - \delta_N N - k_{on} AN + k_{off} C,$$

$$\frac{dC}{dt} = k_{on} AN - k_{off} C - \delta_N C.$$

In this system, A represents the concentration of the unbound activator, B represents the concentration of the repressor, N represents the concentration of unbound NanoDeg, and C represents the concentration of the complex formed by the association of the NanoDeg with the activator. Regulation of the expression of the activator from the hybrid promoter by the activator and repressor are assumed to be independent. Hence, the system can be simulated using a multiplicative model that combines the Hill function of self-activation by A with the Hill function of repression by B. Expression of the repressor is simulated using a Hill function of the activation by A. Constitutive expression of NanoDeg is simulated using a constant expression rate. Half-lives of the proteins are simulated by a linear degradation coefficient. Association and dissociation interactions between the activator and the NanoDeg are modeled using a mass-action reaction model. A description of all

model variables and parameter values used for simulation (unless otherwise specified in the figures) are given in the table below (Table 4.4.1).

Parameter	Description	Value	Source
p_{A_T}	Concentration of DNA containing the activator gene.	1 nM	This paper. Represents approximately 2200 copies of gene/cell[133] for a typical cell of volume[134] $3.7\mu\text{m}^3$.
p_{B_T}	Concentration of DNA containing the repressor gene.	1 nM	This paper.
p_{N_T}	Concentration of DNA containing the NanoDeg gene.	1 nM	This paper.
K_A	Dissociation constant between activator and promoter operator sites.	3 nM	[37]
K_B	Dissociation constant between repressor and promoter operator sites.	3 nM	[37]
$\eta_A = \delta_A^{-1} \ln(2)$	Half-life of activator	4 h	This paper.
$\eta_B = \delta_B^{-1} \ln(2)$	Half-life of repressor	4 h	This paper.
$\eta_N = \delta_N^{-1} \ln(2)$	Half-life of NanoDeg	0.9 h	[37]
α_1	Parameter for the hybrid promoter that regulates the activator. Associated with maximal expression for self-activation.	112.5 h^{-1}	[70]
α_2	Parameter for the hybrid promoter that regulates the activator. Associated with leaky expression for self-activation.	1 h^{-1}	Modified from [70]
β_1	Parameter for the hybrid promoter that regulates the activator. Associated with minimum expression due to repression.	0.04 h^{-1}	Modified from [70]

β_2	Parameter for the hybrid promoter that regulates the activator. Associated with leaky expression from the repressor.	1.8 h^{-1}	[70]
m	Cooperativity (i.e., Hill coefficient) for activator.	2	This paper.
n	Cooperativity (i.e., Hill coefficient) for repressor.	2	This paper.
k_5	Maximal expression of the repressor promoter.	36 h^{-1}	[70]
k_6	Leaky expression from the repressor promoter.	0.05 h^{-1}	Modified from [70]
k_{on}	Association rate between NanoDeg and activator.	$0.6262 \text{ (nM h)}^{-1}$	[37]
k_{off}	Dissociation rate of the NanoDeg-activator complex.	2.7648 h^{-1}	[37]
k_N	Expression rate from constitutive NanoDeg promoter.	5 nM/h	This paper. For the NanoDeg with 0.9 h half-life, the total NanoDeg concentration is approximately 6.5 nM.

Table 4.4.1 Parameters used in activator-repressor simulations.

Simulations of the activator-repressor system without NanoDeg were performed by setting $k_N = 0$, and simulations with a nominal concentration of NanoDeg were performed by setting $k_N = N_0/\delta_N$, in which N_0 is the nominal concentration of NanoDeg. To simulate the rate of the association and dissociation interaction (Figure 4.3B), the association and dissociation rates were both multiplied by a common multiplier v .

4.4.2. Goodwin Oscillator simulations

The systems illustrated in the Goodwin oscillator section were implemented using delay-differential equations (DDE) that model a fixed time delay for maturation of the repressor protein. That is, in this model I assume that the nascent repressor does not interact with the target promoter sequence or the NanoDeg. The resulting DDE system is given as:

Equation 4.4.2 Goodwin oscillator with a mature repressor-targetting NanoDeg.

$$\frac{dA}{dt} = p_{A_T} \frac{\beta_1 A_\tau^m + \beta_2 K_A^m}{A_\tau^m + K_A^m} - \delta_A A - k_{on} A_\tau N + k_{off} C$$

$$\frac{dN}{dt} = p_{N_T} k_N - \delta_N N - k_{on} A_\tau N + k_{off} C$$

$$\frac{dC}{dt} = k_{on} A_\tau N - k_{off} C - \delta_N C$$

In this system, $A = A(t)$ represents the free nascent repressor and $A_\tau = A(t - \tau)$ represents the mature repressor. The maturation delay is given by τ . N represents the free NanoDeg and C represents the complex formed by NanoDeg bound to the mature repressor A_τ . The initial history for the repressor is set to $A = 0$ for $-\tau \leq t \leq 0$. Expression of the repressor is simulated using a Hill function for repression by matured A_τ . Constitutive expression of NanoDeg is simulated using a constant expression rate. Half-lives of the proteins are simulated by a linear degradation coefficient. Association and dissociation interactions between the mature repressor A_τ and the NanoDeg is modeled using a mass-action reaction model. A description of

individual model variables and parameter values used for simulation (unless otherwise specified in the figures) are given in the table below (Table 4.4.2).

Parameter	Description	Value	Source
p_{AT}	Concentration of DNA containing the repressor gene.	1 nM	This paper. Represents approximately 2200 copies of gene/cell[133] for a typical cell of volume[134] $3.7\mu\text{m}^3$.
p_{NT}	Concentration of DNA containing the NanoDeg gene.	1 nM	This paper.
K_A	Dissociation constant between repressor and promoter operator sites.	3nM	[70]
$\eta_A = \delta_A^{-1} \ln(2)$	Half-life of repressor	11 h	This paper.
$\eta_N = \delta_N^{-1} \ln(2)$	Half-life of NanoDeg	0.9 h	[37]
β_1	Leaky expression rate of the repressor promoter.	1.8 h^{-1}	[70]
β_2	Maximum expression rate from the repressor promoter.	181 h^{-1}	[70]
m	Cooperativity (i.e., Hill coefficient) of the repressor.	2	This paper.
k_{on}	Association rate between NanoDeg and repressor.	$0.6262 \text{ (nM h)}^{-1}$	[37]
k_{off}	Dissociation rate for the NanoDeg-repressor complex.	2.7648 h^{-1}	[37]
k_N	Expression rate from constitutive NanoDeg promoter.	5 nM/h	This paper. For the NanoDeg with 0.9 h half-life, the total NanoDeg concentration is

			approximately 6.5nM.
τ	Repressor maturation time.	0.5 h.	This paper.

Table 4.4.2 Parameters used in Goodwin oscillator simulations.

Simulations of the Goodwin oscillator system without NanoDeg were performed by setting $k_N = 0$, and simulations with a nominal concentration of NanoDeg were performed by setting $k_N = N_0/\delta_N$, in which N_0 is the nominal concentration of NanoDeg.

4.4.3. Repressilator Regulation simulations

For the repressilator system tuned by a common NanoDeg, the differential equations used in the simulation are given in the equations below.

Equation 4.4.3 Repressilator with a common NanoDeg.

$$\frac{dA}{dt} = p_{A_T} \frac{k_1 C^r + k_2 K_C^r}{C^r + K_C^r} - \delta_A A - k_{on} AN + k_{off} T_A$$

$$\frac{dB}{dt} = p_{B_T} \frac{k_3 A^m + k_4 K_A^m}{A^m + K_A^m} - \delta_B B - k_{on} BN + k_{off} T_B$$

$$\frac{dC}{dt} = p_{C_T} \frac{k_5 B^n + k_6 K_B^n}{B^n + K_B^n} - \delta_C C - k_{on} CN + k_{off} T_C$$

$$\frac{dN}{dt} = p_{N_T} k_N - \delta_N N - k_{on} (A + B + C) N + k_{off} (T_A + T_B + T_C)$$

$$\frac{dT_A}{dt} = k_{on} AN + k_{off} T_A - \delta_N T_A$$

$$\frac{dT_B}{dt} = k_{on} BN + k_{off} T_B - \delta_N T_B$$

$$\frac{dT_C}{dt} = k_{on}CN + k_{off}T_C - \delta_N T_C$$

In this system, A, B and, C represent the concentration of three unbound repressors connected in series forming the repressilator and N represents the concentration of unbound NanoDeg. T_A , T_B , and T_C represents the concentration of the complex formed by the association of the NanoDeg with repressors A, B, and C, respectively. Expression of each repressor is simulated using a Hill function for repression by the corresponding repressor protein. Constitutive expression of NanoDeg is simulated using a constant expression rate. Half-lives of the proteins are simulated by a linear degradation coefficient. Association and dissociation interactions between the repressors and NanoDeg are modeled using a mass-action reaction model. A description of individual model variables and parameter values used for simulation (unless otherwise specified in the figures) are given in the table below (Table 4.4.3).

Parameter	Description	Value	Source
p_{A_T}	Concentration of DNA containing the gene for repressor A.	1 nM	This paper. Represents approximately 2200 copies of gene/cell[133] for a typical cell of volume[134] $3.7\mu\text{m}^3$.
p_{B_T}	Concentration of DNA containing the gene for repressor B.	1 nM	This paper.

p_{C_T}	Concentration of DNA containing the gene for repressor C.	1 nM	This paper.
p_{N_T}	Concentration of DNA encoding the NanoDeg.	1 nM	This paper.
K_A	Dissociation constant between repressor A and corresponding promoter operator sites.	3 nM	[70]
K_B	Dissociation constant between repressor B and corresponding promoter operator sites.	3 nM	[70]
K_C	Dissociation constant between repressor C and corresponding promoter operator sites.	3 nM	[70]
$\eta_A = \delta_A^{-1} \ln(2)$	Half-life of repressor A	11 h	This paper.
$\eta_B = \delta_B^{-1} \ln(2)$	Half-life of repressor B	11 h	This paper.
$\eta_C = \delta_C^{-1} \ln(2)$	Half-life of repressor C	11 h	This paper.
$\eta_N = \delta_N^{-1} \ln(2)$	Half-life of NanoDeg	0.9 h	[37]
k_1	Leaky expression rate of the repressor A promoter.	1.8 h^{-1}	[70]
k_2	Maximum expression rate of the repressor A promoter.	181 h^{-1}	[70]
k_3	Leaky expression rate of the repressor B promoter.	1.8 h^{-1}	[70]
k_4	Maximum expression rate of the repressor B promoter.	181 h^{-1}	[70]
k_5	Leaky expression rate of the repressor C promoter.	1.8 h^{-1}	[70]
k_6	Maximum expression rate of the repressor C promoter.	181 h^{-1}	[70]
m	Cooperativity (i.e., Hill coefficient) for repressor A.	4	This paper.

n	Cooperativity (i.e., Hill coefficient) for repressor B.	4	This paper.
r	Cooperativity (i.e., Hill coefficient) for repressor C.	4	This paper.
k_{on}	Association rate between NanoDeg and repressor.	0.6262 (nM h) ⁻¹	[37]
k_{off}	Dissociation rate of the NanoDeg-repressor complex.	2.7648 h ⁻¹	[37]
k_N	Expression rate from constitutive NanoDeg promoter.	5 nM/h	This paper. For the NanoDeg with 0.9 h half-life, the total NanoDeg concentration is approximately 6.5nM.

Table 4.4.3 Parameters used in repressilator with a common NanoDeg simulations.

Simulations of the repressilator system without NanoDeg were performed by setting $k_N = 0$, and simulations with a nominal concentration of NanoDeg were performed by setting $k_N = N_0/\delta_N$, in which N_0 is the nominal concentration of NanoDeg.

For the repressilator system tuned by independent NanoDeg N_A , N_B , and N_C , that target, respectively, repressors A, B, and C, the differential equations used in the simulation are given in the equations below:

Equation 4.4.4 Repressilator with individual NanoDegs.

$$\frac{dA}{dt} = p_{AT} \frac{k_1 C^r + k_2 K_C^r}{C^r + K_C^r} - \delta_A A - k_{on} A N_A + k_{off} T_A$$

$$\frac{dB}{dt} = p_{BT} \frac{k_3 A^m + k_4 K_A^m}{A^m + K_A^m} - \delta_B B - k_{on} B N_B + k_{off} T_B$$

$$\frac{dC}{dt} = p_{CT} \frac{k_5 B^n + k_6 K_B^n}{B^n + K_B^n} - \delta_C C - k_{on} C N_C + k_{off} T_C$$

$$\frac{dN_A}{dt} = p_{NTA} k_{NA} - \delta_{NA} N_A - k_{on} A N_A + k_{off} T_A$$

$$\frac{dN_B}{dt} = p_{NTB} k_{NB} - \delta_{NB} N_B - k_{on} A N_B + k_{off} T_B$$

$$\frac{dN_C}{dt} = p_{NTC} k_{NC} - \delta_{NC} N_C - k_{on} A N_C + k_{off} T_C$$

$$\frac{dT_A}{dt} = k_{on} A N_A + k_{off} T_A - \delta_{NA} T_A$$

$$\frac{dT_B}{dt} = k_{on} B N_B + k_{off} T_B - \delta_{NB} T_B$$

$$\frac{dT_C}{dt} = k_{on} C N_C + k_{off} T_C - \delta_{NC} T_C$$

In this system, A, B and, C represent the concentration of three unbound repressors connected in series forming the repressilator. N_A , N_B , and N_C represent the concentration of unbound NanoDeg molecules that target A, B, and C, respectively. T_A , T_B , and T_C represents the concentration of the complex formed by the association of N_A , N_B , and N_C with their respective repressors A, B, and C. In this system, the parameters were chosen such that each node of the repressilator is subject to the same dynamics. Expression of each repressor is simulated using a Hill function for repression by the corresponding repressor protein. Constitutive expression of N_A , N_B , and N_C are simulated using a constant rate. Half-lives of the proteins are simulated by a linear degradation coefficient. Association and

dissociation of the repressors and the corresponding NanoDeg are modeled using a mass-action reaction model. A description of all model variables and parameter values used for simulation (unless otherwise specified in the figures) are given in the table below (Table 4.4.4).

Parameter	Description	Value	Source
p_{A_T}	Concentration of DNA containing the gene for repressor A.	1 nM	This paper. Represents approximately 2200 copies of gene/cell[133] for a typical cell of volume[134] $3.7\mu\text{m}^3$.
p_{B_T}	Concentration of DNA containing the gene for repressor B.	1 nM	This paper.
p_{C_T}	Concentration of DNA containing the gene for repressor C.	1 nM	This paper.
$p_{N_{TA}}$	Concentration of DNA encoding the NanoDeg _A .	1 nM	This paper.
$p_{N_{TB}}$	Concentration of DNA encoding the NanoDeg _B .	1 nM	This paper.
$p_{N_{TC}}$	Concentration of DNA encoding the NanoDeg _C .	1 nM	This paper.
K_A	Dissociation constant between repressor A and corresponding promoter operator sites.	3 nM	[70]
K_B	Dissociation constant between repressor B and corresponding promoter operator sites.	3nM	[70]
K_B	Dissociation constant between repressor C and corresponding promoter operator sites.	3nM	[70]

$\eta_A = \delta_A^{-1} \ln(2)$	Half-life of repressor A	11 h	This paper.
$\eta_B = \delta_B^{-1} \ln(2)$	Half-life of repressor B	11 h	This paper.
$\eta_C = \delta_C^{-1} \ln(2)$	Half-life of repressor C	11 h	This paper.
$\eta_N = \delta_N^{-1} \ln(2)$	Half-life of the NanoDegs	0.9 h	[37]
k_1	Leaky expression rate of the repressor A promoter.	1.8 h^{-1}	[70]
k_2	Maximum expression rate of the repressor A promoter.	181 h^{-1}	[70]
k_3	Leaky expression rate of the repressor B promoter.	1.8 h^{-1}	[70]
k_4	Maximum expression rate of the repressor B promoter.	181 h^{-1}	[70]
k_5	Leaky expression rate of the repressor C promoter.	1.8 h^{-1}	[70]
k_6	Maximum expression of the repressor C promoter.	181 h^{-1}	[70]
m	Cooperativity (i.e., Hill coefficient) for repressor A.	4	This paper.
n	Cooperativity (i.e., Hill coefficient) for repressor B.	4	This paper.
r	Cooperativity (i.e., Hill coefficient) for repressor C.	4	This paper.
k_{on}	Association rate between NanoDegs and repressors.	$0.6262 \text{ (nM h)}^{-1}$	[37]
k_{off}	Dissociation rate of the NanoDeg-repressor complexes.	2.7648 h^{-1}	[37]
k_{NA}	Expression rate from constitutive NanoDeg _A promoter.	5 nM/h	This paper. For the NanoDeg with 0.9 h half-life, the total NanoDeg concentration is approximately 6.5nM.

k_{NB}	Expression rate from constitutive NanoDeg _B promoter.	5 nM/h	This paper.
k_{NC}	Expression rate from constitutive NanoDeg _C promoter.	5 nM/h	This paper.

Table 4.4.4 Parameters used in Repressilator with individual NanoDegs simulations.

Simulations of the repressilator without any NanoDeg were performed by setting $k_{NA} = k_{NB} = k_{NC} = 0$. The simulations with a nominal concentration of NanoDeg were performed using a common concentration $N_A = N_B = N_C = N_0$, by setting $k_{NA} = k_{NB} = k_{NC} = N_0/\delta_N$.

4.4.4. NanoDeg repressilator simulations

For the section describing the repressilator that incorporates a NanoDeg as a node in the ring oscillator, the differential equations used in the simulation are given in the equations below.

Equation 4.4.5 NanoDeg repressilator.

$$\frac{dA}{dt} = p_{AT}k_1 - \delta_A A - k_{on}AN + k_{off}C$$

$$\frac{dB}{dt} = p_{BT} \frac{k_2 A^m + k_3 K_A^m}{A^m + K_A^m} - \delta_B B$$

$$\frac{dN}{dt} = p_{NT} \frac{k_4 B^n + k_5 K_B^n}{B^n + K_B^n} - \delta_N N - k_{on}AN + k_{off}C$$

$$\frac{dC}{dt} = k_{on}AN - k_{off}C - \delta_N C$$

In this system, A represents the unbound concentration of a first repressor and B represents the concentration of a second repressor whose expression is regulated by B. In turn, B represses the expression of a NanoDeg that targets the first repressor. N represents the concentration of unbound NanoDeg and C represents the concentration of the complex formed by the association of the NanoDeg with the repressor A. Constitutive expression of repressor A is modeled by a constant expression rate. Expression of the repressor B and of the NanoDeg are simulated using a Hill function of repression by the repressors A and B, respectively. Half-lives of all the proteins are simulated by a linear degradation coefficient. Association and dissociation interactions between repressor A and the NanoDeg are modeled using a mass-action reaction model. A description of individual model variables and parameter values used for simulation (unless otherwise specified in the figures) are given in the table below (Table 4.4.5).

Parameter	Description	Value	Source
p_{A_T}	Concentration of DNA containing the gene for repressor A.	1 nM	This paper. Represents approximately 2200 copies of gene/cell[133] for a typical cell of volume[134] $3.7\mu\text{m}^3$.
p_{B_T}	Concentration of DNA containing the gene for repressor B.	1 nM	This paper.
p_{N_T}	Concentration of DNA encoding the NanoDeg.	1 nM	This paper.

K_A	Dissociation constant between repressor A and corresponding promoter operator sites.	3 nM	[70]
K_B	Dissociation constant between repressor B and corresponding promoter operator sites.	3 nM	[70]
$\eta_A = \delta_A^{-1} \ln(2)$	Half-life of repressor A	11 h	This paper.
$\eta_B = \delta_B^{-1} \ln(2)$	Half-life of repressor B	11 h	This paper.
$\eta_N = \delta_N^{-1} \ln(2)$	Half-life of NanoDeg	0.9 h	[37]
k_1	Constitutive expression rate of A	18.1 h ⁻¹	This paper.
k_2	Leaky expression rate of the repressor B promoter.	0.018 h ⁻¹	Modified from [70].
k_3	Maximum expression rate of the repressor B promoter.	18.1 h ⁻¹	Modified from [70].
k_4	Leaky expression rate of the NanoDeg promoter.	0.018 h ⁻¹	Modified from [70]
k_5	Maximum expression rate of the NanoDeg promoter.	18.1 h ⁻¹	Modified from [70]
m	Cooperativity (i.e., Hill coefficient) for repressor A.	10	This paper.
n	Cooperativity (i.e., Hill coefficient) for repressor B.	10	This paper.
k_{on}	Association rate between NanoDeg and repressor.	0.6262 (nM h) ⁻¹	[37].
k_{off}	Dissociation rate of the NanoDeg-repressor complex.	2.7648 h ⁻¹	[37].

Table 4.4.5 Parameters used in NanoDeg repressilator simulations.

Simulations for this system in the absence of NanoDeg were performed by setting $p_{NT} = 0$.

A platform for post-translational spatiotemporal control of cytosolic proteins

5.1. Introduction

Cellular information processing is primarily managed by regulating protein concentration in space and time [1], [135]. Temporal regulation of protein concentration is mostly achieved through transcription factor activation and degradation, which are controlled through a myriad of well-studied mechanisms [136]–[145]. Proteins are typically synthesized in the cytosol or on ER-bound ribosomes and then directed to the appropriate subcellular location through amino-acid sequences intrinsic to the proteins [146]. Protein function depends on subcellular location and can be drastically affected by environmental conditions,

such as pH and redox state [147]–[150]. Protein localization also dictates the availability of interacting proteins [151]–[153] and substrates [154]–[156], further diversifying protein functionality. Additionally, many cellular responses are regulated by mechanisms controlling changes in protein concentration in space, including translocation of transcription factors from the cytosol to the nucleus [157], release of mitochondrial proteins into the cytosol during apoptosis [158], endocytic recycling of plasma membrane proteins [159], and scaffold recruitment and release of signaling pathway components [160]. Spatial organization of cellular components is also of vital importance in cellular manufacturing of proteins and metabolites [161], as it provides a mechanism for accelerating reactions [162], [163] and reducing interference between pathways with shared components [164]. Furthermore, aberrant localization of proteins has been associated with disease states including neurodegeneration [165]–[167], metabolic impairment [168], [169] and cancer [170], [171]. Perturbing cellular protein levels and monitoring the associated phenotypic changes is thus a powerful approach to investigate biological pathways [172]–[174]. Similarly, characterization of the physiological role of protein localization in the complex milieu of mammalian cells depends on tools to precisely perturb the location of cellular proteins while monitoring the associated phenotypic changes [8], [175].

Defined sequences that determine protein location have been used to impart novel localization of target proteins through direct fusion of such sequences to the protein of interest [12], [146]. This approach, however, requires genetic

manipulations of the target protein, which may potentially affect the protein's native function [176], [177]. In addition, the efficiency of protein localization is largely target-specific [178], [179]. Control over the location of a target protein can also be achieved through engineered inducible interactions between a protein residing at the location of interest and the target protein. This approach to regulate protein localization requires extensive genetic manipulation and is generally achieved through fusion of a dimerizing domain to a protein at the desired location and the complementary dimerizing domain to the target protein. Small molecule [180]–[184] or light [185]–[187] inducible fragment complementation has been widely used to control localization of a target protein. These systems, however, are limited by the requirement for a binding partner with the correct subcellular address and that is amenable to protein engineering. Generally speaking, regulating localization of proteins based on fusion to a signal sequence or dimerization domain is a cumbersome endeavor due to the need to modify each target individually. Furthermore, the availability of a restricted number of inducible dimerization domains [180] limits the development of strategies for directing single targets to multiple compartments or for multiplexing control of multiple targets. An alternative approach to control location of cellular proteins relies on the use of binding proteins (DARPs, antibody fragments, and nanobodies) functionalized with localization signals [188]–[190]. While this approach provides a powerful tool to investigate the role of protein subcellular localization in determining protein

function that circumvents the need to modify the target protein, it does not allow for user-defined control over the extent and dynamics of target localization.

In this chapter, I addressed the need for a platform technology for regulating the localization of cellular proteins that can be adapted to any cellular target protein, provides dynamic control of the protein levels at the desired subcellular location, and allows modulating subcellular localization of a single target to multiple compartments. In this regard, I constructed a nanobody-based platform for tunable control of target protein localization. Specifically, I built a toolbox of nanobodies functionalized to direct a target to a series of subcellular compartments (NanoLoc). I demonstrated nanobody-mediated localization of a target protein depends on the expression level of the nanobody and of the target protein. I developed a method to modulate the extent of target subcellular localization based on combining the use of target-specific nanobodies mediating localization (VHH_{Loc}) and degradation [37] (VHH_{Deg}). Finally, I interfaced this toolkit for nanobody-mediated target localization and degradation with different strategies for transcriptional regulation of the nanobody to achieve spatial and temporal control of the target protein localization.

5.2. Results

5.2.1. Design of a nanobody-based platform for spatial control of GFP.

To build a platform technology for controlling the subcellular localization of a target protein that could be adapted to target any cellular protein to different

cellular compartments, I built a set of GFP-specific nanobody (VHH) [191] variants fused to different localization signals, namely the mitochondrial outer membrane anchor (VHH_{MOM}) [192], the endoplasmic reticulum membrane anchor (VHH_{ERM}) [193], the peroxisome targeting signal (VHH_{PEX}) [194], the plasma membrane anchor (VHH_{PM}) [195], and the nuclear localization signal (VHH_{NLS}) [196] (Table 5.4.1). All nanobody variants (VHH_{Loc}) contained the HA tag for detection. To verify that the resulting VHH_{Loc} variants localize cytosolic GFP to the corresponding subcellular compartments, I analyzed the colocalization of VHH_{Loc}, GFP, and the subcellular compartment designated by the localization tag. Specifically, HEK293 cells stably expressing GFP (HEK293/GFP#1) were transiently transfected for the expression of the VHH_{Loc} variants. Cells were analyzed by confocal microscopy for detection of GFP, VHH (anti-HA), and the subcellular compartments, namely the mitochondria (MitoTracker stain), endoplasmic reticulum membrane (anti-CANX), peroxisome (anti-PMP70), plasma membrane (MemBrite stain), or nucleus (Hoechst stain). Imaging analyses revealed a distinct GFP and VHH distribution pattern in cells transfected for the expression of each VHH_{Loc}. Specifically, the VHH_{Loc} signal was found to colocalize with the subcellular compartment marker, indicating that the localization signal controls the VHH subcellular localization (Figure 5.1, merge compartment-VHH, purple). GFP and VHH_{Loc} signals also colocalized, suggesting formation of the GFP-VHH complex (Figure 5.1, merge GFP-VHH, cyan). Finally, colocalization of GFP and the subcellular compartment marker indicates that VHH_{Loc} controls GFP localization (Figure 5.1, merge Compartment-GFP, yellow).

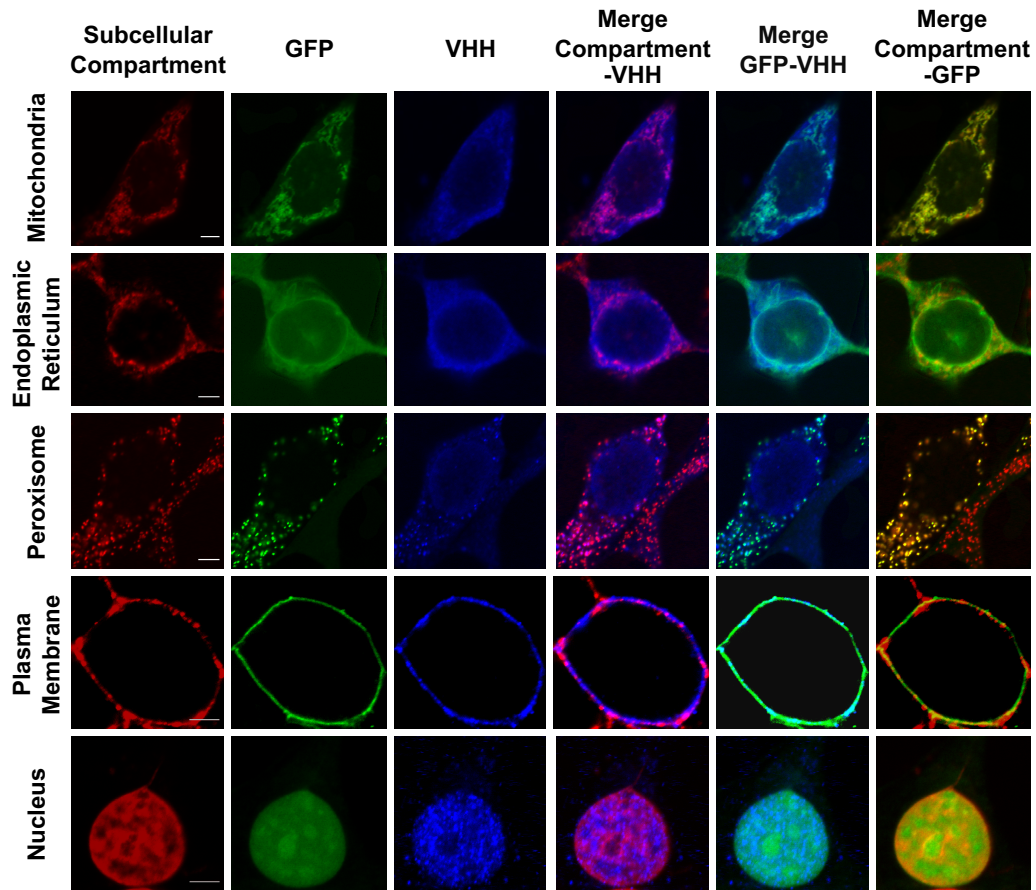


Figure 5.1 NanoLoc-mediated control of GFP subcellular localization. Representative confocal microscopy images of HEK293/GFP#1 cells transiently transfected for expression of VHH_{Loc} variants and analyzed 72 h post-transfection. Subcellular compartment (red, column 1); GFP (green, column 2); VHH (blue, anti-HA, column 3); colocalization of subcellular compartment and VHH shown in merged images (purple, column 4); colocalization of GFP and VHH shown in merged images (cyan, column 5); colocalization of subcellular compartment and GFP shown in merged images (yellow, column 6). All scale bars are 5 μ m. Brightness and contrast levels were minimally adjusted. Pseudo-coloring was applied to the subcellular compartment stain and VHH images for the plasma membrane and the nucleus.

Cells transfected with a control plasmid lacking the gene encoding the nanobody

display a diffuse GFP signal that does not colocalize with the fluorescent signal of

any of the compartment markers (Figure 5.2), confirming that VHH_{Loc} controls GFP localization to the compartment designated by the localization signal.

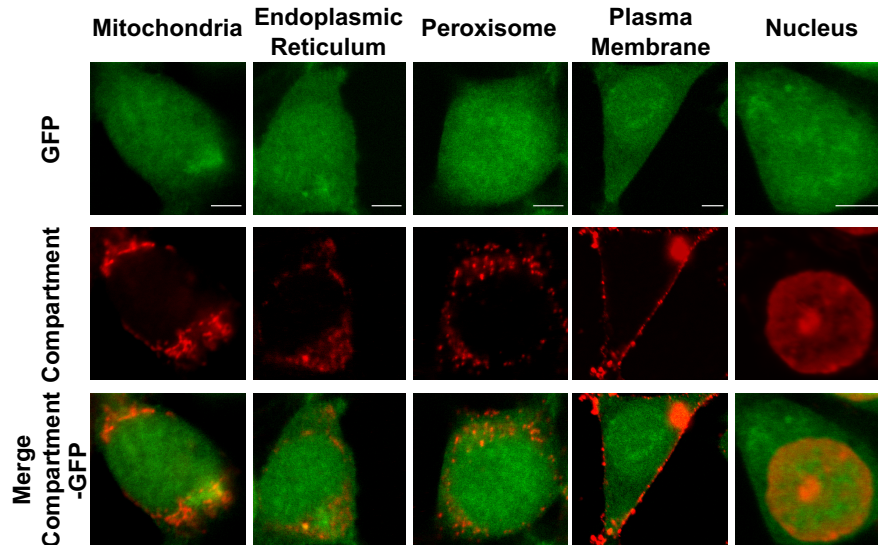


Figure 5.2 GFP subcellular localization in the absence of NanoLoc. Representative confocal microscopy images of HEK293/GFP#1 cells transiently transfected with a control plasmid lacking the *vhh* gene and analyzed 72 h post-transfection. GFP (green, row 1); subcellular compartment (red, row 2); colocalization of subcellular compartment and GFP shown in merged images (row 3). All scale bars are 5 μ m. Brightness and contrast levels were minimally adjusted.

To test the residence time of GFP within each subcellular compartment, I monitored GFP fluorescence over time in cells expressing the VHH_{Loc} variants. HEK293/GFP#1 cells stably expressing the erythromycin-dependent transrepressor (EKRA) [197] were transiently transfected for the expression of each VHH_{Loc} under the control of the erythromycin-inducible operator and treated with erythromycin (Em) to induce expression of VHH_{Loc}. Confocal microscopy analyses were initiated at the time of removal of Em from the culturing medium. Localization of GFP to the ER membrane and plasma membrane decayed rapidly with complete loss of

localization by 48 h and 72 h, respectively. Nuclear localization of GFP appeared stable for the first 72 h, followed by a slow decay and complete loss of localization by 120 h. Peroxisomal and mitochondrial localization presented similar temporal patterns resulting in total loss of localization by 144 h (Figure 5.3). These results are indicative of a compartment-specific localization decay rate, which may be due to a multitude of factors including different compartment turnover rates and localization mechanisms.

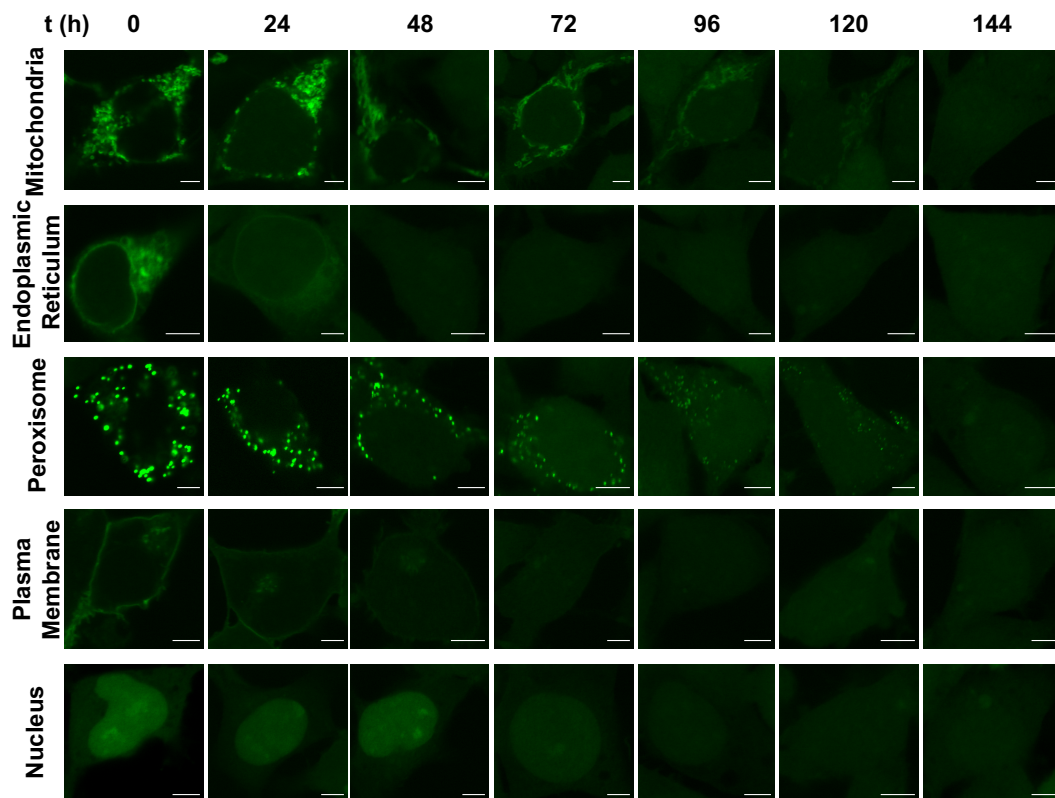


Figure 5.3 Residence time of NanoLoc-mediated GFP subcellular localization. Representative confocal microscopy images of HEK293/GFP2R cells transiently transfected for the expression of different VHH_{Loc} variants and induced with erythromycin (Em, 500 ng/mL) 8 h post-transfection. Em was removed from the media and time-course analyses initiated (t = 0 h) after 24 h of Em treatment. Time-course analyses were conducted every 24 h for 144 h. All scale bars are 5 μ m.

Brightness levels were minimally adjusted and all images were subjected to the same adjustment.

To test whether GFP can be simultaneously targeted to multiple subcellular compartments, HEK293/GFP#1 cells were co-transfected for the expression of two VHH_{Loc} variants fused to different localization signals. Expression of a single VHH_{Loc} displayed the pattern of GFP fluorescence consistent with GFP localization to the designated compartment (Figure 5.4A). Expression of two distinct VHH_{Loc}, however, resulted in a pattern of GFP fluorescence consistent with GFP localization in two distinct compartments for all combinations of VHH_{Loc} tested (Figure 5.4B). These results indicate that a cytosolic protein can be localized simultaneously to multiple subcellular compartments through co-expression of the appropriate VHH_{Loc} variants.

To test the extent to which the VHH_{Loc} expression level affects GFP localization, I monitored GFP localization within a representative subcellular compartment (mitochondria) upon modulation of the corresponding VHH_{Loc} variant (VHH_{MOM}) expression level. Specifically, HEK293/GFP#1 cells were transiently transfected with varying amounts of VHH_{MOM} expressing plasmid (10 - 450 ng) and the extent of colocalization of GFP and MitoTracker stain quantified as a function of plasmid amount. Transfected cells were selected and analyzed based on expression of the transfection control (iRFP), and the GFP signal of transfected cells that colocalized with the mitochondria stain was quantified [198]. Localization of GFP to the mitochondria was found to depend on VHH_{MOM} expression level until a

saturation point. Specifically, the extent of mitochondria-localized GFP in HEK293/GFP#1 cells increased exponentially (20 - 150 ng of plasmid) until a 16.5-fold maximum compared to cells not expressing VHH_{MOM} and plateaued upon transfection with higher amounts of VHH_{MOM} expressing plasmid (Figure 5.5A).

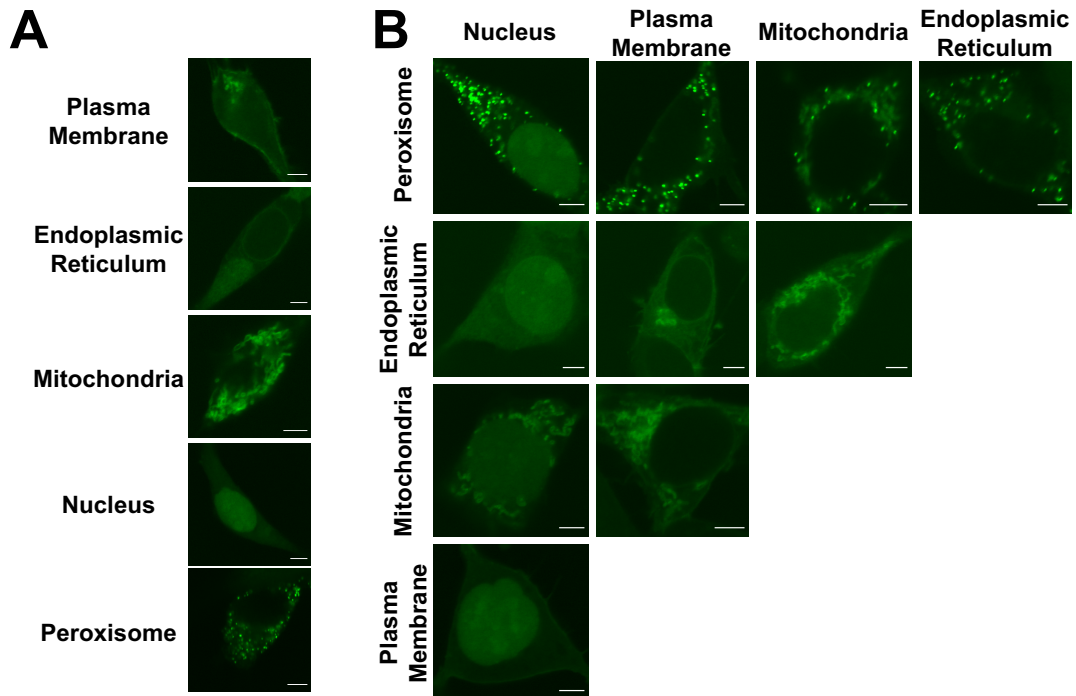


Figure 5.4 Dual-compartment subcellular localization of GFP with the NanoLoc. Representative confocal microscopy images of HEK293/GFP#1 cells transiently transfected for expression of (A) a single VHH_{Loc} variant or (B) two VHH_{Loc} variants (using a 1:1 plasmid ratio). Samples were analyzed 72 h post-transfection. All scale bars are 5 μm. Brightness levels were minimally adjusted.

To further characterize VHH_{Loc}-mediated localization, I investigated the effect of GFP expression level on GFP localization by quantifying mitochondria-localized GFP fluorescence in cells presenting different GFP expression levels. Specifically, three stable HEK293 cell lines expressing different GFP levels, namely

HEK293/GFP#1 (low), HEK293/GFP#2 (intermediate), and HEK293/GFP#3 (high) were transiently transfected with saturating amount of VHH_{MOM} expressing plasmid (450 ng, Figure 5.5A) expected to maximize GFP localization. Total GFP fluorescence levels of the HEK293/GFP cell lines were measured by flow cytometry (Figure 5.5C). Transfected cells were analyzed by confocal microscopy to evaluate the extent of GFP localization to the mitochondria (Figure 5.5B). These analyses revealed that GFP localization to the mitochondria depends on the total level of GFP. Specifically, mitochondria-localized GFP fluorescence of HEK293/GFP#2 and HEK293/GFP#3 cells was 2.8-fold and 6.7-fold to that of HEK293/GFP#1 cells, respectively, reflecting the 6.3-fold and 15.4-fold increase in total GFP fluorescence levels in HEK293/GFP#2 and HEK293/GFP#3 cells compared to HEK293/GFP#1 cells (Figure 5.5B and C).

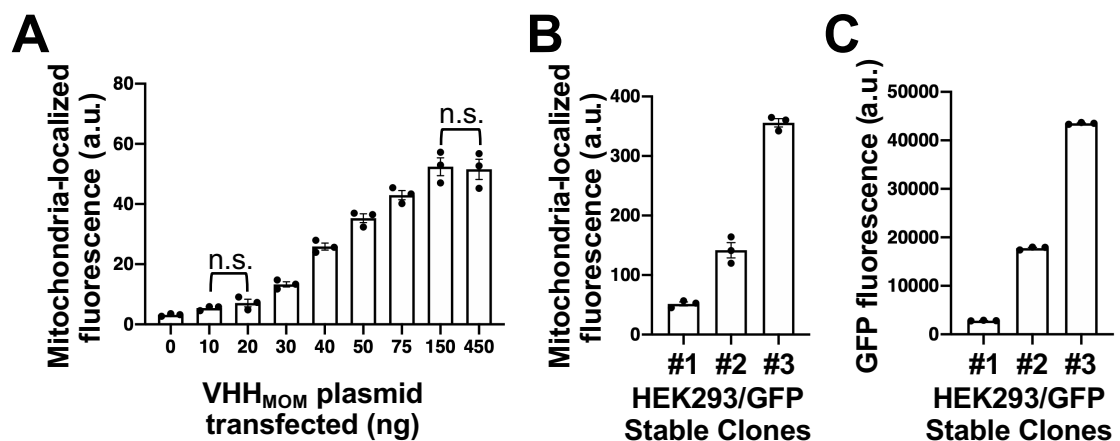


Figure 5.5 GFP mitochondrial localization as a function of VHH_{MOM} and GFP expression level. (A) Confocal microscopy analyses of HEK293/GFP#1 cells transiently transfected for the expression of VHH_{MOM} and analyzed 72 h post-transfection. Data are reported as mean \pm s.e.m. ($n = 3$, $p < 0.05$, Student's t -test, n.s = not significant). Black dots represent the biological replicates. (B) Confocal

microscopy analyses of mitochondria-localized GFP fluorescence in stable HEK293 cell lines presenting low (HEK293/GFP#1), intermediate (HEK293/GFP#2), and high (HEK293/GFP#3) GFP expression levels and transiently transfected with 450 ng of plasmid expressing VHH_{MOM}. (C) Mean GFP fluorescence intensity of three HEK293/GFP stable cells detected by flow cytometry. Data are reported as mean \pm s.e.m. (n = 3, $p < 0.05$, Student's *t*-test). Black dots represent the biological replicates.

These results, taken together, demonstrate that the level of a cytosolic target protein localized to a specific compartment can be tuned using the NanoLoc platform by modulating the expression level of the VHH_{Loc} variant relative to the expression level of the target protein.

To investigate whether the extent of target protein subcellular localization could be modulated post-translationally by controlling the target protein degradation rate, I combined nanobody-mediated modulation of GFP subcellular localization and degradation rate. GFP degradation rate was controlled using the previously developed NanoDeg platform consisting of a target-specific nanobody variants fused to a degradation tag (VHH_{Deg}) [37]. HEK293/GFP#1 cells were transiently transfected for the expression of VHH_{MOM} and varying amounts of a VHH_{Deg} variant containing the 37 amino acid carboxy-terminal sequence of ornithine decarboxylase (VHH_{ODC}) [199]. Transfected cells were analyzed by confocal microscopy to quantify mitochondria-localized GFP fluorescence. Co-expression of VHH_{MOM} and VHH_{ODC} resulted in a reduction of mitochondria-localized GFP fluorescence compared to control cells lacking VHH_{ODC} which was proportional to the amount of VHH_{ODC}-encoding plasmid (Figure 5.6A). Localized GFP fluorescence was reduced by 66%, 81% and 92% in cells expressing a VHH_{MOM} to

VHH_{ODC} ratio of 1:0.5, 1:2 and 1:3, respectively, compared to control cells (Figure 5.6B).

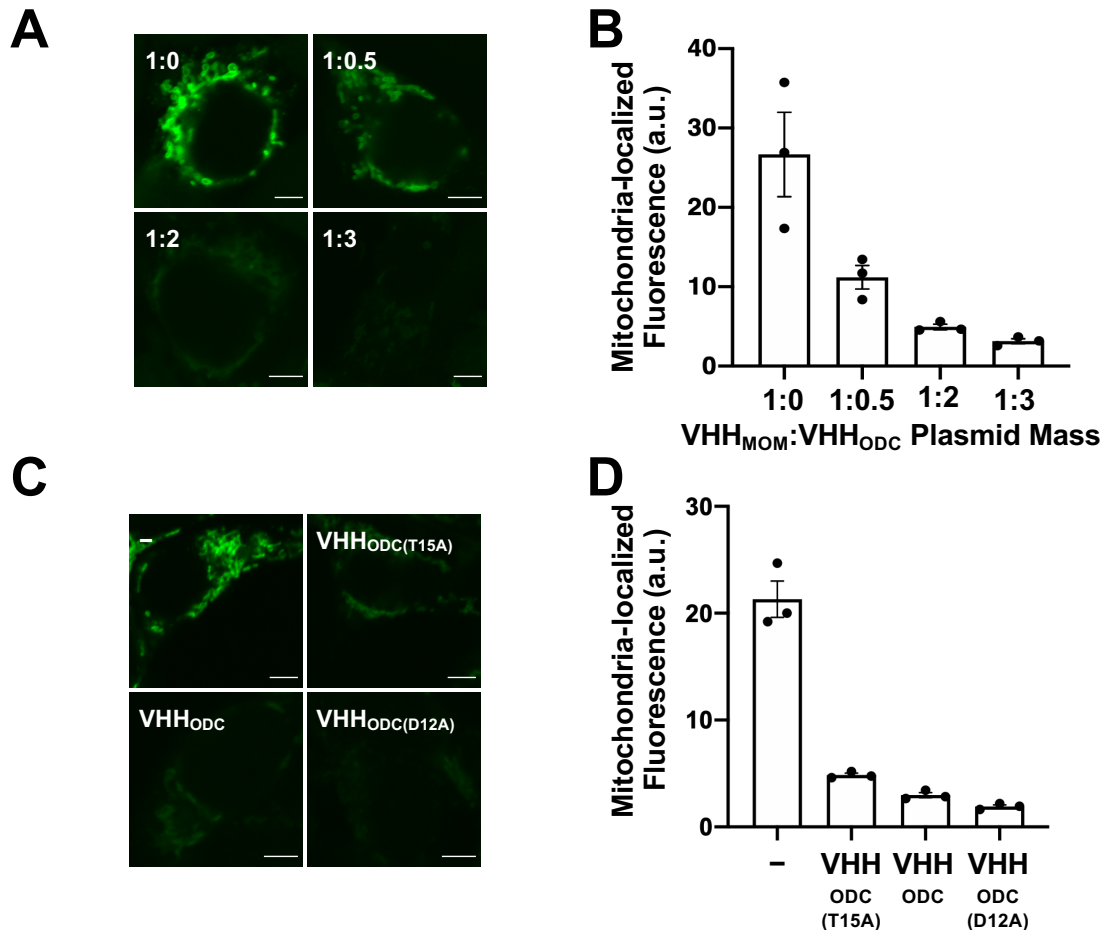


Figure 5.6 Modulation of mitochondria-localized GFP fluorescence using the NanoDeg. (A-B) Confocal microscopy analyses of HEK293/GFP#1 cells transiently transfected for the expression of VHH_{MOM} and VHH_{ODC}. Transfection reactions were conducted using VHH_{MOM}:VHH_{ODC} plasmid mass ratios of 1:0, 1:0.5, 1:2, and 1:3 and a filler plasmid lacking *vhh* to maintain total plasmid mass constant. Images were analyzed 72 h post-transfection. (A) Representative images of mitochondria-localized GFP fluorescence. All scale bars are 5 μ m. Brightness levels were minimally adjusted and all images were subjected to the same adjustment. (B) Average mitochondria-localized GFP fluorescence. Data are reported as mean \pm s.e.m. ($n = 3$, $p < 0.005$, Student's *t*-test). Black dots represent biological replicates. (C-D) Confocal microscopy analyses of HEK293/GFP#1 cells transiently transfected with a plasmid expressing VHH_{MOM} and a plasmid expressing a VHH_{ODC} variant (VHH_{ODC}(T15A), half-life 2.1 h; VHH_{ODC}, half-life 1.3 h; and VHH_{ODC}(D12A), half-life 0.9 h)

or lacking *vhh* in a 1:2 mass ratio and analyzed 72 h post-transfection. (C) Representative images of mitochondria-localized GFP fluorescence. All scale bars are 5 μm . Brightness levels were minimally adjusted and all images were subjected to the same adjustment. (D) Average mitochondria-localized GFP fluorescence. Data are reported as mean \pm s.e.m. ($n = 3$, $p < 0.005$, Student's *t*-test). Black dots represent biological replicates.

To investigate whether GFP subcellular localization could be further tuned by modulating the VHH_{ODC} degradation rate, rather than its expression level, I tested GFP localization upon expression of VHH_{ODC} variants presenting different half-lives. I used a set of VHH_{ODC} variants containing mutations in the ODC tag [13] that alter VHH_{ODC} half-life[37], namely $\text{VHH}_{\text{ODC}(\text{T15A})}$, VHH_{ODC} , and $\text{VHH}_{\text{ODC}(\text{D12A})}$, which were reported to present half-lives of 2.1 h, 1.3 h, and 0.9 h, respectively [37]. HEK293/GFP#1 cells were transiently transfected for the expression of VHH_{MOM} and $\text{VHH}_{\text{ODC}(\text{T15A})}$, VHH_{ODC} , or $\text{VHH}_{\text{ODC}(\text{D12A})}$ and analyzed by confocal microscopy to quantify mitochondria-localized GFP fluorescence. Imaging analyses revealed a reduction in mitochondria-localized GFP fluorescence compared to control cells that was proportional to the VHH_{ODC} variant half-life. Localized GFP fluorescence was reduced by 67%, 80%, and 87% in cells expressing $\text{VHH}_{\text{ODC}(\text{T15A})}$, VHH_{ODC} , and $\text{VHH}_{\text{ODC}(\text{D12A})}$, respectively, compared to control cells (Figure 5.6C-D).

These results support the use of the NanoLoc and NanoDeg platforms in conjunction to modulate the target protein concentration in a specific subcellular compartment by tuning nanobody-mediated localization and nanobody-mediated degradation and that thus does not require genetic manipulation of the target protein.

5.2.2. Tuning GFP localization by modulating nanobody-mediated control of GFP localization and degradation.

To investigate whether the NanoLoc and NanoDeg platforms can be adapted to achieve temporal control of the target protein localization, I built a system to control the expression of multiple VHH variants. As proof-of-principle, I built the simplest configuration consisting of a dual-input system in which the expression of two VHH variants is regulated by inducible promoters. Specifically, I designed a system in which the expression of the two VHH variants are independently controlled by the tetracycline repressor (TetR) [200] and erythromycin-dependent transrepressor (EKRA), and can thus be independently regulated using the small-molecule inducers tetracycline (Tc) and erythromycin (Em), respectively (Figure 5.8A). To build this system, a stable cell line (HEK293/GFP2R) expressing GFP, TetR, and EKRA. Induction of gene expression was characterized by transiently transfecting HEK293/GFP2R cells for the expression of iRFP regulated by EKRA or TetR was generated. Transfected cells were treated with the corresponding inducer and analyzed by flow cytometry to define the transgene expression levels as a function of inducer concentration (Figure 5.7). The expression of VHH variants in the dual-input system regulated by EKRA or TetR is expected to be comparable to that of iRFP under the same conditions.

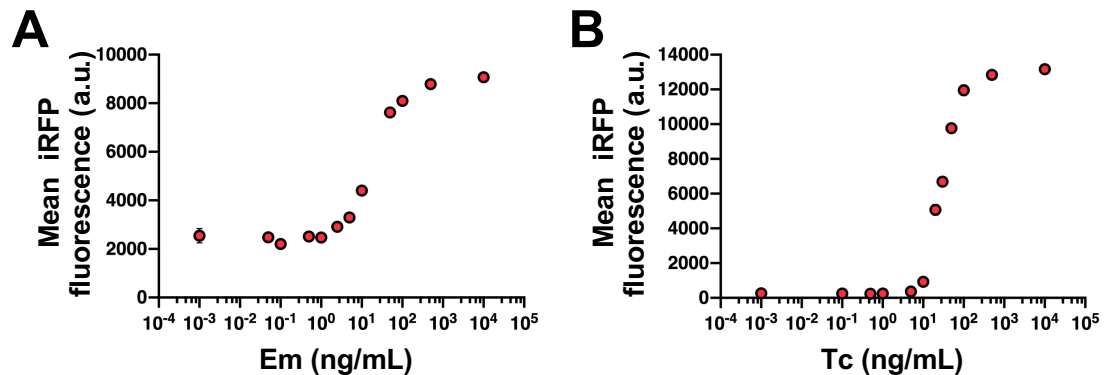


Figure 5.7 Induction of iRFP expression in the dual-input system. (A) HEK293/GFP2R cells transiently transfected for the expression of iRFP under the control of the Em-inducible operator were treated with Em (0 - 10 $\mu\text{g/mL}$) 16 h post-transfection and analyzed by flow cytometry after 48 h of Em treatment. (B) HEK293/GFP2R cells transiently transfected for the expression of iRFP under the control of the Tc-inducible operator were treated with Tc (0 - 10 $\mu\text{g/mL}$) 16 h post-transfection and analyzed by flow cytometry after 48 h of Tc treatment. Data are reported as mean \pm s.e.m. ($n = 3$).

To test whether the extent of target protein localization to an extracytosolic compartment can be modulated by controlling the target degradation rate after induction of subcellular localization, I explored the use of a VHH_{Loc} to first induce target subcellular localization followed by expression of a VHH_{Deg} to control target degradation rate. Specifically, I implemented the dual-input system by transiently transfecting HEK293/GFP2R cells for the expression of VHH_{MOM} under control of the Tc-inducible operator and the expression of VHH_{ODC} under control of the Em-inducible operator. Transfected cells were first treated with Tc to induce expression of VHH_{MOM}. The resulting sample presenting localization of GFP to the mitochondria (Figure 5.8B, left) was cultured in the absence of Tc discontinuing expression of VHH_{MOM} to evaluate the residence time of GFP in the mitochondria (Figure 5.8B, top right). A sample of cells cultured in the absence of Tc was also exposed to Em

inducing expression of VHH_{ODC} to evaluate whether VHH_{ODC}-mediated degradation results in depletion of mitochondrial GFP (Figure 5.8B, bottom right). Confocal microscopy analyses of mitochondria-localized GFP fluorescence revealed that cells not exposed to Em and thus not expressing VHH_{ODC} present minimal decrease in mitochondria-localized GFP fluorescence compared to cells analyzed at the end of the Tc induction period. Induction of VHH_{ODC} via cell treatment with Em, on the other hand, resulted in 87% decrease in mitochondria-localized GFP fluorescence (Figure 5.8C). These results demonstrate the residence time of a target protein localized in a subcellular compartment can be modulated by controlling proteasome-mediated degradation of the target protein.

To test whether the extent of target protein localization to distinct extracytosolic compartments can be modulated by controlling the expression level of the corresponding VHH_{Loc} variants, I monitored GFP signal in two subcellular compartments (mitochondria and nucleus) upon modulation of the expression level of two VHH_{Loc} variants (VHH_{MOM} and VHH_{NLS}). Specifically, I used the dual-input system to induce expression of VHH_{MOM} under the control of the Em-inducible operator and VHH_{NLS} under the control of the Tc-inducible operator. Cells were treated with Em and Tc, separately or in combination, at concentrations estimated from iRFP induction analyses to result in linear changes in target gene expression (Figure 5.7). Localization of GFP to the mitochondria and nuclei was assessed using confocal microscopy.

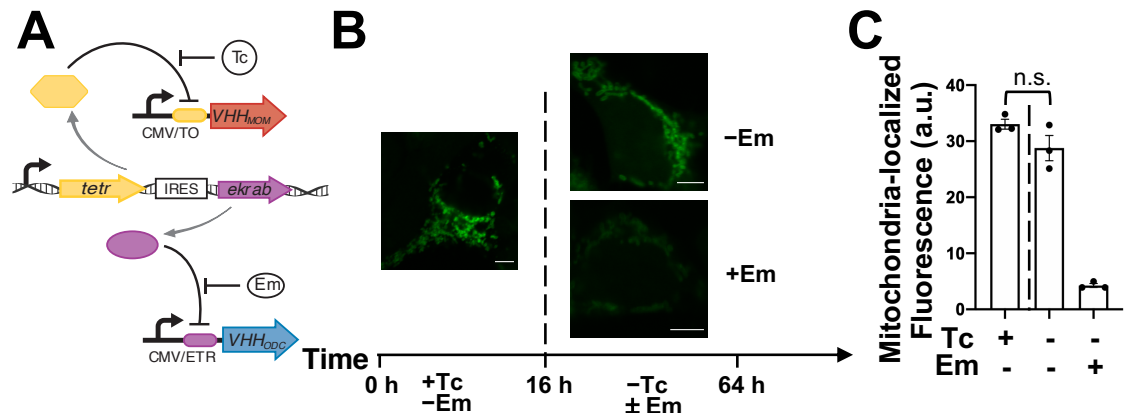


Figure 5.8 A dual-input NanoLoc and NanoDeg system for temporal control of GFP localization. (A) Schematic representation of the dual-input system to control expression of two VHH variants. The tetracycline repressor (TetR) and erythromycin-dependent transrepressor (EKRA) are constitutively expressed from a single promoter. Expression from a promoter containing TetR operator sites (TO) is induced with tetracycline (Tc) and expression from a promoter containing EKRA operator sites (ETR) is induced with erythromycin (Em). (B-C) Confocal microscopy analyses of HEK293/GFP2R cells transiently transfected with VHH_{MOM} under control of the Tc-inducible operator and VHH_{ODC} under control of the Em-inducible operator. Cells were cultured in the presence of Tc (50ng/ml) for the first 16 h and then in the presence or absence of Em (500 ng/mL) for an additional 48 h. (B) Representative images of cells at 16 h (Tc treatment, left) and 64 h (right. Em free media, top; Em supplemented media, bottom). The scale bar for all images is 5 μm. (C) Average mitochondria-localized GFP fluorescence of cells analyzed at 16 h (left of dashed line) and 64 h (right of dashed line) post-transfection. Data are reported as mean ± s.e.m. (n = 3, p < 0.01, Student's t-test). Black dots represent biological replicates.

Cell treatment with Em resulted in an increase in mitochondria-localized GFP fluorescence to a 7.9-fold maximum compared to untreated cells and did not affect localization of GFP to the nucleus (Figure 5.9A). Cell treatment with Tc resulted in an increase in nucleus-localized GFP fluorescence to a 2.2-fold maximum compared to untreated cells and did not affect localization of GFP to the mitochondria (Figure 5.9B). Cells exposed to Em and Tc displayed GFP localization to both the nucleus and mitochondria (Figure 5.9C). The extent of GFP colocalization with the nucleus and

the mitochondria depended on the concentration of Em and Tc and thus on the expression level of the compartment-specific VHH_{Loc} variants (Figure 5.9D). These results demonstrate localization of a target protein can be quantitatively tuned between different subcellular compartments by modulating the expression of the appropriate VHH_{Loc} variants.

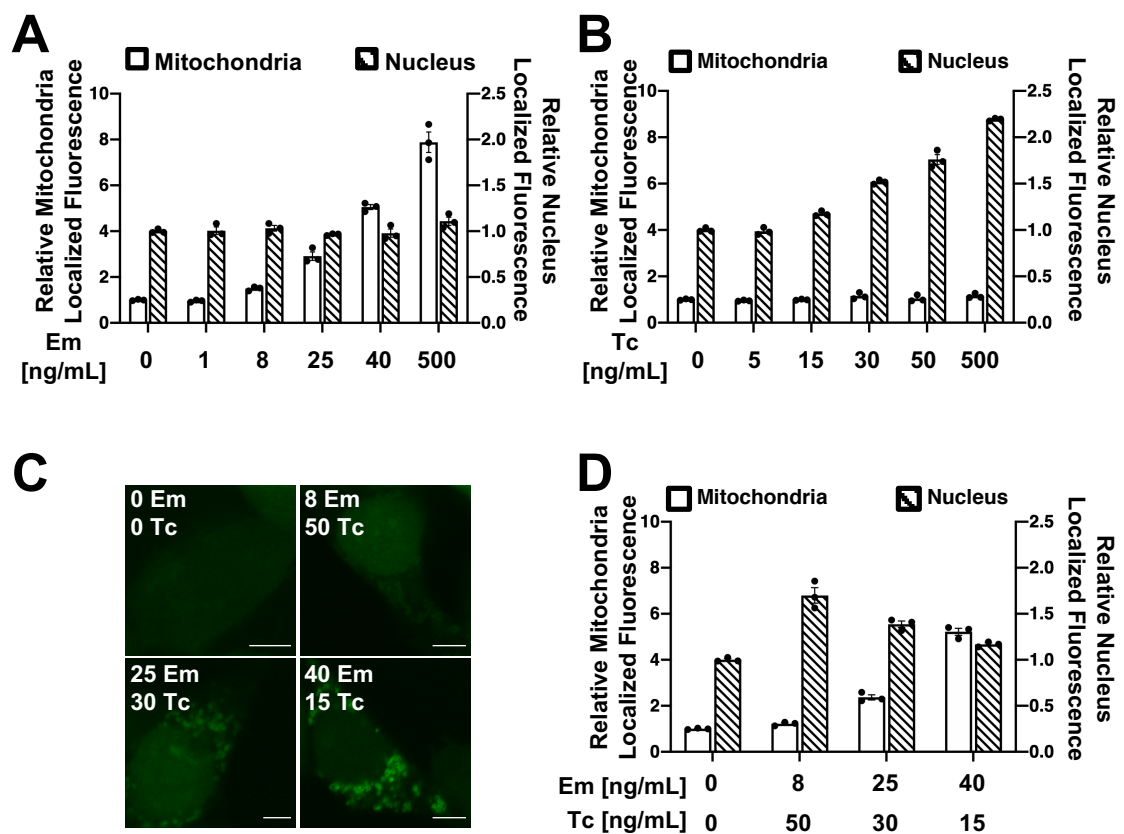


Figure 5.9 Modulation of GFP localization to the mitochondria and the nucleus using a dual-input NanoLoc expression system. (A-D) Confocal microscopy analyses of HEK293/GFP2R cells transiently transfected for the expression of VHHMOM under control of the Em-inducible operator and VHHNLS under control of the Tc-inducible operator. Cells were treated with Em and Tc 16 h post-transfection and analyzed after 48 h of induction with Em and Tc. (A) Transfected cells cultured in the presence of Em (0-500 ng/mL) and in the absence of Tc. Relative GFP fluorescence that colocalizes with the mitochondria (red bars) and with the nucleus (blue bars) as a function of Em concentration obtained by normalizing the localized GFP fluorescence values of each sample to that of uninduced cells. (B) Transfected cells

cultured in the presence of Tc (0-500 ng/mL) and in the absence of Em. Cells treated with increasing concentration of Tc. Relative GFP fluorescence that colocalizes with the mitochondria (red bars) and with the nucleus (blue bars) as a function of Tc concentration obtained by normalizing the localized GFP fluorescence values of each sample to that of uninduced cells. (C) Representative images of cells treated with Tc and Em. The scale bar for all images is 5 μm . Brightness levels were minimally adjusted and all images were subjected to the same adjustment. (D) Transfected cells cultured in the presence of both Em and Tc. Relative GFP fluorescence that colocalizes with the mitochondria (red bars) and with the nucleus (blue bars) as a function of Em and Tc concentration obtained by normalizing the localized GFP fluorescence values of each sample to that of uninduced cells. All data are reported as mean \pm s.e.m. ($n = 3$, $p < 0.05$, Student's t-test). Black dots represent biological replicates.

5.2.3. Design of a Genetic Toggle Switch for Spatial Control of GFP Output.

To investigate the use of NanoLoc to spatially control the output of genetic circuits, I built a genetic toggle switch circuit that regulates expression of two VHH_{Loc} variants such that the state of the toggle switch dictates the expression of each VHH_{Loc} variant and the resulting subcellular localization of the target protein. Toggle switch topologies in bacteria [78], [201], [202] and mammalian cells [49], [203], [204] are typically based on the function of two transcriptional repressors that mutually repress each other. To generate a toggle switch for spatial control of GFP localization between two subcellular compartments, I modified the classic toggle switch configuration [201], [203] to link the expression of two VHH_{Loc} variants to that of the two repressors through an internal ribosome entry site (IRES) sequence (Figure 5.10A). Specifically, HEK293/GFP#1 cells were transiently transfected for the expression of VHH_{MOM} and EKCRAB under the control of the Pristinimycin I (PI)-inducible operator and VHH_{NLS} and PIPCRAB under the control of the Em-inducible operator. The same IRES was used to link expression of VHH_{MOM}

and VHH_{NLS} to that of EKCRAB and PIPCRAB to ensure equal ratios of expression. Transfected cells were treated with Em and PI and imaged by confocal microscopy to quantify GFP localization and verify that the state of the toggle switch determines the target's subcellular localization.

To investigate the use of the spatial toggle switch to shift localization of GFP from the nucleus to the mitochondria, transfected HEK293/GFP#1 cells expressing the mutually repressed VHH_{Loc} variants were treated with pulses of Em and PI. Specifically, cells were treated with PI during transfection to initialize the toggle to mitochondrial localization by inducing expression of VHH_{MOM} and PIPCRAB. Transfected cells were first treated with Em for 48 h to induce expression of VHH_{NLS} (and EKCRAB), resulting in repression of VHH_{MOM} (and PIPCRAB), and then with PI for an additional 48 h to induce expression of VHH_{MOM} (and PIPCRAB), resulting in repression of VHH_{NLS} (and EKCRAB). Control cells treated continuously with Em or PI to maximize expression of VHH_{NLS} or VHH_{MOM}, respectively, provided measurements of maximum localization of GFP to the mitochondria (PI treatment, Figure 5.10B-D solid lines) or the nucleus (Em treatment, Figure 5.10B-D, dashed lines) in the spatial toggle switch. Imaging analyses at the end of the Em treatment (Figure 5.10B, 48 h) showed low mitochondrial localization (left) and high nuclear localization (right) and that the extent of localization to both the mitochondria and the nucleus is comparable to that observed in cells treated continuously with Em. After the switch to PI treatment (Figure 5.10B, 96 h), cells displayed high mitochondrial localization (left) and low nuclear localization (right) and the extent

of localization to both the mitochondria and the nucleus was comparable to that observed in cells treated continuously with PI (Figure 5.10B). These results indicate that GFP localization is switched from a state of predominantly nucleus-localized GFP to a state of predominantly mitochondria-localized GFP by switching from expression of VHH_{NLS} to expression of VHH_{MOM}.

To demonstrate reversible switching of the toggle, I tested the opposite transition from mitochondria-localized GFP to nucleus-localized GFP. Specifically, cells were transiently transfected for expression of the spatial toggle switch in the presence of Em to initialize the toggle to nuclear localization by inducing expression of VHH_{NLS} and EK_{RAB}. Transfected cells were first treated with PI for 48 h to induce expression of VHH_{MOM} (and PIP_{KRAB}), resulting in repression of VHH_{NLS} (and EK_{RAB}), and then with Em for an additional 48 h to induce expression of VHH_{NLS} (and EK_{RAB}), resulting in repression of VHH_{MOM} (and PIP_{KRAB}). Confocal microscopy analyses of GFP subcellular localization at the end of PI treatment (Figure 5.10C, 48 h) showed high mitochondrial localization (left) and low nuclear localization (right). Similar to the previous experiment, the extent of localization to both the mitochondria and the nucleus was comparable to that observed in cells treated continuously with PI. After the switch to Em treatment (Figure 5.10C, 96 h), cells displayed low mitochondrial localization (left) and high nuclear localization (right) at levels corresponding to those observed in cells treated continuously with Em (Figure 5.10C), indicating a shift from nuclear to mitochondrial localization upon switch of the expression of VHH_{Loc}.

These results (Figure 5.10B and C), taken together, indicate that localization of the target protein can be reversibly switched between the mitochondria and the nucleus by switching the state of the spatial toggle switch circuit.

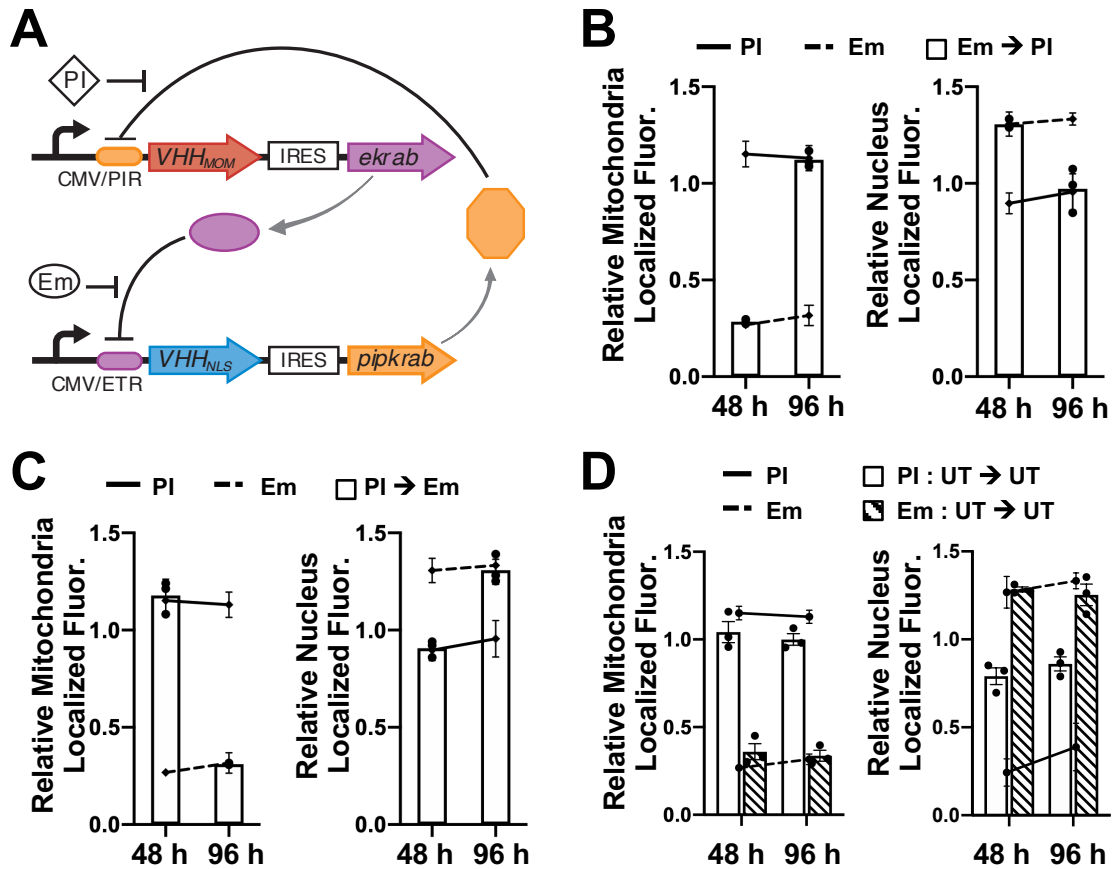


Figure 5.10 A synthetic toggle switch with NanoLoc to control GFP subcellular localization. (A) Schematic representation of the spatial toggle switch. (B-D) Confocal microscopy analyses of HEK293/GFP#1 cells transiently transfected with plasmids for expression of the spatial toggle switch as shown in A. Relative localized GFP fluorescence values were obtained by normalizing the localized GFP fluorescence values of each sample to that of uninduced cells. (B) Cells were cultured in the presence of PI during transfection to initialize cells to VHH_{MOM} and PIPKRAB expression. Following transfection, cells were cultured in the presence of Em (500 ng/mL) for the first 48 h and then in the presence of PI (500 ng/mL) for other 48 h. Cells were analyzed at the end of Em treatment (48 h) and at the end of PI treatment (96 h). Control cells were cultured continuously in the presence of PI (solid line) and Em (dashed line). (C) Cells were cultured in the presence of Em during transfection to initialize cells to VHH_{NLS} and EKRAB expression. Following

transfection, cells were cultured in the presence of PI (500 ng/mL) for the first 48 h and then in the presence of Em (500 ng/mL) for other 48 h. Cells were analyzed at the end of PI treatment (48 h) and at the end of Em treatment (96 h). Control cells were cultured continuously in the presence of PI (solid line) and Em (dashed line). (D) Cells were cultured in the presence PI (white bars) or Em (diagonal line bars) during transfection (16 h) and then in inducer-free medium for 96 h. Cells were analyzed at 48 h and 96 h after removal of the inducer. Control cells were cultured continuously in the presence of PI (solid line) and Em (dashed line). All data are reported as mean \pm s.e.m. ($n = 3$, $p < 0.05$, Student's *t*-test). Black dots represent biological replicates.

In addition to reversible switching, another key feature of the toggle switch topology is bistability of the system [201], [203]. Bistability is denoted by the presence of two path-dependent stable output states for given inputs (i.e., a fixed set of inducer concentrations) [132]. To demonstrate bistability of the spatial toggle switch, I treated cells with two different inducers to generate two different initial conditions and then removed the inducers to subject cells exposed to different initial conditions to a common input condition. I monitored GFP localization to verify if the outputs associated with each initial condition remained stable. Specifically, HEK293/GFP#1 cells were exposed to a pulse of either PI or EM during transient transfection for expression of the spatial toggle switch, and then incubated without inducer. Confocal microscopy analyses of GFP subcellular localization 48 h and 96 h after removal of PI (Figure 5.10D, white bars) showed high mitochondrial localization (left) and low nuclear localization (right). The extent of localization to both the mitochondria and the nucleus was again comparable to that observed in cells induced with PI and cultured continuously in the presence of PI for 96 h (Fig. 8D, solid line). Imaging analyses of cells treated with a pulse of Em (Figure 5.10D, striped bars) displayed low mitochondrial localization (left) and high nuclear

localization (right) at levels comparable to those observed in cells treated continuously with Em (dashed line). The GFP localization levels achieved upon cell exposure to a pulse of inducer were maintained for 96 h post-induction, indicating the spatial toggle switch displays bistable localization to either the mitochondria or the nucleus depending on the initial conditions of the circuit.

These results evince that the NanoLoc platform can be integrated within genetic circuits to exert spatial control over the outputs while maintaining key characteristics inherent to the circuit topology and providing an additional mode for control in synthetic gene networks.

5.3. Discussion

Strategies for user-defined control of protein subcellular localization allow investigating the role of specific proteins and their localization in a variety of cellular function [148], [150], [156], including mechanisms that mediate the cellular response to external stimuli [150]–[152], [154]. An array of intrinsic localization signals that dictate the subcellular address of proteins have been characterized [146]. Fusion of localization signals to target proteins enables protein relocation to the desired subcellular compartment [12], but requires genetic manipulation of the target protein, which may affect the protein's native function independently of localization [176]. Most importantly, direct fusion of target proteins to localization signals does not allow modulating the extent of target localization to the desired

subcellular compartment. Interacting protein domains have also been employed to engineer inducible localization systems in which the target and a compartment-specific protein are fused to interacting partners [180]–[188]. While providing an opportunity for tunable and reversible control of protein localization, these systems depend largely on the choice of binding partner and often require extensive development and re-engineering for customization to other target proteins. Regulating target localization through the use of target binding partners or recognition molecules functionalized with localization signals enables spatial control of the resulting complex without the need for target manipulation [189], [190], [205], [206]. Audenhove *et al* [190] described the role of fascin and cortactin in invadopodium formation through nanobody-mediated localization. Similarly, Beghein and colleagues [189] employed a survivin-targeting nanobody to trace and manipulate survivin localization during mitosis. These methods for targeted protein relocation do not, however, provide tunable control over the extent of target localization and typically result in irreversible localization. The potential of these strategies for the development of a universal, plug-and-play technology for reversible control of target localization that can be adapted to any cellular protein and used to direct localization to different subcellular compartments remains uncharacterized.

In this study, I addressed the need for a technology to control localization of cellular proteins with multi-compartment specificity, tunable control over the localized target concentration, and dynamic control over the target residence time. I

developed a modular system based on nanobodies, which are the smallest antigen recognition domain and could potentially be customized to target virtually any cellular protein [32], and a comprehensive series of localization signal sequences, which when fused to the target-specific nanobody determine location of the nanobody-target protein complex. Nanobodies are readily obtained from immunized Camelids [19]–[24] and can be evolved [25]–[30] or engineered [207] to target a seemingly unlimited number of sequences. The small size and stability of nanobodies allows for easy expression [208] and excellent tissue penetration [209]. I thus envision that this platform could be customized to target virtually any cellular protein sequence, conformation [33]–[35] or post-translational modification [33], [36].

Customization of the nanobody-based platform developed in this study with respect to the localization determining sequence allows user-defined control of target localization to any subcellular compartment [146]. The choice of localization signal also determines the target residence time within the signal-specific compartment. While the mechanistic features of localization signal-mediated control that affect the target residence time remain to be determined, the NanoLoc system could be further engineered by tuning the timescale of target localization. The reversible nature of the VHH_{Loc}-induced perturbation allows minimizing irreversible downstream effects and exposing phenotypic changes that depend on the duration of the perturbation. Such localization-based perturbation [182] may thus prove useful in elucidating mechanisms regulating cell signaling [210], [211]

and viral infections [205], [212], [213]. The NanoLoc platform could also be used to investigate the effect of aberrant localization of disease-related proteins [171], [214], [215].

I demonstrated that our nanobody-based system can achieve an exquisite level of spatial and temporal control over a target protein by combining the NanoLoc and NanoDeg technologies with transcriptional regulation. Small-molecule inducible promoters were used to drive orthogonal expression of VHH_{Loc} and VHH_{Deg} variants in the dual-input system, thereby tuning the duration of localization and the localized concentration of a target protein in multiple subcellular compartments. The NanoLoc system could also be expanded to localize multiple proteins to a single subcellular compartment by combining distinct VHH_{Loc} variants customized to recognize multiple targets. Developing the NanoLoc platform to control multiple targets in a distinct cellular compartment could open the way to a variety of metabolic engineering applications as it provides a powerful approach to regulate metabolite fluxes by controlling the local concentration of key reaction components [216], [217].

Finally, I demonstrated the use of the GFP-specific NanoLoc as a modular unit for synthetic genetic circuits that allows spatial control of the circuit's reporter protein. Synthetic mammalian gene networks are typically designed to regulate the concentration of a single reporter protein [6]. By contrast, the NanoLoc enables the regulation of both location and local concentration of the reporter protein, thereby

broadening the potential of genetic circuits for cell engineering. Here, I integrated VHH_{Loc} variants with transcriptional toggle switch regulation to achieve reversible localization of a target protein based on the state of the underlying genetic circuit. I anticipate that this strategy for spatial control of genetic circuit outputs will provide a novel method for orthogonal regulation of spatially constrained reactions using synthetic circuits that can reversibly locate a key reaction component [157] in response to the state of the genetic circuit.

In summary, the NanoLoc system provides an instrument for spatial and temporal control of protein concentration in mammalian cells that can be readily customized and integrated with transcriptional regulation to diversify the functionality of synthetic gene circuits.

5.4. Materials and Methods

5.4.1. Plasmids and Cloning

Localization signal sequences are listed in Table 5.4.1. The plasmids and primers used in this study are listed in Table 5.4.2 and Table 5.4.3, respectively. Plasmids were transformed and maintained in Stbl3 *E. Coli* competent cells (Thermo Fisher Scientific). PCR amplifications of DNA fragments were performed using Kappa HiFi DNA polymerase (Kapa Biosystems) according to the manufacturer's protocol. Plasmid sequences are available upon request.

Localization tag	Amino Acid Sequence	Reference
Mitochondria (MOM)	RGDGEPSGVPVAVVLLPVFALTLVAVWAFVRYRKQL	[192]
Endoplasmic reticulum (ER)	SGLRSFLVNMCVATVLTAGAYLCYR	[193]
Peroxisome (PEX)	ASGYKSKL	[194]
Plasma membrane (PM)	GCTVSAEDKAAAER	[195]
Nuclear localization signal (NLS)	PKKKRKV	[196]

Table 5.4.1 Localization tag sequences

The plasmid pSV40-GFP was generated by replacing the CMV promoter of pLenti CMV GFP Blast (Addgene plasmid # 17445) with the SV40 promoter using restriction enzymes ClaI and BamHI. The neomycin-resistance gene was PCR amplified from pcDNA3.1+ (Invitrogen) with primers designed to add BclI and BlnI enzyme recognition sites 5' and 3', respectively. The resulting fragment was ligated into the pLenti SV40 GFP vector, replacing the blasticidin-resistance gene, after digestion with BclI and BlnI restriction enzymes.

The VHH encoding sequence with a 5' fused HA tag sequence was amplified from pvhh [37]. The pCMV-VHH_{MOM}, pCMV-VHH_{ERM}, pCMV-VHH_{PEX}, and pCMV-VHH_{NLS} were constructed using overlap extension PCR to fuse the localization signal sequence 3' of the HA-VHH encoding sequence. The PCR amplified fragments encoding HA-VHH_{Loc} variants were ligated into the pvhh vector [37] after digestion with KpnI and NotI restriction enzymes. To generate pCMV-VHH_{PM}, the sequence encoding the plasma membrane localization signal was fused to the 5' end of the *vhh*

and the HA tag encoding sequence was fused to the 3' end of the *vhh* using overlap extension PCR. The resulting sequence was ligated into the *pvhh* vector after digestion with *AflIII* and *NotI* restriction enzymes.

The pCMV-TetR-IRES-EKRAB plasmid was constructed by ligating *TetR* (Invitrogen), an IRES (Addgene Plasmid #21547) and *EKRAB* [197] into the pLenti CMV eGFP Zeo vector (Addgene Plasmid #17449) after restriction enzyme digestion of *TetR* with *SpeI* and *SbfI*, IRES with *SbfI* and *MluI*, and *EKRAB* with *MluI* and *Sall*.

The pCMV/TO-iRFP plasmid was generated from pcDNA4/TO (Invitrogen) by replacing *gfp* with *irfp* (piRFP, Addgene plasmid #31857) using *KpnI* and *NotI* restriction enzymes. The CMV promoter containing four downstream repeats of the ETR operator site [197] (CMV/ETR) was generated by assembly PCR. The CMV/ETR promoter sequence was ligated into the pCMV/TO-iRFP vector, replacing the CMV/TO promoter, after digestion with *MluI* and *KpnI* restriction enzymes. The pCMV/TO-VHH_{MOM} plasmid was constructed by excising the HA-VHH_{MOM} sequence from pCMV-VHH_{MOM} and ligating it into pCMV/TO-iRFP, replacing *irfp*, using restriction enzymes *KpnI* and *NotI*. The pCMV/TO-VHH_{NLS} plasmid was constructed in the same manner by excising VHH_{NLS} from pCMV-VHH_{NLS}. The pCMV/ETR.VHH_{ODC(wt)} plasmid was constructed by excising VHH_{ODC(wt)} from *pvhh*-ODC [37] and ligating it into the pCMV/ETR-iRFP backbone, replacing *irfp*, using restriction enzymes *KpnI* and *NotI*. The pCMV/ETR-VHH_{MOM} plasmid was constructed in the same manner by excising VHH_{MOM} from pCMV-VHH_{MOM}.

To construct pCMV/ETR-VHH_{NLS}-IRES-PIPKRAB, the insert sequence encoding HA-VHH_{NLS}-IRES-PIPKRAB was generated by PCR amplification of HA-VHH_{NLS} from pCMV-VHH_{NLS} with primers designed to add the NheI and AgeI enzyme recognition sites at the 5' and 3' ends, respectively. The IRES sequence was amplified from pCMV-TetR-IRES-EKRAB with primers designed to add the AgeI and AflII enzyme recognition sites at the 5' and 3' ends, respectively, and the PIPKRAB sequence [203] was amplified with primers designed to add the AflII and NotI enzyme recognition sites at the 5' and 3' ends, respectively. These three insert sequences were then ligated into the pCMV/ETR-iRFP backbone, replacing *irfp*, using NheI and NotI restriction enzymes.

The pCMV/PIR-VHH_{MOM}-IRES-EKRAB plasmid was constructed by first replacing the ETR operator sites of pCMV/ETR-iRFP with PIR operator sites, which were generated by assembly PCR [203], to yield pCMV/PIR-iRFP. The sequence encoding VHH_{MOM} was PCR amplified from pCMV-VHH_{MOM} with overlapping primers designed to add a FLAG tag encoding sequence and a KasI enzyme recognition site at the 5' end and the AgeI enzyme recognition site at the 3' end. The IRES-EKRAB sequence was PCR amplified from pCMV.TetR-IRES-EKRAB with primers designed to add the AgeI and NotI enzyme recognition sites at the 5' and 3' ends, respectively. The FLAG-VHH_{MOM} and IRES-EKRAB inserts were then ligated into the pCMV/PIR-iRFP backbone, replacing *irfp*, using KasI and NotI restriction enzymes.

Sr. no.	Name of the plasmid	Notes	Ref
1.	pLenti SV40 GFP	GFP downstream of the SV40 promoter	This work
2.	pCMV.VHH _{MOM}	VHH tagged with mitochondrial outer membrane localization signal at the 3' end	This work
3.	pCMV.VHH _{ERM}	VHH tagged with endoplasmic reticulum localization signal at the 3' end	This work
4.	pCMV.VHH _{PEX}	VHH tagged with peroxisome localization signal at the 3' end	This work
5.	pCMV.VHH _{PM}	VHH tagged with plasma membrane localization signal at the 5' end	This work
6.	pCMV.VHH-NLS	VHH tagged with nuclear localization signal at the 3' end	This work
7.	pCMV.VHH _{ODC_{wt}}	VHH tagged with ODC degron at the 3' end	[32]
8.	pCMV.VHH _{ODC(T15A)}	VHH tagged with ODC _{T15A} degron variant at the 3' end	[32]
9.	pCMV.VHH _{ODC(D12A)}	VHH tagged with ODC _{D12A} degron variant at the 3' end	[32]
10.	pCMV/ETR.iRFP	iRFP downstream of a minimal CMV promoter consisting of four repeats of the ETR operator sequence	This work
11.	pCMV/TO.iRFP	iRFP downstream of a minimal CMV promoter consisting of two repeats of the TO operator sequence	This work
12.	pCMV/ETR.VHH _{MOM}	VHH-MOM downstream of a minimal CMV promoter consisting of four repeats of the ETR operator sequence	This work
13.	pCMV/TO.VHH _{NLS}	VHH-NLS downstream of a minimal CMV promoter consisting of two repeats of the TO operator sequence	This work
14.	pCMV-TetR-IRES-EKRAB	TetR and EKRAB downstream of a CMV promoter and separated by IRES	This work
15.	pCMV/TO-VHH _{MOM}	VHH-MOM downstream of a minimal CMV promoter consisting of two repeats of the TO operator sequence	This work
16.	pCMV/ETR-VHH _{ODC(wt)}	VHH-ODC _{wt} downstream of a minimal CMV promoter consisting of four repeats of the ETR operator sequence	This work
17.	pCMV/ETR-VHH _{NLS} -IRES-PIPKRAB	VHH-NLS and PIPKRAB separated by IRES, downstream of a minimal CMV promoter consisting of four repeats of the ETR operator sequence	This work
18.	pCMV/PIR.VHH _{MOM} -IRES-EKRAB	VHH-MOM and EKRAB separated by IRES, downstream of a minimal CMV promoter consisting of three repeats of the PIR operator sequence	This work

Table 5.4.2 Plasmids used in the NanoLoc study.

Primer Name	Sequence	Notes
F SV40-Clal	ATATGTACTTATATCGATTGTGTGGAATGTGTG TCAGTTAGGG	pSV40-GFP
GFP-Rev-BamHI	AATATATATTAGGATCCCTTGTACAGCTCGTCC ATGCCGAGAGTG	
BB-205R-Neo-BIpl	TTATAATATAGCTTAGCTCAGAAGAACTCGTCA AGAAGGCGA	
L_01F_pcDNA Fwd- KpnI	AAGCTTGGTACCGAGCTCGGATCCACC	
L_11F_MOM Fwd- BplI	CCAGCGGAGCTAAGCTAGGAGGAGGCACGCG TGGGCGAGGCGACGG	pCMV-VHH- MOM
L_12R_MOM Rev- NotI	GACTCGAGCGGCCGCTTAGAGCTGCTTTCGGT ATCTCACGAAGGCCAAACTGCTACCAG	
L_09F_ERM Fwd- BplI	CCAGCGGAGCTAAGCTAGGAGGAGGCAGTGG TCTTCGATCATTCTGGTCAACATGTGCG	pCMV-VHH- ERM
L_10R_ERM Rev- NotI	GACTCGAGCGGCCGCTTACCTGTAGCAGAGGT AAGCGCCGGC	
L_07R_VHH Rev- PEX	GCTTACTCTTGTATCCGCTAGCGCCTCCTCCTA GCTTAGCTCCGCTGGAGACGGTGACC	pCMV-VHH- PEX
L_08R_PEX Rev- NotI	GACTCGAGCGGCCGCTTACAGCTTACTCTTGT ATCCGCTAGCGCCTCCTCC	
L_15F_VHH Fwd- KpnI	CGCCACCGGTACCGGCGGAGATCAAGTCCAA CTGGTGGAGTC	pCMV-PM-VHH
L_27F_VHH Fwd PM Ext	GCCGAGGACAAGGCGGCGGCCGAGCGCTTAC CGGTCCGACCGGTACCGGCGGAGATCAA	
L_25F_PM Ext-AfIII	CGTTTAAACTTAAGCCACCATGGGCTGCACCG TGAGCGCCGAGGACAAGGCGGCGG	
L_16R_VHH Rev- BplI+linker-HA	TAGTCAGGCACATCGTAAGGGTAACCTCCTCC TAGCTTAGCTCCGCTGGAGACGGTGACC	
L_17R_HA ext Rev- NotI	GACTCGAGCGGCCGCTTACTACGCGTAGTCAG GCACATCGTAAGGGTAACCTCCTCC	
L_04R_VHH Rev- NES	TCCAGCTTGTCTGCAGCTCACTGCCTCCTCCT AGCTTAGCTCCGCTGGAGACGGTGACC	
L_05R_NES Ext Rev	GCTTACTTGTACGAGTCCAGATCCAACCTTCC AGCTTGTCTGCAGCTCACTGCCTC	pCMV-VHH- NES
L_06R_NES Rev- NotI	GACTCGAGCGGCCGCTTACTTGTACGAGTCCA GATCCAACCTTCCAGC	
L_02R_VHH Rev- NLS	TAGACCTTGCCTTCTTCTTAGGGCCTCCTCCT AGCTTAGCTCCGCTGGAGACGGTGACC	
L_03R_NLS Rev-NotI	CCTCTAGACTCGAGCGGCCGCTTAGACCTTGC GCTTCTTCTTAGGGCCTCCTCC	pCMV-VHH- NLS
L_30R_TetR Rev_SbfI	CTAGAGTGCCTGCAGGTCAATAAGATCTGAATT CCCGGGATCCGCTGTACGCG	
L_31F_IRES Fwd_SbfI	GCTCCAGTCTGCAGGCCGGGAGAGTGGGAT GAATGGATATCTAACGGATCCG	pCMV.TetR_IRE S_EKRAB
L_32R_IRES Rev_MluI	GGTAGGACACGCGTGTGTGGCCATATTATCA TCGTGTTTTTCAAAGGAAAACCACGTCCC	
L_33F_EKRAB Fwd_MluI	GACCACTGACGCGTGCCACCATGCCTCGCCCA AAGTTGAAGAG	

L_34R_EKRAB Rev_Sall	GCCGTCGTGTCGACAGAGACTACCAGAGGTC GTTCCCTGGCCATGC	
BL_01-HA-VHH-NLS- NheI	ATATTATAATGCTAGCCGCCACCATGTACCCTT ACGATGTGCCTGACT	pCMV.ETR- VHH- NLS_IRES_PIP KRAB
BL_02-R-NLS-AgeI	ATATTATATTACCGGTTTAGACCTTGCGCTTCT TCTTAGGG	
L_44F_IRES- Fwd_AgeI	GAACAACAACCGGTCCGGGAGAGTGGGATGA ATGGATATCTAACGG	
L_45R_IRES_Rev- AflII	GATAGACGCTTAAGGTTGTGGCCATATTATCAT CGTGTTTTTCAAAGGAAAACCACG	
L_50F_PIPKRAB- Fwd_AflII	GAAATGTGCTTAAGGCCACCATGAGTCGAGGA GAGGTACGAATGGCTAAGGCAGG	
L_51R_PIPKRAB- Rev_NotI	GGTTATTGGCGCCGCTTACCAGAGATCATT CTTGCCATTCCCTTCCATTTAATGTCAC	
BL_05F_VH H linker Fwd_FLAG tag	GGACTACAAAGACGATGACGATAAAGGTGGTT CTTCTGGTGGTGATCAAGTCCAAGTGG	pCMV.PIR- VHH- MOM_IRES_EK RAB
BL_06F_FLAG tag Fwd_KasI	GCACTAGGCGCCGCCACCATGGACTACAAAGA CGATGACGATAAAGGTGGTTCTTCTGG	
BL_04R-MOM-AgeI	TTATTTATTAACCGGTTTAGAGCTGCTTTTCGGT ATCTCAGC	
L_46F_EKRAB- Fwd_AflII	GAATGTATCTTAAGGCCACCATGCCTCGCCCA AAGTTGAAG	
L_47R_EKR AB-Rev_NotI	GAAAAGTAGCGGCCGCCTACCAGAGGTGCTTC CTGGCCATGCC	

Table 5.4.3 List of primers used in the NanoLoc study.

5.4.2. Cell culture and transfections

HEK293 cells (ATCC) and HEK293T cells (ATCC) were cultured in DMEM/High glucose (Hyclone) supplemented with 10% fetal bovine serum (FBS, GenClone) and 1% penicillin–streptomycin–glutamine (PSQ, Hyclone) and maintained at 37 °C and 5% CO₂. Cells were passaged using PBS (Lonza) and trypsin (TrypLE, GIBCO Invitrogen).

Transient transfections were performed by seeding cells onto 24-well plates, 12-well plates or 10 cm tissue culture dishes. After 24 h, cells were transfected using JetPrime (Polyplus transfection) according to manufacturer's protocol. The medium

was replaced with fresh medium 8 h or 16 h post-transfection and cells were replated onto coverslips 48 h post-transfection at a density of 18×10^4 cells/ml. Cells were fixed for analysis at 72 h post-transfection unless otherwise indicated.

5.4.3. Lentivirus production and transduction

Third-generation lentiviruses were generated by seeding HEK293T cells onto 10 cm tissue culture dishes at a density of 10×10^4 cells/ml. Cells were transfected with pSV40-GFP or pCMV-TetR-IRES-EKRAB, and the packaging plasmids pMLg/PRRE (Addgene plasmid #12251), pRSV-Rev (Addgene plasmid #12253), and pMD2.g (Addgene plasmid # 12259) in a 2:5:2.5:3 ratio, respectively. The medium was replaced with fresh medium 8 h post-transfection and the virus-containing medium was collected after 48 h. The virus was concentrated using a Lenti-X concentrator (Clontech) according to manufacturer's protocol.

Cell transductions were conducted by seeding HEK293 cells onto 12-well plates at a density of 10×10^4 cells/ml. After 24 h, the medium was replaced with medium supplemented with virus particles and 8 $\mu\text{g}/\text{ml}$ polybrene. The medium supplemented with virus was replaced with fresh medium 24 h post-transduction.

5.4.4. Generation of stable cell lines

To generate the GFP stable cell lines (HEK293/GFP#1, HEK293/GFP#2 and HEK293/GFP#3), HEK293 cells were seeded onto 12-well plates and transduced with pSV40-GFP. Cells were transferred into 10 cm tissue culture dishes 48 h post-

transduction and selected for 2 weeks using 1 mg/ml geneticin (MilliporeSigma). Cells were analyzed with a Nanocollect (Wolf) to sort cells presenting different levels of GFP fluorescence. Sorted cells were seeded onto 96-well plates containing DMEM with 20% FBS at a density of 1 cell/well, expanded, and monoclonal cell populations analyzed by flow cytometry to select the three cell lines presenting different levels of GFP fluorescence used in this study.

To generate the two-repressor stable cell line (HEK293/GFP2R), HEK293/GFP#1 cells were seeded onto 12-well plates and transduced with pCMV-TetR-IRES-EKRAB. Cells were transferred into 10 cm tissue culture dishes 48 h post-transduction and selected for 2 weeks using 500 µg/ml Zeocin (InvivoGen). The selected polyclonal population was diluted onto 96-well plates at a concentration of 0.5 cells/well and expanded. Monoclonal populations were then screened by transfection with pCMV/ETR-iRFP and pCMV/TO-iRFP, and treated with Em and Tc. The iRFP fluorescence of cells treated with or without inducer was measured by flow cytometry. The cell population exhibiting the greatest range of iRFP fluorescence intensity upon treatment with both Em and Tc was selected for further experiments.

5.4.5. Flow cytometry analyses

Cell were analyzed with a FACSCanto II flow cytometer (BD Biosciences). GFP fluorescence intensity was detected using a 488 nm laser and 530/30 nm emission filter. iRFP fluorescence intensity was detected using a 635 nm laser and 780/60 nm

emission filter. At least 10,000 cell events were recorded in each sample for analysis.

5.4.6. Immunofluorescence for confocal microscopy

Cells were seeded onto coverslips in a 24-well plate at a density of 9×10^4 cells. To stain mitochondria and plasma membrane, samples were stained with MitoTracker dye (200nM, ThermoFisher) or Membrite dye (Biotium) prior to fixing 24 h post-seeding according to the manufacturer's protocol. Cells were then washed once with PBS, fixed with 4% paraformaldehyde (15 min), and permeabilized with 0.1% TritonX-100 (7 mins). Cells were then washed three times with 0.1% Tween-20 in PBS (PBST) and blocked with 8% BSA (Calbiochem, 2930) for 1 h. Cells were washed three times with PBST and incubated in primary antibody (rabbit anti-HA SantaCruz Biotechnology sc-805, 1:250; mouse anti-calnexin, ThermoFisher MA3-027, 1:50; mouse anti-PMP70, Novus Biologicals NBP2-36770, 1:50) overnight. Cells were then washed three times with PBST and incubated with appropriate secondary antibodies (goat anti-rabbit DyLight 549 conjugated, Rockland 611-142-002, 1:500; goat anti-rabbit DyLight 405 conjugated, Rockland 611-146-002, 1:200; goat anti-mouse DyLight 549 conjugated, KPL 072-04-18-06, 1:500) for 2 h. Hoechst 3342 nuclear stain (Thermo Fisher Scientific) was added along with secondary antibodies where indicated. Coverslips were mounted onto glass slides using anti-fade solution (Invitrogen, S36936). Images were obtained with a Nikon A-1 confocal microscope (Nikon) and the Nikon NIS Element C imaging software. The acquired images were

minimally processed using ImageJ software to adjust brightness and contrast where indicated [218].

5.4.7. Image analysis

Analyses of GFP fluorescence intensity in 8-bit images was conducted using ImageJ. The areas of interest (cell and compartment) were segmented by establishing a threshold based on pixel intensity in the appropriate color channel for each image. The area of interest corresponding to the cell was first segmented in the color channel showing iRFP fluorescence, and then the area of interest corresponding to the subcellular compartment was further segmented within the cell area of interest in the color channel corresponding to the compartment stain. The fluorescence intensity was quantified by calculating the mean pixel intensity within the segmented subcellular compartment area of interest in the color channel showing GFP fluorescence. At least 15 cells per sample were analyzed. ImageJ macros are available upon request.

5.4.8. Statistical analysis

All data are reported as mean and error bars represent the standard error of at least three independent experiments. Statistical significance between samples was calculated using an unpaired two-tailed Student's *t*-test.

Summary and Future Work

6.1. Summary

The objective of this research was to develop tools for enhanced temporal and spatial control over cellular proteins that can be used in the characterization of biological parts and mechanisms of cellular information processing. This goal was achieved by engineering genetic circuits that can be used to modulate the temporal dynamics of the output and a platform for post-translational control that can regulate the localization of cellular proteins.

To improve input-dependent reporters for more precise characterization of promoter activity, I developed a tunable circuit module that enhances the dynamic range of the reporter and the temporal resolution of the input-dependent promoter activity (Chapter 3). Specifically, I integrated a reporter-specific NanoDeg in a

coherent feed-forward loop (CFFL) topology to produce the NanoDeg Inverter circuit which inverts the expression of the NanoDeg with respect to the input. This inversion of NanoDeg expression results in NanoDeg-mediated reduction of basal reporter levels thus enhancing the dynamic range. After the input is removed, the NanoDeg Inverter circuit leads to the production of the NanoDeg which, in turn, rapidly depletes the reporter thus enhancing the time resolution of the input. I validated the NanoDeg Inverter circuit experimentally in cells expressing a GFP reporter of heat shock. The rate of decay of GFP in the NanoDeg Inverter was modulated by altering the NanoDeg degradation rate. I also demonstrated that GFP dynamics in the NanoDeg Inverter are easily tuned by the addition of tetracycline. This study provides the design rules of a novel genetic circuit module that will be generally useful to build complex genetic networks for enhanced detection of highly dynamic behaviors.

To investigate strategies for control of genetic oscillators, I modeled NanoDeg-mediated degradation of oscillator network components (Chapter 4). Specifically, I identified topologies from two classes of biomolecular oscillators and predicted the effects of NanoDeg integration for post-translational modulation of network components on the circuit oscillatory behavior. I demonstrated that modifying the degradation rates of network components in relaxed-feedback oscillator and ring oscillator topologies is a strategy to generate oscillations. Furthermore, amplitude and period characteristics of the oscillation in these networks can be controlled by modifying the NanoDeg concentration or half-life. I

also proposed a strategy to generate oscillatory behavior from a non-oscillating cellular network by integrating the NanoDeg with a repressor-of-a-repressor network. This study provides a framework that can be used to guide the mechanistic study of periodic behavior in cellular adaptation.

To develop a platform for manipulating the extent and dynamics of protein localization, I constructed a toolkit of nanobodies that mediate localization of their target protein (NanoLoc) and combined nanobody-mediated localization with the degradation-enhancing capacity of the NanoDeg. I demonstrated that nanobody-mediated localization depends on the expression level of the nanobody and the target protein. The localized concentration of the target protein can be modulated by combining the NanoLoc and the NanoDeg platforms to control localization and degradation of the target protein. I also integrated nanobodies that mediate target localization into a synthetic toggle switch circuit and demonstrated spatial control of the output based on the state of the underlying genetic circuit. This study provides a comprehensive platform to control both the concentration and subcellular localization of a target protein.

6.2. Future Work

The study in Chapter 3 provides a novel genetic module that can be used to control the dynamic behavior of an input-dependent output. I expect that this module will be useful to investigate promoter activities that regulate the cell

response to repeated exposure of an input [219]–[221]. The circuit in this study rapidly eliminates GFP after input-dependent promoter activity is attenuated and would allow detecting periodic promoter activity occurring at short time intervals. The NanoDeg Inverter circuit provides a mechanism to modulate the basal levels and rate of decay of an input-dependent output by altering the NanoDeg degradation rate. Customizing the NanoDeg to target an output that operates as the input to a downstream circuit would allow the connection of the NanoDeg Inverter module to other defined circuit topologies. The dynamic control of the NanoDeg Inverter module output could, in this manner, be employed as a mode to tune more complex genetic circuits.

The study in Chapter 4 provides an exploration of strategies to generate oscillatory behavior in different types of genetic networks through enhanced degradation mediated by the NanoDeg. The most immediate application of this work would be to experimentally validate the proposed theoretical strategies. As an example, one can use a NanoDeg to perturb an activator-repressor topology [54] modified with a more stable activator. Using an activator-specific NanoDeg, the principles for tuning oscillations identified in this network can be verified by modulating the NanoDeg half-life and concentration. It would be particularly interesting to investigate the use of the NanoDeg to generate oscillations from a self-repressing system by creating a Goodwin oscillator. This implementation could then be contrasted directly with other Goodwin oscillators [222] where delay occurs at the post-transcriptional level, rather than post-translational level, providing a path

to better understand the roles of maturation delays and degradation in genetic networks. Additionally, an experimental comparison between the proposed NanoDeg repressilator and a transcription-based repressilator could provide a method to measure timescale differences between transcriptional and post-translational events.

The study in Chapter 5 provides a toolkit to precisely perturb the location and concentration of a target protein, which can be used to investigate the location-dependent activity of target proteins. Customizing this system with respect to the target, the subcellular location, and the degradation rate opens an array of possible future investigations. For example, reactive oxygen species (ROS) trigger the shuttling of p53 first to the mitochondria and then to the nucleus during an apoptosis response [223]. Generation of a p53-specific nanobody followed by integration of nanobodies controlling p53-specific localization into a bistable genetic circuit would allow investigating the effects of p53 localization on apoptosis, independent of the multitude of cell responses to ROS [224]. As mentioned, this platform could also be used in disease model systems to investigate if aberrant localization of disease-related proteins is causative or merely correlated to the disease process. Specifically, implementing the dual-input system to modulate the residence time of a disease-related target could uncover new mechanisms for disease progression. It would be particularly interesting to investigate the use of nanobodies as modular protein scaffolds [225]–[227]. The envisioned nanobody scaffolds could be constructed by first generating distinct nanobodies against MAPK

pathway proteins (e.g., Raf, MEK and ERK proteins), then modulating the concentration of these MAPK pathway components at the plasma membrane and monitoring the phenotypic effects, such as the rate of cell proliferation[228].

References

- [1] N. C. Bauer, P. W. Doetsch, and A. H. Corbett, "Mechanisms Regulating Protein Localization," *Traffic*, vol. 16, no. 10. Blackwell Munksgaard, pp. 1039–1061, 01-Oct-2015.
- [2] N. E. Davey and D. O. Morgan, "Building a Regulatory Network with Short Linear Sequence Motifs: Lessons from the Degrons of the Anaphase-Promoting Complex," *Molecular Cell*. 2016.
- [3] T. Lai, Y. Yang, and S. K. Ng, "Advances in mammalian cell line development technologies for recombinant protein production," *Pharmaceuticals*, vol. 6, no. 5, pp. 579–603, 2013.
- [4] Y. Qian, C. McBride, and D. Del Vecchio, "Programming Cells to Work for Us," *Annu. Rev. Control. Robot. Auton. Syst.*, 2018.
- [5] M. Xie and M. Fussenegger, "Designing cell function: assembly of synthetic gene circuits for cell biology applications," *Nature Reviews Molecular Cell Biology*. 2018.
- [6] D. Greber and M. Fussenegger, "Mammalian synthetic biology: Engineering of sophisticated gene networks," *Journal of Biotechnology*. 2007.
- [7] M. Wieland and M. Fussenegger, "Engineering Molecular Circuits Using Synthetic Biology in Mammalian Cells," *Annu. Rev. Chem. Biomol. Eng.*, 2012.

- [8] E. J. Olson and J. J. Tabor, "Post-translational tools expand the scope of synthetic biology," *Curr. Opin. Chem. Biol.*, vol. 16, no. 3–4, pp. 300–306, 2012.
- [9] A. Levskaya, O. D. Weiner, W. A. Lim, and C. A. Voigt, "Spatiotemporal control of cell signalling using a light-switchable protein interaction," *Nature*, 2009.
- [10] M. Strumillo and P. Beltrao, "Towards the computational design of protein post-translational regulation," *Bioorganic Med. Chem.*, 2015.
- [11] L. Zhang *et al.*, "Molecular imaging of Akt kinase activity," *Nat. Med.*, 2007.
- [12] J. Goedhart *et al.*, "Structure-guided evolution of cyan fluorescent proteins towards a quantum yield of 93%," *Nat. Commun.*, 2012.
- [13] X. Li *et al.*, "Generation of destabilized green fluorescent protein as a transcription reporter," *J. Biol. Chem.*, vol. 273, no. 52, pp. 34970–34975, Dec. 1998.
- [14] S. Harmansa and M. Affolter, "Protein binders and their applications in developmental biology," *Dev.*, 2018.
- [15] J. Helma, M. C. Cardoso, S. Muyldermans, and H. Leonhardt, "Nanobodies and recombinant binders in cell biology," *Journal of Cell Biology*. 2015.
- [16] K. Lyon and T. J. Stasevich, "Imaging Translational and Post-Translational Gene Regulatory Dynamics in Living Cells with Antibody-Based Probes," *Trends in Genetics*. 2017.

- [17] P. Monnier, R. Vigouroux, and N. Tassew, "In Vivo Applications of Single Chain Fv (Variable Domain) (scFv) Fragments," *Antibodies*, 2013.
- [18] H. K. Binz, P. Amstutz, and A. Plückthun, "Engineering novel binding proteins from nonimmunoglobulin domains," *Nature Biotechnology*. 2005.
- [19] A. Monegal *et al.*, "Immunological applications of single-domain llama recombinant antibodies isolated from a naïve library," *Protein Eng. Des. Sel.*, vol. 22, no. 4, pp. 273–280, 2009.
- [20] E. Pardon *et al.*, "A general protocol for the generation of Nanobodies for structural biology," *Nat. Protoc.*, vol. 9, no. 3, p. 674, 2014.
- [21] X. Fu *et al.*, "Design and Selection of a Camelid Single-Chain Antibody Yeast Two-Hybrid Library Produced De Novo for the Cap Protein of Porcine Circovirus Type 2 (PCV2)," *PLoS One*, vol. 8, no. 3, p. e56222, 2013.
- [22] M. H. Schut *et al.*, "Selection and characterization of llama single domain antibodies against N-terminal huntingtin," *Neurol. Sci.*, vol. 36, no. 3, pp. 429–434, 2015.
- [23] M. Arbabi Ghahroudi, A. Desmyter, L. Wyns, R. Hamers, and S. Muyldermans, "Selection and identification of single domain antibody fragments from camel heavy-chain antibodies," *FEBS Lett.*, vol. 414, no. 3, pp. 521–526, 1997.
- [24] R. Van Der Linden *et al.*, "Induction of immune responses and molecular

- cloning of the heavy chain antibody repertoire of Lama glama," *J. Immunol. Methods*, 2000.
- [25] J. S. M. Sabir *et al.*, "Construction of naïve camelids VHH repertoire in phage display-based library," *C. R. Biol.*, vol. 337, no. 4, pp. 244–249, 2014.
- [26] S. Moutel *et al.*, "NaLi-H1: A universal synthetic library of humanized nanobodies providing highly functional antibodies and intrabodies," *Elife*, vol. 5, p. e16228, 2016.
- [27] J. Yan, G. Li, Y. Hu, W. Ou, and Y. Wan, "Construction of a synthetic phage-displayed Nanobody library with CDR3 regions randomized by trinucleotide cassettes for diagnostic applications," *J. Transl. Med.*, vol. 12, no. 1, p. 343, 2014.
- [28] J. Tanha, G. Dubuc, T. Hiram, S. A. Narang, and C. R. MacKenzie, "Selection by phage display of llama conventional VH fragments with heavy chain antibody VHH properties," *J. Immunol. Methods*, 2002.
- [29] E. R. Goldman *et al.*, "Facile generation of heat-stable antiviral and antitoxin single domain antibodies from a semisynthetic llama library," *Anal. Chem.*, 2006.
- [30] P. Dufner, L. Jeremutis, and R. R. Minter, "Harnessing phage and ribosome display for antibody optimisation," *Trends in Biotechnology*. 2006.

- [31] Y. Wang *et al.*, “Nanobody-derived nanobiotechnology tool kits for diverse biomedical and biotechnology applications,” *International Journal of Nanomedicine*. 2016.
- [32] E. Beghein and J. Gettemans, “Nanobody technology: A versatile toolkit for microscopic imaging, protein-protein interaction analysis, and protein function exploration,” *Frontiers in Immunology*. 2017.
- [33] T. Guilliams *et al.*, “Nanobodies raised against monomeric α -synuclein distinguish between fibrils at different maturation stages,” *J. Mol. Biol.*, vol. 425, no. 14, pp. 2397–2411, 2013.
- [34] K. Domanska *et al.*, “Atomic structure of a nanobody-trapped domain-swapped dimer of an amyloidogenic 2-microglobulin variant,” *Proc. Natl. Acad. Sci.*, 2011.
- [35] S. G. F. Rasmussen *et al.*, “Structure of a nanobody-stabilized active state of the β 2 adrenoceptor,” *Nature*, 2011.
- [36] V. K. Nguyen, R. Hamers, L. Wyns, and S. Muyldermans, “Camel heavy-chain antibodies: Diverse germline V(H)H and specific mechanisms enlarge the antigen-binding repertoire,” *EMBO J.*, vol. 19, no. 5, pp. 921–930, 2000.
- [37] W. Zhao, L. Pferdehirt, and L. Segatori, “Quantitatively Predictable Control of Cellular Protein Levels through Proteasomal Degradation,” *ACS Synth. Biol.*, vol. 7, no. 2, pp. 540–552, 2018.

- [38] J. A. Kolkman and D. A. Law, "Nanobodies - From llamas to therapeutic proteins," *Drug Discov. Today Technol.*, vol. 7, no. 2, pp. e139–e146, 2010.
- [39] R. Y. Tsien, "The Green Fluorescent Protein," *Annu. Rev. Biochem.*, vol. 67, no. 1, pp. 509–544, 1998.
- [40] J. C. March, G. Rao, and W. E. Bentley, "Biotechnological applications of green fluorescent protein," *Appl. Microbiol. Biotechnol.*, vol. 62, no. 4, pp. 303–315, 2003.
- [41] M. Chalfie, Y. Tu, G. Euskirchen, W. Ward, and D. Prasher, "Green fluorescent protein as a marker for gene expression," *Science (80-.)*, vol. 263, no. 5148, pp. 802–805, 1994.
- [42] T. Stearns, D. Prasher, R. Tsien, W. Ward, and D. Prasher, "Green fluorescent protein. The green revolution," *Curr. Biol.*, vol. 5, no. 3, pp. 262–4, 1995.
- [43] P. Corish and C. Tyler-Smith, "Attenuation of green fluorescent protein half-life in mammalian cells," *Protein Eng. Des. Sel.*, vol. 12, no. 12, pp. 1035–1040, 1999.
- [44] A. F. Villaverde and J. R. Banga, "Reverse engineering and identification in systems biology: Strategies, perspectives and challenges," *J. R. Soc. Interface*, vol. 11, no. 91, 2014.
- [45] V. V. Verkhusha *et al.*, "High stability of *Discosoma* DsRed as compared to

- Aequorea EGFP," *Biochemistry*, vol. 42, no. 26, pp. 7879–7884, 2003.
- [46] A. V. Korennykh *et al.*, "The unfolded protein response signals through high-order assembly of Ire1," *Nature*, vol. 457, no. 7230, p. 687, 2009.
- [47] M. Kracikova, G. Akiri, A. George, R. Sachidanandam, and S. A. Aaronson, "A threshold mechanism mediates p53 cell fate decision between growth arrest and apoptosis," *Cell Death Differ.*, vol. 20, no. 4, p. 576, 2013.
- [48] J. P. MacKeigan, L. O. Murphy, C. A. Dimitri, and J. Blenis, "Graded Mitogen-Activated Protein Kinase Activity Precedes Switch-Like c-Fos Induction in Mammalian Cells," *Mol. Cell. Biol.*, vol. 25, no. 11, pp. 4676–4682, 2005.
- [49] D. Greber, M. D. El-Baba, and M. Fussenegger, "Intronicly encoded siRNAs improve dynamic range of mammalian gene regulation systems and toggle switch," *Nucleic Acids Res.*, vol. 36, no. 16, p. e101, 2008.
- [50] T. J. Morikawa *et al.*, "Dependence of fluorescent protein brightness on protein concentration in solution and enhancement of it," *Sci. Rep.*, vol. 6, p. 22342, 2016.
- [51] T. Reya *et al.*, "A role for Wnt signalling in self-renewal of haematopoietic stem cells," *Nature*, vol. 423, no. 6938, p. 409, 2003.
- [52] S. J. Kuhlman, J. E. Quintero, and D. G. McMahon, "GFP fluorescence reports Period1 circadian gene regulation in the mammalian biological clock,"

Neuroreport, vol. 11, no. 7, pp. 1479–1482, 2000.

- [53] M. B. Elowitz and S. Leibler, “A synthetic oscillatory network of transcriptional regulators,” *Nature*, vol. 403, no. 6767, p. 335, 2000.
- [54] M. Tigges, T. T. Marquez-Lago, J. Stelling, and M. Fussenegger, “A tunable synthetic mammalian oscillator,” *Nature*, vol. 457, no. 7227, p. 309, 2009.
- [55] Y. Chen *et al.*, “Tuning the dynamic range of bacterial promoters regulated by ligand-inducible transcription factors,” *Nat. Commun.*, vol. 9, no. 1, pp. 1–8, 2018.
- [56] R. M. Murray and D. Del Vecchio, *Biomolecular Feedback Systems*. 2014.
- [57] D. Longo and J. Hasty, “Dynamics of single-cell gene expression,” *Mol. Syst. Biol.*, vol. 2, no. 1, p. 64, 2006.
- [58] S. Mangan and U. Alon, “Structure and function of the feed-forward loop network motif,” *Pnas*, vol. 100, no. 21, pp. 11980–11985, 2003.
- [59] U. Alon, *An Introduction to Systems Biology: Design Principles of Biological Circuits*. 2007.
- [60] B. J. Wu, R. E. Kingston, and R. I. Morimoto, “Human HSP70 promoter contains at least two distinct regulatory domains,” *Proc. Natl. Acad. Sci. U. S. A.*, vol. 83, no. 3, pp. 629–633, 1986.
- [61] M. Dreano *et al.*, “High-level, heat-regulated synthesis of proteins in

- eukaryotic cells," *Gene*, vol. 49, no. 1, pp. 1–8, 1986.
- [62] Q. Huang *et al.*, "Heat-induced gene expression as a novel targeted cancer gene therapy strategy," *Cancer Res.*, vol. 60, no. 13, pp. 3435–3439, 2000.
- [63] K. Takeda *et al.*, "Cell biology: Incoherent feedforward control governs adaptation of activated ras in a eukaryotic chemotaxis pathway," *Sci. Signal.*, vol. 5, no. 205, pp. 29–31, 2012.
- [64] E. Hornstein and N. Shomron, "Canalization of development by microRNAs," *Nat. Genet.*, vol. 38, p. S20, 2006.
- [65] C. Mateus and S. V Avery, "Destabilized green fluorescent protein for monitoring dynamic changes in yeast gene expression with flow cytometry," *Yeast*, vol. 16, no. 14, pp. 1313–1323, 2000.
- [66] B. P. Ingalls, "Mathematical Modelling in Systems Biology : An Introduction," *J. Chem. Inf. Model.*, vol. 53, no. 9, pp. 1–396, 2014.
- [67] M. Gossen and H. Bujard, "Tight control of gene expression in mammalian cells by tetracycline-responsive promoters," *Proc. Natl. Acad. Sci.*, vol. 89, no. 12, pp. 5547–5551, 1992.
- [68] P. Orth, D. Schnappinger, W. Hillen, W. Saenger, and W. Hinrichs, "Structural basis of gene regulation by the tetracycline inducible Tet repressor-operator system," *Nat. Struct. Biol.*, vol. 7, no. 3, pp. 215–219, 2000.

- [69] E. W. Gerner *et al.*, "Heat-inducible vectors for use in gene therapy," *Int. J. Hyperth.*, vol. 16, no. 2, pp. 171–181, 2000.
- [70] W. Zhao, M. Bonem, C. McWhite, J. J. Silberg, and L. Segatori, "Sensitive detection of proteasomal activation using the Deg-On mammalian synthetic gene circuit," *Nat. Commun.*, vol. 5, pp. 1–12, 2014.
- [71] S. Hoops *et al.*, "COPASI - A COmplex PATHway Simulator," *Bioinformatics*, vol. 22, no. 24, pp. 3067–3074, 2006.
- [72] D. Shcherbo *et al.*, "Near-infrared fluorescent proteins," *Nat. Methods*, vol. 7, no. 10, p. 827, 2010.
- [73] I. R. Ghattas, J. R. Sanes, and J. E. Majors, "The encephalomyocarditis virus internal ribosome entry site allows efficient coexpression of two genes from a recombinant provirus in cultured cells and in embryos.," *Mol. Cell. Biol.*, vol. 11, no. 12, pp. 5848–5859, 1991.
- [74] E. E. Yao F, Svensjö T, Winkler T, Lu M, Eriksson C, "Tetracycline Repressor, tetR , rather than the Cell Transcription Factor Fusion Derivatives , Regulates Inducible Gene Expression in Mammalian Cells," vol. 1950, pp. 1939–1950, 1998.
- [75] G. S. Filonov, K. D. Piatkevich, L. M. Ting, J. Zhang, K. Kim, and V. V. Verkhusha, "Bright and stable near-infrared fluorescent protein for in vivo imaging," *Nat. Biotechnol.*, vol. 29, no. 8, p. 757, 2011.

- [76] W. Hillen, C. Gatz, L. Altschmied, K. Schollmeier, and I. Meier, "Control of expression of the Tn10-encoded tetracycline resistance genes. Equilibrium and kinetic investigation of the regulatory reactions," *J. Mol. Biol.*, vol. 169, no. 3, pp. 707–721, 1983.
- [77] A. L. Slusarczyk, A. Lin, and R. Weiss, "Foundations for the design and implementation of synthetic genetic circuits," *Nat. Rev. Genet.*, vol. 13, no. 6, p. 406, 2012.
- [78] H. Kobayashi *et al.*, "Programmable cells: Interfacing natural and engineered gene networks," *Proc. Natl. Acad. Sci.*, vol. 101, no. 22, pp. 8414–8419, 2004.
- [79] A. Goldbeter, "Biochemical oscillations and cellular rhythms: The molecular bases of periodic and chaotic behaviour Albert Goldbeter. Cambridge University Press, Cambridge, 1996. \$99.95 (cloth), 605 + xxiv pp," *Bull. Math. Biol.*, 1997.
- [80] W. O. Friesen and G. D. Block, "What is a biological oscillator?," *Am. J. Physiol.*, 1984.
- [81] C. H. Ko and J. S. Takahashi, "Molecular components of the mammalian circadian clock," *Human Molecular Genetics*. 2006.
- [82] C. Oikonomou and F. R. Cross, "Frequency control of cell cycle oscillators," *Current Opinion in Genetics and Development*. 2010.

- [83] J. E. Purvis, K. W. Karhohs, C. Mock, E. Batchelor, A. Loewer, and G. Lahav, "p53 dynamics control cell fate," *Science (80-.)*, 2012.
- [84] S. Ghosh and M. S. Hayden, "New regulators of NF- κ B in inflammation," *Nature Reviews Immunology*. 2008.
- [85] Y. Niwa, Y. Masamizu, T. Liu, R. Nakayama, C. X. Deng, and R. Kageyama, "The Initiation and Propagation of Hes7 Oscillation Are Cooperatively Regulated by Fgf and Notch Signaling in the Somite Segmentation Clock," *Dev. Cell*, 2007.
- [86] T. Kobayashi, H. Mizuno, I. Imayoshi, C. Furusawa, K. Shirahige, and R. Kageyama, "The cyclic gene Hes1 contributes to diverse differentiation responses of embryonic stem cells," *Genes Dev.*, 2009.
- [87] Y. H. Wu *et al.*, "Pineal clock gene oscillation is disturbed in Alzheimer's disease, due to functional disconnection from the 'master clock,'" *FASEB J.*, 2006.
- [88] X. R. Sailer, V. Beato, L. Schimansky-Geier, and H. Engel, "Noise-induced effects in excitable systems with local and global coupling," *Anal. Control Complex Nonlinear Process. Physics, Chem. Biol.*, pp. 1-41, 2007.
- [89] A. Rosenberg, S. Jayanthi, and D. Del Vecchio, "Tuning an activator-repressor clock employing retroactivity," in *Proceedings of the American Control Conference*, 2011.

- [90] S. Sastry, "Nonlinear systems: analysis, stability, and control, Shankar Sastry, Springer-Verlag, New York, NY, 1999, 667 pages. ISBN 0-387-98513-1.," *Int. J. Robust Nonlinear Control*, 2001.
- [91] D. Bratsun, D. Volfson, L. S. Tsimring, and J. Hasty, "Delay-induced stochastic oscillations in gene regulation," *Proc. Natl. Acad. Sci. U. S. A.*, 2005.
- [92] M. Xiao and J. Cao, "Genetic oscillation deduced from Hopf bifurcation in a genetic regulatory network with delays," *Math. Biosci.*, 2008.
- [93] D. Del Vecchio, "Design and analysis of an activator-repressor clock in E. Coli," in *Proceedings of the American Control Conference*, 2007.
- [94] S. Jayanthi and D. Del Vecchio, "Tuning genetic clocks employing DNA binding sites," *PLoS One*, 2012.
- [95] H. El Samad, D. Del Vecchio, and M. Khammash, "Repressilators and promotilators: Loop dynamics in synthetic gene networks," in *Proceedings of the American Control Conference*, 2005.
- [96] A. Ciliberto, B. Novak, and J. J. Tyson, "Steady states and oscillations in the p53/Mdm2 network," *Cell Cycle*, 2005.
- [97] B. E. K. Jayanthi, W. Zhao, and L. Segatori, "Input-dependent post-translational control of the reporter output enhances dynamic resolution of mammalian signaling systems," in *Methods in Enzymology*, 2019.

- [98] O. Purcell, N. J. Savery, C. S. Grierson, and M. Di Bernardo, "A comparative analysis of synthetic genetic oscillators," *Journal of the Royal Society Interface*. 2010.
- [99] N. Rosenfeld, J. W. Young, U. Alon, P. S. Swain, and M. B. Elowitz, "Gene regulation at the single-cell level," *Science (80-.)*, 2005.
- [100] R. Guantes and J. F. Poyatos, "Dynamical principles of two-component genetic oscillators," *PLoS Comput. Biol.*, 2006.
- [101] A. Möller, E. Pion, V. Narayan, and K. L. Ball, "Intracellular activation of interferon regulatory factor-1 by nanobodies to the multifunctional (Mf1) domain," *J. Biol. Chem.*, 2010.
- [102] J. Bethuyne *et al.*, "A nanobody modulates the p53 transcriptional program without perturbing its functional architecture," *Nucleic Acids Res.*, 2014.
- [103] U. Rothbauer, K. Zolghadr, S. Muyldermans, A. Schepers, M. C. Cardoso, and H. Leonhardt, "A versatile nanotrap for biochemical and functional studies with fluorescent fusion proteins," *Mol. Cell. Proteomics*, 2008.
- [104] M. B. Braun *et al.*, "Peptides in headlock - A novel high-affinity and versatile peptide-binding nanobody for proteomics and microscopy," *Sci. Rep.*, 2016.
- [105] S. Jayanthi, K. S. Nilgiriwala, and D. Del Vecchio, "Retroactivity controls the temporal dynamics of gene transcription," *ACS Synth. Biol.*, 2013.

- [106] J. E. Ferrell and S. H. Ha, "Ultrasensitivity part II: Multisite phosphorylation, stoichiometric inhibitors, and positive feedback," *Trends in Biochemical Sciences*. 2014.
- [107] A. Burger, A. M. Walczak, and P. G. Wolynes, "Abduction and asylum in the lives of transcription factors," *Proc. Natl. Acad. Sci. U. S. A.*, 2010.
- [108] B. C. Goodwin, "Oscillatory behavior in enzymatic control processes," *Adv. Enzyme Regul.*, 1965.
- [109] J. Stricker, S. Cookson, M. R. Bennett, W. H. Mather, L. S. Tsimring, and J. Hasty, "A fast, robust and tunable synthetic gene oscillator," *Nature*, 2008.
- [110] A. Woller, D. Gonze, and T. Erneux, "The Goodwin model revisited: Hopf bifurcation, limit-cycle, and periodic entrainment," *Phys. Biol.*, 2014.
- [111] A. Verdugo and R. Rand, "Hopf bifurcation in a DDE model of gene expression," *Commun. Nonlinear Sci. Numer. Simul.*, 2008.
- [112] J. P. Pett, A. Korenčič, F. Wesener, A. Kramer, and H. Herzel, "Feedback Loops of the Mammalian Circadian Clock Constitute Repressilator," *PLoS Comput. Biol.*, 2016.
- [113] A. Pokhilko, A. P. Fernández, K. D. Edwards, M. M. Southern, K. J. Halliday, and A. J. Millar, "The clock gene circuit in Arabidopsis includes a repressilator with additional feedback loops," *Mol. Syst. Biol.*, 2012.

- [114] O. Buse, R. Pérez, and A. Kuznetsov, "Dynamical properties of the repressilator model," *Phys. Rev. E - Stat. Nonlinear, Soft Matter Phys.*, 2010.
- [115] J. Tyler, A. Shiu, and J. Walton, "Revisiting a synthetic intracellular regulatory network that exhibits oscillations," *J. Math. Biol.*, 2019.
- [116] S. Müller, J. Hofbauer, L. Endler, C. Flamm, S. Widder, and P. Schuster, "A generalized model of the repressilator," *J. Math. Biol.*, 2006.
- [117] I. Potapov, E. Volkov, and A. Kuznetsov, "Dynamics of coupled repressilators: The role of mRNA kinetics and transcription cooperativity," *Phys. Rev. E - Stat. Nonlinear, Soft Matter Phys.*, 2011.
- [118] K. F. Wildt *et al.*, "The Transcription Factor Zbtb7b Promotes CD4 Expression by Antagonizing Runx-Mediated Activation of the CD4 Silencer," *J. Immunol.*, 2007.
- [119] N. Nakamichi, T. Kiba, R. Henriques, T. Mizuno, N. H. Chua, and H. Sakakibara, "PSEUDO-RESPONSE REGULATORS 9, 7, and 5 are transcriptional repressors in the Arabidopsis circadian clock," *Plant Cell*, 2010.
- [120] A. L. Silverstone, H. S. Jung, A. Dill, H. Kawaide, Y. Kamiya, and T. P. Sun, "Repressing a repressor: Gibberellin-induced rapid reduction of the RGA protein in Arabidopsis," *Plant Cell*, 2001.
- [121] X. Zhang *et al.*, "Macrophage/microglial Ezh2 facilitates autoimmune

inflammation through inhibition of Socs3," *J. Exp. Med.*, 2018.

- [122] A. Goldbeter and D. E. Koshland, "An amplified sensitivity arising from covalent modification in biological systems," *Proc. Natl. Acad. Sci. U. S. A.*, 1981.
- [123] J. A. Sepulchre and A. C. Ventura, "Intrinsic Feedbacks in MAPK Signaling Cascades Lead to Bistability and Oscillations," *Acta Biotheor.*, 2013.
- [124] N. Blüthgen, S. Legewie, H. Herzel, and B. Kholodenko, "Mechanisms generating ultrasensitivity, bistability, and oscillations in signal transduction," in *Introduction to Systems Biology*, 2007.
- [125] M. R. Atkinson, M. A. Savageau, J. T. Myers, and A. J. Ninfa, "Development of genetic circuitry exhibiting toggle switch or oscillatory behavior in *Escherichia coli*," *Cell*, vol. 113, no. 5, pp. 597–607, May 2003.
- [126] Y. Chen, J. K. Kim, A. J. Hirning, K. Josić, and M. R. Bennett, "Emergent genetic oscillations in a synthetic microbial consortium," *Science (80-.)*, 2015.
- [127] A. N. Dodd *et al.*, "The Arabidopsis circadian clock incorporates a cADPR-based feedback loop," *Science (80-.)*, 2007.
- [128] K. D. Nguyen, S. J. Fentress, Y. Qiu, K. Yun, J. S. Cox, and A. Chawla, "Circadian gene *Bmal1* regulates diurnal oscillations of Ly6Chi inflammatory monocytes," *Science (80-.)*, 2013.

- [129] J. K. Dale, M. Maroto, M. L. Dequeant, P. Malapert, M. McGrew, and O. Pourquie, "Periodic Notch inhibition by lunatic fringe underlies the chick segmentation clock," *Nature*, 2003.
- [130] M. Tigges, N. Dénervaud, D. Greber, J. Stelling, and M. Fussenegger, "A synthetic low-frequency mammalian oscillator," *Nucleic Acids Res.*, 2010.
- [131] Z. Wang, D. A. Potoyan, and P. G. Wolynes, "Molecular stripping, targets and decoys as modulators of oscillations in the NF-kB/IkBa/DNA genetic network," *J. R. Soc. Interface*, 2016.
- [132] D. Del Vecchio and E. D. Sontag, "Dynamics and control of synthetic biomolecular networks," in *Proceedings of the American Control Conference*, 2007, pp. 1577–1588.
- [133] R. N. Cohen, M. A. E. M. van der Aa, N. Macaraeg, A. P. Lee, and F. C. Szoka, "Quantification of plasmid DNA copies in the nucleus after lipoplex and polyplex transfection," *J. Control. Release*, 2009.
- [134] C. Theodore T., Puck, Philip I., Marcus, Steven J., "Clonal Growth of Mammalian Cells in vitro," *J. Exp. Med.*, 1955.
- [135] J. Berg, J. Tymoczko, and L. Stryer, *Biochemistry*, 5. Auflage. 2002.
- [136] A. Coulon, C. C. Chow, R. H. Singer, and D. R. Larson, "Eukaryotic transcriptional dynamics: From single molecules to cell populations," *Nature*

Reviews Genetics, vol. 14, no. 8. pp. 572–584, Aug-2013.

- [137] V. M. Weake and J. L. Workman, “Inducible gene expression: Diverse regulatory mechanisms,” *Nature Reviews Genetics*. 2010.
- [138] S. A. Lambert *et al.*, “The Human Transcription Factors,” *Cell*. 2018.
- [139] K. M. Lelli, M. Slattery, and R. S. Mann, “Disentangling the Many Layers of Eukaryotic Transcriptional Regulation,” *Annu. Rev. Genet.*, 2012.
- [140] M. Hochstrasser, “Ubiquitin, proteasomes, and the regulation of intracellular protein degradation,” *Curr. Opin. Cell Biol.*, 1995.
- [141] P. O. Seglen and P. Bohley, “Autophagy and other vacuolar protein degradation mechanisms,” *Experientia*. 1992.
- [142] A. L. Goldberg, “Protein degradation and protection against misfolded or damaged proteins,” *Nature*. 2003.
- [143] H. Liu, S. Urbé, and M. J. Clague, “Selective protein degradation in cell signalling,” *Seminars in Cell and Developmental Biology*, vol. 23, no. 5. Elsevier Ltd, pp. 509–514, 2012.
- [144] C. Kraft, M. Peter, and K. Hofmann, “Selective autophagy: Ubiquitin-mediated recognition and beyond,” *Nature Cell Biology*. 2010.
- [145] A. Varshavsky, “The N-end rule pathway and regulation by proteolysis,” *Protein Science*. 2011.

- [146] S. Negi, S. Pandey, S. M. Srinivasan, A. Mohammed, and C. Guda, "LocSigDB: A database of protein localization signals," *Database*, 2015.
- [147] P. Chan, J. Lovrić, and J. Warwicker, "Subcellular pH and predicted pH-dependent features of proteins," *Proteomics*, 2006.
- [148] L. J. Sweetlove and A. R. Fernie, "The Spatial Organization of Metabolism Within the Plant Cell," *Annu. Rev. Plant Biol.*, 2013.
- [149] C. M. Jakobson, D. Tullman-Ercek, and N. M. Mangan, "Spatially organizing biochemistry: Choosing a strategy to translate synthetic biology to the factory," *Sci. Rep.*, 2018.
- [150] P. Kakkar and B. K. Singh, "Mitochondria: A hub of redox activities and cellular distress control," *Mol. Cell. Biochem.*, 2007.
- [151] M. C. Good, J. G. Zalatan, and W. A. Lim, "Scaffold proteins: Hubs for controlling the flow of cellular information," *Science*. 2011.
- [152] D. K. Morrison and R. J. Davis, "Regulation of MAP Kinase Signaling Modules by Scaffold Proteins in Mammals," *Annu. Rev. Cell Dev. Biol.*, 2003.
- [153] M. C. Konopka, I. A. Shkel, S. Cayley, M. T. Record, and J. C. Weisshaar, "Crowding and confinement effects on protein diffusion in vivo," *J. Bacteriol.*, 2006.
- [154] A. Takano *et al.*, "Mammalian Target of Rapamycin Pathway Regulates Insulin

Signaling via Subcellular Redistribution of Insulin Receptor Substrate 1 and Integrates Nutritional Signals and Metabolic Signals of Insulin," *Mol. Cell. Biol.*, 2001.

- [155] S. Kamatkar, V. Radha, S. Nambirajan, R. S. Reddy, and G. Swarup, "Two splice variants of a tyrosine phosphatase differ in substrate specificity, DNA binding, and subcellular location," *J. Biol. Chem.*, 1996.
- [156] D. Jagnandan, W. C. Sessa, and D. Fulton, "Intracellular location regulates calcium-calmodulin-dependent activation of organelle-restricted eNOS," *Am. J. Physiol. - Cell Physiol.*, 2005.
- [157] N. Hao, B. A. Budnik, J. Gunawardena, and E. K. O'Shea, "Tunable signal processing through modular control of transcription factor translocation," *Science (80-.)*, 2013.
- [158] S. Y. Jeong and D. W. Seol, "The role of mitochondria in apoptosis," *Journal of Biochemistry and Molecular Biology*. 2008.
- [159] B. D. Grant and J. G. Donaldson, "Pathways and mechanisms of endocytic recycling," *Nature Reviews Molecular Cell Biology*. 2009.
- [160] J. Ryu and S. H. Park, "Simple synthetic protein scaffolds can create adjustable artificial MAPK circuits in yeast and mammalian cells," *Sci. Signal.*, 2015.
- [161] C. M. Agapakis, P. M. Boyle, and P. A. Silver, "Natural strategies for the spatial

- optimization of metabolism in synthetic biology," *Nature Chemical Biology*. 2012.
- [162] G. Chatterjee, N. Dalchau, R. A. Muscat, A. Phillips, and G. Seelig, "A spatially localized architecture for fast and modular DNA computing," *Nat. Nanotechnol.*, 2017.
- [163] O. N. Yogurtcu and M. E. Johnson, "Cytosolic proteins can exploit membrane localization to trigger functional assembly," *PLoS Comput. Biol.*, 2018.
- [164] C. Myhrvold, J. K. Polka, and P. A. Silver, "Synthetic Lipid-Containing Scaffolds Enhance Production by Colocalizing Enzymes," *ACS Synthetic Biology*. 2016.
- [165] G. J. Bassell and S. Kelic, "Binding proteins for mRNA localization and local translation, and their dysfunction in genetic neurological disease," *Current Opinion in Neurobiology*. 2004.
- [166] W. Wang, E. Van Niekerk, D. E. Willis, and J. L. Twiss, "RNA transport and localized protein synthesis in neurological disorders and neural repair," *Developmental Neurobiology*. 2007.
- [167] N. W. Kowall and K. S. Kosik, "Axonal disruption and aberrant localization of tau protein characterize the neuropil pathology of Alzheimer's disease," *Ann. Neurol.*, 1987.
- [168] S. Calvo *et al.*, "Systematic identification of human mitochondrial disease

genes through integrative genomics," *Nat. Genet.*, 2006.

[169] D. S. Lee, J. Park, K. A. Kay, N. A. Christakis, Z. N. Oltvai, and A. L. Barabási, "The implications of human metabolic network topology for disease comorbidity," *Proc. Natl. Acad. Sci. U. S. A.*, 2008.

[170] X. Wang and S. Li, "Protein mislocalization: Mechanisms, functions and clinical applications in cancer," *Biochimica et Biophysica Acta - Reviews on Cancer*. 2014.

[171] M. C. Hung and W. Link, "Protein localization in disease and therapy," *J. Cell Sci.*, 2011.

[172] G. Prelich, "Gene overexpression: Uses, mechanisms, and interpretation," *Genetics*. 2012.

[173] W. P. Blackstock and M. P. Weir, "Proteomics: Quantitative and physical mapping of cellular proteins," *Trends in Biotechnology*. 1999.

[174] H. Kim and J. S. Kim, "A guide to genome engineering with programmable nucleases," *Nature Reviews Genetics*. 2014.

[175] C. J. Bashor, A. A. Horwitz, S. G. Peisajovich, and W. A. Lim, "Rewiring Cells: Synthetic Biology as a Tool to Interrogate the Organizational Principles of Living Systems," *Annu. Rev. Biophys.*, 2010.

[176] A. E. Campbell and D. Bennett, "Targeting protein function: The expanding

toolkit for conditional disruption," *Biochemical Journal*. 2016.

[177] R. E. Hosein, S. A. Williams, K. Haye, and R. H. Gavin, "Expression of GFP-Actin Leads to Failure of Nuclear Elongation and Cytokinesis in *Tetrahymena thermophila*," *J. Eukaryot. Microbiol.*, 2003.

[178] M. Nelson and P. Silver, "Context affects nuclear protein localization in *Saccharomyces cerevisiae*," *Mol. Cell. Biol.*, 1989.

[179] M. G. Douglas, M. T. McCammon, and A. Vassarotti, "Targeting proteins into mitochondria," *Microbiological Reviews*. 1986.

[180] M. Putyrski and C. Schultz, "Protein translocation as a tool: The current rapamycin story," *FEBS Letters*. 2012.

[181] N. Umeda, T. Ueno, C. Pohlmeier, T. Nagano, and T. Inoue, "A photocleavable rapamycin conjugate for spatiotemporal control of small GTPase activity," *J. Am. Chem. Soc.*, 2011.

[182] M. S. Robinson, D. A. Sahlender, and S. D. Foster, "Rapid Inactivation of Proteins by Rapamycin-Induced Rerouting to Mitochondria," *Dev. Cell*, 2010.

[183] K. A. Brown *et al.*, "Light-cleavable rapamycin dimer as an optical trigger for protein dimerization," *Chem. Commun.*, 2015.

[184] P. Geda *et al.*, "A small molecule-directed approach to control protein localization and function," *Yeast*, 2008.

- [185] J. E. Toettcher, D. Gong, W. A. Lim, and O. D. Weiner, "Light control of plasma membrane recruitment using the Phy-PIF system," *Methods Enzymol.*, 2011.
- [186] C. E. Buckley, R. E. Moore, A. Reade, A. R. Goldberg, O. D. Weiner, and J. D. W. Clarke, "Reversible Optogenetic Control of Subcellular Protein Localization in a Live Vertebrate Embryo," *Dev. Cell*, 2016.
- [187] M. Adrian, W. Nijenhuis, R. I. Hoogstraaten, J. Willems, and L. C. Kapitein, "A Phytochrome-Derived Photoswitch for Intracellular Transport," *ACS Synth. Biol.*, 2017.
- [188] S. Harmansa, I. Alborelli, D. Bieli, E. Caussin, and M. Affolter, "A nanobody-based toolset to investigate the role of protein localization and dispersal in *Drosophila*," *Elife*, 2017.
- [189] E. Beghein, I. Van Audenhove, O. Zwaenepoel, A. Verhelle, A. De Ganck, and J. Gettemans, "A new survivin tracer tracks, delocalizes and captures endogenous survivin at different subcellular locations and in distinct organelles," *Sci. Rep.*, 2016.
- [190] I. Van Audenhove *et al.*, "Stratifying fascin and cortactin function in invadopodium formation using inhibitory nanobodies and targeted subcellular delocalization," *FASEB J.*, 2014.
- [191] E. Caussin, O. Kanca, and M. Affolter, "Fluorescent fusion protein knockout mediated by anti-GFP nanobody," *Nat. Struct. Mol. Biol.*, vol. 19, no. 1, pp. 117–

122, 2012.

- [192] C. Horie, H. Suzuki, M. Sakaguchi, and K. Mihara, "Characterization of signal that directs C-tail-anchored proteins to mammalian mitochondrial outer membrane," *Mol. Biol. Cell*, vol. 13, no. 5, pp. 1615–1625, 2002.
- [193] I. Anderie, I. Schulz, and A. Schmid, "Characterization of the C-terminal ER membrane anchor of PTP1B," *Exp. Cell Res.*, vol. 313, no. 15, pp. 3189–3197, Sep. 2007.
- [194] C. Brocard and A. Hartig, "Peroxisome targeting signal 1: Is it really a simple tripeptide?," *Biochimica et Biophysica Acta - Molecular Cell Research*, vol. 1763, no. 12, pp. 1565–1573, Dec-2006.
- [195] D. Clift *et al.*, "A Method for the Acute and Rapid Degradation of Endogenous Proteins," *Cell*, vol. 171, no. 7, pp. 1692-1706.e18, Dec. 2017.
- [196] D. Kalderon, B. L. Roberts, W. D. Richardson, and A. E. Smith, "A short amino acid sequence able to specify nuclear location," *Cell*, vol. 39, no. 3 PART 2, pp. 499–509, 1984.
- [197] W. Weber *et al.*, "Macrolide-based transgene control in mammalian cells and mice," *Nat. Biotechnol.*, vol. 20, no. 9, pp. 901–907, 2002.
- [198] B. Angelici, E. Mailand, B. Haefliger, and Y. Benenson, "Synthetic Biology Platform for Sensing and Integrating Endogenous Transcriptional Inputs in

- Mammalian Cells.," *Cell Rep.*, vol. 16, no. 9, pp. 2525–37, 2016.
- [199] S. -i. Matsuzawa, M. Cuddy, T. Fukushima, and J. C. Reed, "Method for targeting protein destruction by using a ubiquitin-independent, proteasome-mediated degradation pathway," *Proc. Natl. Acad. Sci.*, vol. 102, no. 42, pp. 14982–14987, 2005.
- [200] W. Hillen and C. Berens, "Mechanisms underlying expression of Tn10 encoded tetracycline resistance.," *Annu. Rev. Microbiol.*, vol. 48, pp. 345–69, 1994.
- [201] T. S. Gardner, C. R. Cantor, and J. J. Collins, "Construction of a genetic toggle switch in *Escherichia coli*," *Nature*, vol. 403, no. 6767, pp. 339–342, Jan. 2000.
- [202] M. Sadeghpour, A. Veliz-Cuba, G. Orosz, K. Josić, and M. R. Bennett, "Bistability and oscillations in co-repressive synthetic microbial consortia."
- [203] B. P. Kramer, A. U. Viretta, M. D. E. Baba, D. Aubel, W. Weber, and M. Fussenegger, "An engineered epigenetic transgene switch in mammalian cells," *Nat. Biotechnol.*, vol. 22, no. 7, pp. 867–870, Jul. 2004.
- [204] K. Müller *et al.*, "A red/far-red light-responsive bi-stable toggle switch to control gene expression in mammalian cells," *Nucleic Acids Res.*, vol. 41, no. 7, Apr. 2013.
- [205] A. Cattaneo and S. Biocca, "The selection of intracellular antibodies," *Trends in Biotechnology*. 1999.

- [206] M. Alessandra Vigano *et al.*, "DARPin recognize mTFP1 as novel reagents for in vitro and in vivo protein manipulations," *Biol. Open*, 2018.
- [207] H. J. Wagner, S. Wehrle, E. Weiss, M. Cavallari, and W. Weber, "A two-step approach for the design and generation of nanobodies," *Int. J. Mol. Sci.*, 2018.
- [208] R. H. J. J. Van Der Linden *et al.*, "Comparison of physical chemical properties of llama VHH antibody fragments and mouse monoclonal antibodies," *Biochim. Biophys. Acta - Protein Struct. Mol. Enzymol.*, vol. 1431, no. 1, pp. 37–46, 1999.
- [209] H.-P. Peng, K. H. Lee, J.-W. Jian, and A.-S. Yang, "Origins of specificity and affinity in antibody–protein interactions," *Proc. Natl. Acad. Sci.*, p. 201401131, 2014.
- [210] H. Kaji, L. Canaff, J. J. Lebrun, D. Goltzman, and G. N. Hendy, "Inactivation of menin, a Smad3-interacting protein, blocks transforming growth factor type β signaling," *Proc. Natl. Acad. Sci. U. S. A.*, 2001.
- [211] R. K. Bikkavilli, M. E. Feigin, and C. C. Malbon, "p38 mitogen-activated protein kinase regulates canonical Wnt- β -catenin signaling by inactivation of GSK3 β ," *J. Cell Sci.*, 2008.
- [212] W. A. Marasco, W. A. Haseltine, and S. Chen, "Design, intracellular expression, and activity of a human anti-human immunodeficiency virus type 1 gp120 single-chain antibody," *Proc. Natl. Acad. Sci. U. S. A.*, 1993.

- [213] S. Biocca, F. Ruberti, M. Tafani, P. Pierandrei-Amaldi, and A. Cattaneo, "Redox state of single chain FV fragments targeted to the endoplasmic reticulum, cytosol and mitochondria," *Bio/Technology*, 1995.
- [214] J. D. Moore, "In the wrong place at the wrong time: Does cyclin mislocalization drive oncogenic transformation?," *Nature Reviews Cancer*. 2013.
- [215] H. Zempel and E. Mandelkow, "Lost after translation: Missorting of Tau protein and consequences for Alzheimer disease," *Trends in Neurosciences*. 2014.
- [216] J. E. Dueber *et al.*, "Synthetic protein scaffolds provide modular control over metabolic flux," *Nat. Biotechnol.*, 2009.
- [217] H. Lee, W. C. DeLoache, and J. E. Dueber, "Spatial organization of enzymes for metabolic engineering," *Metab. Eng.*, 2012.
- [218] J. Schindelin *et al.*, "Fiji: An open-source platform for biological-image analysis," *Nature Methods*, vol. 9, no. 7. pp. 676–682, Jul-2012.
- [219] A. Martinez Guimera, C. M. Welsh, C. J. Proctor, A. McArdle, and D. P. Shanley, "'Molecular habituation' as a potential mechanism of gradual homeostatic loss with age," *Mech. Ageing Dev.*, 2018.
- [220] E. L. Ardiel, A. J. Yu, A. C. Giles, and C. H. Rankin, "Habituation as an adaptive shift in response strategy mediated by neuropeptides," *npj Sci. Learn.*, 2017.

- [221] C. M. McInnis *et al.*, "Response and habituation of pro- and anti-inflammatory gene expression to repeated acute stress," *Brain. Behav. Immun.*, 2015.
- [222] I. A. Swinburne, D. G. Miguez, D. Landgraf, and P. A. Silver, "Intron length increases oscillatory periods of gene expression in animal cells," *Genes Dev.*, 2008.
- [223] Y. Zhao *et al.*, "p53 translocation to mitochondria precedes its nuclear translocation and targets mitochondrial oxidative defense protein-manganese superoxide dismutase," *Cancer Res.*, 2005.
- [224] M. D. Temple, G. G. Perrone, and I. W. Dawes, "Complex cellular responses to reactive oxygen species," *Trends in Cell Biology*. 2005.
- [225] C. J. Bashor, N. C. Helman, S. Yan, and W. A. Lim, "Using engineered scaffold interactions to reshape MAP kinase pathway signaling dynamics," *Science (80-.)*, 2008.
- [226] A. Bell *et al.*, "Differential tumor-targeting abilities of three single-domain antibody formats," *Cancer Lett.*, 2010.
- [227] J. Zhang *et al.*, "Pentamerization of single-domain antibodies from phage libraries: A novel strategy for the rapid generation of high-avidity antibody reagents," *J. Mol. Biol.*, 2004.
- [228] W. Kolch, "Meaningful relationships: The regulation of the Ras/Raf/MEK/ERK

pathway by protein interactions," *Biochemical Journal*. 2000.